THE UNIVERSITY OF SUSSEX

Analytical Modelling of Multi-Spacecraft Reconnection Layer Measurements at the Magnetopause

Jonathan Daniel Crofts
Submitted for the degree of DPhil
September 2009

DECLARATION

I hereby declare that all work contained within this thesis is my own, unless stated otherwise, and that it has not been and will not be, submitted in whole or in part to another University for the award of any other degree.

Jonathan Daniel Crofts
7th January, 2011

ACKNOWLEDGEMENTS

To thank the people who have made this thesis, and the work it represents, possible is an enormous task. I would like to first thank and acknowledge my supervisors.

Dr Richard Rijnbeek was my supervisor both during my masters degree, and my primary supervisor during the first two years of my doctorate, he introduced me to this field of research and imparted both the information and enthusiasm required to pursue it. During this time Dr Andrew Buckley was, initially, my secondary supervisor. After Dr Rijnbeek left to pursue other avenues, he and Professor Paul Gough became, between them, my supervisory team. Both have worked tirelessly on my behalf over the last two years and I could not have come this far without their efforts.

Having made extensive use of the CLUSTER Active Archive, its data, and its instrument information, I would like to thank the entire CAA team. I would especially like to single out the FGM and CIS instrument teams, and from those teams Dr Elizabeth Lucek (FGM), Prof. Henri Rème (CIS) and Dr Iannis Dandouras (CIS) all of whom have been the more than patient recipients and respondents of queries.

Enormous thanks must go to my family, whose continuous encouragement and occasional nagging have been invaluable. Special mentions must go to my parents, especially my mother, who have been incredibly supportive in all possible ways, and to my wonderful wife Miyuki. The way that she has approached my long hours and bad moods with a calm, soothing and above all patient manner has been beyond anything I could have hoped for. Thank you!

Many friends have been a part of this journey, and sadly there isn't space here to thank them all. This extraordinary bunch of people have offered their time and energy on countless occasions. I would not have been able to manage this without them, a few of these poor unfortunates are: Leo, Nick, Sally, James, Angela, Oli, Pete, Adam, Andy, Ellie, Duncan and Kadia. Thanks guys, you've been wonderful.

THE UNIVERSITY OF SUSSEX

Jonathan Daniel Crofts, D.Phil.

Analytical Modelling of Multi-Spacecraft Reconnection Layer Measurements at the Magnetopause

ABSTRACT

An approach to determine and analyse the structure of Petschek-type magnetic reconnection is developed. This is achieved by extending an analytical model based on the Rankine-Hugoniot wave equation for shock jump conditions and is described in terms of its past applications and limitations. The model is applied to data from the CLUSTER multi-spacecraft mission using a boundary condition method optimised by two interlinked genetic algorithms.

Case studies for a range of locations within the magnetopause region and local conditions are described and subjected to fluid and particle analyses to confirm the presence of reconnective signatures. Genetic algorithms are used to optimise the fit of the model, by modifying the boundary condition selection and internal structure parameters. This information then facilitates the construction of a more accurate modelled layer structure for each event. The calculated values for state variables within these layers are compared quantitatively and qualitatively to the magnetopause boundary crossings present in the CLUSTER data. Case study results are summarised and compared before being compiled into quantitative statistics for describing the local and possibly global applicability of the model.

The fast application of these methods by means of an automatic process to a large set of data is described, as are the wider possibilities arising from this and the limitations of model, methods and data.

These results are used to support several assertions. Firstly, that this model is indeed applicable, within its limitations, to the study of reconnection events within the magnetospheric environment. It can also facilitate deeper studies of individual reconnection events, in addition to being employed as a basis to classify wider statistical trends in spatio-temporal structures.

Contents

Chapter 1

Introduction

1.1 The Solar-Terrestrial Environment

1.1.1 The Plasma Medium

As the 4th state of matter, a plasma is defined as a charged particle medium that exhibits collective behaviour. Most space plasmas are assumed, for the purposes of analysis, to be quasi-neutral. Quasi-neutrality is described as the presence of equal proportions of electrons and ions in the plasma medium on average. This property, combined with the high electron mobility, in comparison to ion species, leads to the ability of a plasma to shield its coulomb potentials from the wider space environment. This "Debye shielding" is the process by which electric (coulomb) fields are screened from within the medium by the rearrangement of the charged particles within the plasma. It takes place in response to the standing, up to electron and ion plasma frequencies and spatial scales, coulomb electric potentials existing due to the presence of the other charged particles. This rearrangement effectively cancels potentials felt outside of a certain radius from a particular centre point based on number density and kinetic temperature.

The collective behaviour of the plasma medium gives rise to wave effects. Many of these waves are inherent to the medium in its unperturbed state, however those that are most of interest in this study are those that are driven by external perturbations

to the medium.

1.1.2 The Origin of the Solar Wind

Fusion taking place within the core of the Sun continuously liberates large amounts of nuclear energy. This energy is transported through the strata that comprise the sun by radiative and convective processes. This radial transport allows the Sun to remain in a generalised state of hydrostatic equilibrium with respect to the wider space environment. At the solar surface and out into the corona plasma is heated and accelerated outwards to form a highly tenuous medium. This is the Solar Wind.

The existence of the Solar Wind was first postulated by those (Lodge, 1900; Biermann, 1951) who, after investigating the nature of cometary tails, suggested that their direction could not be explained purely in terms of particle acceleration due to interaction with solar radiation as the interaction cross-section of many of the particle species was too small to account for the scale of the effect. The proposed "solar corpuscular radiation" was comprised of ionised material that we would later come to term "a plasma" (Langmuir, 1929). With the advent of satellite missions this plasma could now be observed and studied in situ.

1.1.3 Properties of the Solar Wind

The properties of the Solar Wind have been extensively studied since the early days of space exploration, upon confirmation of the existence of the Solar Wind by the Soviet Luna 1 probe in 1959.

The Solar Wind, as it reaches the Earth's orbit is considered to be a collisionless medium. For this quality to be applied the mean free path (the average distance between binary collisions) has to be large in comparison to the length scale of the medium itself. The mean free path for an electron in a plasma is given in (Baumjohann and Treumann, 1996) by:

$$\lambda_e = \frac{64\pi n_e}{\omega_{pe}^4 ln\Lambda} \left(\frac{k_B T_e}{m_e} \right)^2 \tag{1.1}$$

Where n_e is the electron number density, k_B is the Boltzmann constant, T_e is the electron kinetic temperature, m_e is the electron mass, $ln\Lambda$ is the coulomb logarithm and denotes the logarithm of the ratio between the maximum and minimum impact parameters for the coulomb interaction and ω_{pe} is the electron plasma frequency given in (Kivelson and Russell, 1995) by :

$$\omega_{pe} = \sqrt{\frac{n_e e^2}{\varepsilon_0 m_e}} \tag{1.2}$$

Where e is the charge on an electron and ε_0 is the permittivity of free space. Typical parameter values for solar wind plasma at 1AU are as below in Table 1.1.

Parameters (units)	Value
Velocity (km/s)	450
Proton Density (particles/cm^3)	6.6
Electron Density (particles/cm^3)	7.1
Proton Temperature (10^5K)	1.2
Electron Temperature (10^5K)	1.4

Table 1.1: Typical parameter value ranges for the plasma that comprises the solar wind at 1AU (Kivelson and Russell, 1995)

With values for the coulomb logarithm ranging from 5-15 (Baumjohann and Treumann, 1996), and using the above values it is possible to see that λ_e is approximately equal to $10^8 m$ or 1AU. Thus it is possible to say that since an electron may undergo only a single high deflection collision in the interval between emission from the solar surface and reaching the Terrestrial Bow Shock the medium itself may be regarded as being collisionless.

1.1.4 The IMF and the "Frozen in Flow" Condition

The plasma in the outer reaches of the solar atmosphere is threaded with the magnetic fields from solar sources such as dynamo generation, active region emergence and solar flare activity. In the solar atmosphere and solar wind the diffusion of this magnetic field through the plasma is governed by the conductivity of the plasma in question.

The generalised plasma scalar conductivity for a dilute, fully ionized plasma is given, in Baumjohann and Treumann (1996), by:

$$\sigma_0 = \frac{n_e e^2}{m_e \nu_c} \tag{1.3}$$

Where e is the electron charge, n_e is the electron number density, m_e is the electron mass and ν_c is the collision frequency.

As the collisional frequency decreases the conductivity increases. So in a medium with a large mean-free path length (in comparison to the number density) the conductivity will be high. In this case the general form of Ohm's law can be rearranged to give, from Kivelson and Russell (1995):

$$\mathbf{j} = \sigma(\mathbf{E} + \mathbf{v} \times \mathbf{B}) \tag{1.4}$$

Which, as σ tends to infinity, can only be true if $(\mathbf{E} + \mathbf{v} \times \mathbf{B}) = 0$. What this suggests is that, over a time period that is large in comparison to the length of time a particle needs to react to a standing electric field (the plasma frequency f_{pe}), any unmoving plasma cannot contain any standing electric field. And in turn if the plasma is in motion then there will be an electric field acting orthogonally to the directions of the magnetic field and bulk velocity.

Using the Maxwell equations for a generalized magnetised fluid we can arrive at an equation describing the evolution, with respect to time, of the magnetic field. This relation, and the following derivation, are presented in (Baumjohann and Treumann, 1996):

$$\frac{\partial \mathbf{B}}{\partial t} = \nabla \times (\mathbf{v} \times \mathbf{B}) + \frac{1}{\mu_0 \sigma_0} \nabla^2 \mathbf{B} \tag{1.5}$$

The right hand side of equation 1.5 contains two terms. The leftmost term contains convective factors, whereas the other is a rest term. If the plasma is assumed to be at rest ($\mathbf{v} = 0$) then the equation becomes:

$$\frac{\partial \mathbf{B}}{\partial t} = \frac{1}{\mu_0 \sigma_0} \nabla^2 \mathbf{B} \tag{1.6}$$

Which can then be compared with the general diffusion equation below:

$$\frac{\partial \phi}{\partial t} = D \nabla^2 \phi \tag{1.7}$$

Equation 1.7 suggests that the rest term from equation 1.5 describes magnetic diffusion through the plasma with the diffusion coefficient $D_m = \frac{1}{\mu_0 \sigma_0}$. The presence of the conductivity in this as the primary variable suggests that magnetic diffusion takes place when the conductivity is not infinite (as $D_m \to 0$) but when the plasma is resistive leading to the homogenization of structure.

As the conductivity of the plasma tends towards infinity the amount of magnetic flux through a surface becomes a conserved quantity as the magnetic field is unable to diffuse through the plasma. While this condition is maintained the field follows any deformations applied to the plasma matter due to non-uniform flow within the medium and vice versa.

As a measure for the relative effect of kinetic or field pressures on the plasma the plasma beta β is defined as the ratio of the former to the latter (Kivelson and Russell, 1995). This relation is shown in equation 1.8, where P_P is the plasma thermal pressure, P_B is the magnetic pressure, B is the magnetic field strength and μ_0 is the permeability of free space. To a first approximation in a non-dissipative, collisionless, ideal Magnetohydrodynamic picture this quantity is conserved through fluid deformation of the solar wind medium. This also applies to similar regions where these simplifications apply. This may not be the case in a system showing significant pressure anisotropies as these cause β to split into parallel and perpendicular terms relating to parallel and perpendicular thermal pressures.

$$\beta = \frac{P_P}{P_B} = \frac{P_P}{\left(\frac{B^2}{2\mu_0}\right)} \tag{1.8}$$

In the solar wind, the collisional frequency ($\nu_c \to 0$) tends towards zero, with

interactions taking place, primarily, through the medium of electromagnetic fields. This means that the conductivity (Eqn. 1.3) tends towards infinity ($\sigma_0 \rightarrow \infty$). In this situation the solar magnetic field is unable to diffuse through the plasma medium quickly, and thus is said to be "frozen in". This approximation allows for the modelling of the outflowing material as it convects out into the solar-terrestrial environment, carrying the Sun's magnetic field with it and forming the Interplanetary Magnetic Field (IMF).

Parker, in 1959, described the solar wind plasma carrying the magnetic field of the sun radially outwards while the sun rotates. The three dimensional projection of this motion leads to the multi-pole magnetic field of the sun forming what has become known as the Parker Spiral (Parker, 1959). It is a local fragment of this larger structure that later reaches the planets and interacts with their magnetospheres. An illustration of this Parker Spiral structure is presented in Figure 1.1.

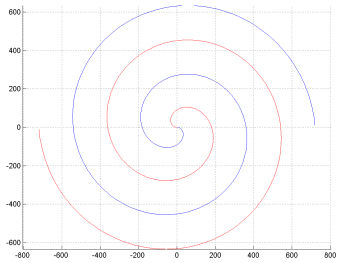

Figure 1.1: Sun polar representation of the field expansion in the Parker Spiral formed by the solar magnetic field being carried by the solar wind.

1.1.5 Solar Wind to Magnetospheric Coupling.

As the plasma carrying the IMF reaches planets with an inherent magnetic field, such as the Earth or Jupiter, interactions between these fields and the magnetospheric plasma environments of those planets take place.

There is, therefore, a hydrostatic equilibrium where the inward pressure of the solar wind is balanced by the combined outward pressure of the magnetic and plasma pressures of the planetary environment it is impinging upon. This point is that planet's magnetopause. Within the confines of this boundary lies the magneto-

sphere. The Earth's magnetosphere is the region that is primarily subject to the dominance of the Earth's magnetic field (Kivelson and Russell, 1995).

Upwind of the planet in question or the direct boundary between solar wind and local magnetosphere lies the bow shock. The fast mode wave transmits information about the presence of the magnetopause boundary to the inflowing solar wind plasma. As the solar wind flow is supersonic compared to the local sound speed of the fast mode wave in the plasma fluid a shock forms. This shock is the bow shock.

The solar wind contacts the bow shock some 15-10 RE sunward of the Earth and at this boundary it is heated and compressed as it is slowed and diverted around the body of the Earth. The region of shocked plasma is known as the magnetosheath and lies between the bow shock and the magnetopause. These boundaries are illustrated using a model magnetopause and bow shock in Figure 1.2.

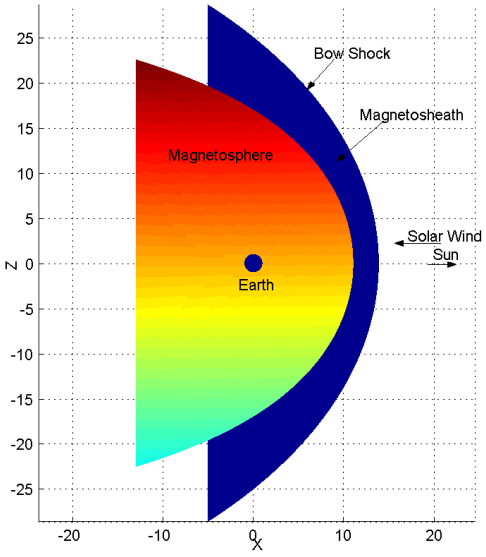

Figure 1.2: A simplified representation of the elements of the local Earth environment as the solar wind flows past the Earth, including the location of the bow shock, magnetosheath and magnetopause.

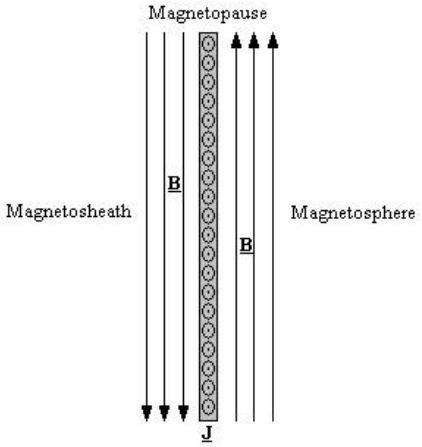

Figure 1.3: A simple schematic diagram of the current layer at the intersection of the solar wind-magnetosheath (southward) and magnetospheric (northward) magnetic fields.

The structure of the magnetopause has been described in terms of a current layer resembling a rotational or tangential discontinuity as it evidences rotation of the magnetic field direction from the magnetosheath to the magnetosphere plasma region. This current layer may be several ion gyro-radii thick (Russell, 2003). This

simple geometry is shown in Figure 1.3.

In general the plasma populations comprising the two environments are segregated.

In the absence of turbulence, drifts or gradients the particles that comprise a plasma are confined to travel along a guiding centre path in the direction of the magnetic field, along field lines. Because of this magnetisation property, described macroscopically by the frozen-in-flux approximation, little or no intermixing takes place between adjacent bodies of plasma with unlike parameters. This separation forms the so called "sector" or "cell" structure of the plasma environment (Kivelson and Russell, 1995).

Since there is no obvious flow of plasma through this boundary a problem arises. Injected magnetosheath plasma material has been observed in the magnetosphere (Bauer et al., 2001; Russell, 2003) in addition to the presence of auroral precipitation and substorms. A possible mechanism to achieve this coupling between these two regions comes about through the violation of this condition. An illustration of this possibility comes about through reference to the local Magnetic Reynolds number, R_m, as defined below (Baumjohann and Treumann, 1996; Kivelson and Russell, 1995).

$$R_m = \mu_0 \sigma_0 L_B V_\perp \tag{1.9}$$

The Magnetic Reynolds number, R_m, is the ratio of the strength of magnetic field convection to field diffusion, where σ_0 is the plasma conductivity, L_B is the characteristic length over which the magnetic field varies and V is the bulk velocity perpendicular to the magnetic field. If the value for $R_m \gg 1$ then diffusion effects can be safely ignored, if $R_m \ll 1$ then the magnetic field diffuses quickly enough that convection is negligible. The former is obviously present in the solar wind where σ_0, L_B and V are all high. However, near the magnetopause all of these quantities see a significant decrease in their value as

- The length scale associated with magnetic variation across the sheet decreases

dramatically.

- The plasma decelerates.

Reconnection occurs at regions where it is energetically advantageous, and physically allowable to do so. The process is characterised by the diffusion, annihilation and consequent topological reorganisation of the magnetic field as the plasma and field become decoupled from one another. In MHD terms, this is where the frozen-in-flux approximation fails and is no longer applicable. In this case, over the magnetopause current layer.

1.2 Plasma behaviour and MHD

1.2.1 The Basis of Magnetohydrodynamics

Magnetohydrodynamics (MHD) is a mathematical formalism that, by incorporating aspects of electromagnetic field and flow behaviour, allows the description of a body of plasma in terms of the evolution of macroscopic quantities through a set of equations describing the conservation of mass, momentum and energy.

Therefore MHD does not so much deal with particle distribution functions, as kinetic theory does, but rather with the moments of those functions; quantities like the magnetic field vector, velocity, number density and temperature.

An MHD model can be constructed with several degrees of simplification. For example the plasma can be treated as simply as taking an electrically neutral fluid subject to magnetic forces, or can be expanded to take each species as a separate fluid and construct the model from there.

The basic equations of MHD can be derived in several different ways. One method is the integration of the kinetic equation for a collisionless plasma, the Vlasov equation below, with respect to velocity space (Kivelson and Russell, 1995; Baumjohann and Treumann, 1996). By using the Vlasov equation in this way it is being assumed that the distribution function for the plasma is a Maxwellian. While

this is not the case in much of the solar-terrestrial environment, as the plasma is not strongly collisional, the MHD formalism can give a useful qualitative insight into the behaviour of certain systems.

$$\frac{\partial f}{\partial t} + \mathbf{v} \cdot \nabla_x f + \frac{q}{m}(\mathbf{E} + \mathbf{v} \times \mathbf{B}) \cdot \nabla_v f = 0 \tag{1.10}$$

The moments of this equation are the Magnetohydrodynamic equations that follow, these have been reproduced from (Baumjohann and Treumann, 1996). The first of these is equation 1.11, the Continuity Equation:

$$\frac{\partial n_s}{\partial t} + \nabla \cdot n_s \mathbf{v}_s = 0 \tag{1.11}$$

Where n_s is the number density for particle species s and $\mathbf{v}_s$ is the bulk flow velocity for that species. The continuity equation specifies that the number of particles in the system of species s during time t is purely a function of the divergence of the mass density, number density multiplied by the bulk velocity vector.

The second equation in the set is that governing the conservation of momentum density, equation 1.12, the Momentum Equation:

$$\frac{\partial (n_s \mathbf{v}_s)}{\partial t} + \nabla \cdot (n_s \mathbf{v}_s \mathbf{v}_s) + \frac{1}{m_s} \nabla \cdot \mathbf{P}_s - \frac{q_s}{m} n_s (\mathbf{E} + \mathbf{v}_s \times \mathbf{B}) = 0 \tag{1.12}$$

The left hand term describes the change in flux density with respect to time, working right the next describes the divergence of the energy density across the surface of the volume in question, next comes a term for the kinetic pressure gradient and last is the Lorentz equation for a number of particles (n_s) subject to electric and magnetic fields. The two left hand terms therefore describe the movement of momentum energy through the system bounds and the right two are source/sink terms acting within the system. The equation describing the total energy of the system is equation 1.13 the Energy Equation:

$$\frac{3}{2}n_s k_B \left(\frac{\partial T_s}{\partial t} + \mathbf{v}_s \cdot \nabla T_s\right) + p_s \nabla \cdot \mathbf{v}_s = -\nabla \cdot \mathbf{q}_s - (\mathbf{P'}_s \cdot \nabla) \cdot \mathbf{v}_s \tag{1.13}$$

Where T_s is the temperature, derived from the velocity distribution function as defined below in equation 1.14, p_s is the species scalar pressure, q_s is the heat flux vector and $\mathbf{P'}_s$ is the shear stress part of the full pressure tensor.

$$T_s = \frac{m}{3k_B n} \int (\mathbf{v} - \mathbf{v}_b)(\mathbf{v} - \mathbf{v}_b) f(\mathbf{v}) d^3 v \tag{1.14}$$

As each of these equations contains an unknown in the form of the next moment of the Vlasov equation they do not, in themselves, comprise a closed set of equations. To close the set, an equation of state is used.

In the case of an isotropic pressure system the Pressure Tensor ($\mathbf{P}_s$) becomes diagonal in that for plasma species s:

$$\mathbf{P}_s = \begin{pmatrix} p_s & 0 & 0 \\ 0 & p_s & 0 \\ 0 & 0 & p_s \end{pmatrix} \tag{1.15}$$

The isothermal case is defined as being when the temperature variations are of sufficient tduration that the plasma has time to carry out interactions to maintain a constant heat bath temperature. This specification then allows the use of the ideal gas law to close the system of equations:

$$p_s = n_s k_B T_{s0} \tag{1.16}$$

Where T_{s0} denotes the aforementioned long time scale heat bath temperature onto which short term variation is imposed. In the non-isothermal case the fluid then can be shown to behave adiabatically and the required state equation then becomes:

$$p_s = p_{s0}\left(\frac{n_s}{n_{s0}}\right)^{\gamma} \tag{1.17}$$

The treatment for an anisotropic pressure tensor is somewhat more complex and is beyond the scope of this investigation, the result, however is that field-parallel and perpendicular pressures are treated separately and produce separate equations of state:

$$p_{s\parallel} = p_{s\parallel 0}\left(\frac{n_s}{n_{s0}}\right)^{3} \tag{1.18}$$

$$p_{s\perp} = p_{s\perp 0}\left(\frac{n_s}{n_{s0}}\right)^{2} \tag{1.19}$$

With the addition of particulate and media properties to the field quantities of the Maxwell equations a new set of modifications to those relations describing the behaviour of the plasma are required, giving rise to a MHD form of Maxwell's Equations:

$$\nabla \times \mathbf{B} = \mu_0 \mathbf{j} \tag{1.20}$$

$$\nabla \cdot \mathbf{j} = 0 \tag{1.21}$$

$$\frac{\partial \mathbf{B}}{\partial t} = -\nabla \times \mathbf{E} \tag{1.22}$$

$$\mathbf{j} = \sigma\left((\mathbf{E} + \mathbf{u} \times \mathbf{B}) + \frac{1}{n_e}\nabla p_e - \frac{1}{n_e}\mathbf{j} \times \mathbf{B} - \frac{m_e}{ne^2}\left[\frac{\partial \mathbf{j}}{\partial t} + \nabla \cdot (\mathbf{ju})\right]\right) \tag{1.23}$$

$$-\nabla \cdot \mathbf{q} = \frac{\partial}{\partial t}\left[nm\left(\frac{1}{2}v^2 + w\right) + \frac{B^2}{2\mu_0}\right] \tag{1.24}$$

$$\frac{dS}{dt} = \frac{\partial S}{\partial t} + \mathbf{v} \cdot \nabla S = 0 \tag{1.25}$$

The above equations 1.20-1.23 give Ampere's law, divergenceless current density, Faraday's law and Ohm's law respectively. Equation 1.24 is the conservation of energy relation where the quantity w denotes the internal energy. The final relation, a rewritten form of 1.24, is the conservation of entropy, S.

1.2.2 Single and Multi-Fluid MHD

The previous equations describe a plasma of any species. In this fashion it is possible to formulate equations for each species comprising the plasma. This is Multi-Fluid MHD. Or, we can assume that the plasma is an electrically quasi-neutral fluid effectively comprised of ions; most usually protons.

In this case it has been shown, in (Baumjohann and Treumann, 1996), that it is possible to recast the earlier equations in terms of the single fluid. The Continuity Equation (Eqn 1.11) therefore becomes:

$$\frac{\partial n}{\partial t} + \nabla \cdot n\mathbf{v} = 0 \tag{1.26}$$

This equation now represents the continuity of classical mass with respect to time within a defined surface. The momentum equation becomes an Equation of Motion:

$$\frac{\partial (nm\mathbf{v})}{\partial t} + \nabla \cdot (nm\mathbf{v}\mathbf{v}) = -\nabla \cdot \mathbf{P} + \rho\mathbf{E} + \mathbf{j} \times \mathbf{B} \tag{1.27}$$

To close this new system of equations the momentum equation can again be manipulated to provide us with a generalized Ohm's law for single fluid MHD.

$$\mathbf{E} + \mathbf{v} \times \mathbf{B} = n\mathbf{j} + \frac{1}{n_e}\mathbf{j} \times \mathbf{B} - \frac{1}{n_e}\nabla \cdot \mathbf{P}_e + \frac{m_e}{ne^2}\frac{\partial \mathbf{j}}{\partial t} \tag{1.28}$$

The previously described energy conservation equation can be brought into this scheme. This expression contains the frozen-in-condition and as such specifies the further simplifications for its application.

To further simplify these equations assumptions are made to render these MHD equations into the ideal MHD equations.

The plasma is assumed to be non-dissipative and infinitely conducting in the limit of length and time scales significantly larger and longer than those required for particle dynamic processes. This allows for the assumption of Maxwellian particle distributions brought about through collisions or other dispersive mechanisms.

1.2.3 Waves and Shocks

These equations from (Baumjohann and Treumann, 1996), define the ideal MHD system and can be explored in terms of the waves and discontinuities that interacting plasma populations can generate. They give rise to several modes of wave behaviour that are analytically useful and have been confirmed through observation in the solar-terrestrial environment.

Based on the assumption that variations in the magnetic field are small in comparison to the strength of the field itself the ideal MHD equations are linearised and homogenised.

Alfvén Waves

The shear Alfvén wave is a field-parallel, purely transverse, non-dispersive MHD wave mode and has been observed in situ (Coleman et al., 1960). It is the primary magnetoacoustic wave. The Alfvén wave velocity (group and phase) magnitude is given in (Kivelson and Russell, 1995) by:

$$V_A = \frac{B}{\sqrt{\mu_0 \rho}} \tag{1.29}$$

This is the magnetic sound speed and corresponds to the velocity at which the wave propagates field-line perturbations (group and phase) along magnetic field lines. The Alfvén wave results in propagating perturbations in the transverse magnetic field, electric field, the plasma velocity and current density while leaving the plasma pressure and density unchanged. As such it is as non-compressional wave.

Slow Mode Waves

The slow mode magnetosonic/magnetoacoustic wave is also, in a similar fashion to the Alfvén wave, unable to propagate perpendicular to magnetic field lines, i.e. the group velocity, V_g, is field aligned. It is characterised by variations in the plasma and magnetic field pressures that are out of phase with one another. The slow mode wave, as a compressional wave, propagates perturbations in density and magnetic

field magnitude in addition to those seen in the Alfvén wave. The group and phase velocities for the slow mode wave vary from those seen in the Alfvén wave and are dependant on θ, the angle between the wave propagation vector ($\mathbf{k}$) and the magnetic field.

The slow mode wave undergoes significant attenuation in high beta environments whereas in low beta the slow mode wave is an acoustic wave modified by the magnetic field.

Fast Mode Waves

The fast mode magnetosonic/magnetoacoustic waves are compressional waves that are generated in locations where the total system pressure changes, this pressure gradient drives the production of these waves which then propagate these pressure variations out into the medium. The fast mode is differentiated from the slow mode behaviourally by the fact that the variations in plasma pressure and magnetic field pressure occur in phase. Structurally they are distinct as fast mode waves are able to propagate in any direction and are not confined to field-aligned (Alfvén) or field-guided (slow mode) geometries.

Shocks and Their Effects

Shocks are non-linear structures that occur and have been observed throughout the solar-terrestrial environment. A shock can be formed in many ways, possibilities include: the steepening of a large amplitude MHD wave mode, the intersection of a supersonic fluid flow with a subsonic fluid flow or the passage of either a supersonic object through a subsonic medium or a supersonic fluid flowing into and around a subsonic, or stationary, object. At a shock, supersonic fluid flow is converted through non-adiabatic dissipative mechanisms into thermalised subsonic flow.

The primary defining factors for shock type selection are the shock strength and the angle (θ_{Bn}) between the shock front and the local upstream magnetic field (Kivelson and Russell, 1995). The magnetic field orientation may be classified in

terms of angular ranges corresponding to parallel, quasi-parallel, oblique, quasi-perpendicular and perpendicular depending on the θ_{Bn}.

A shock is labelled as parallel or quasi-parallel when the plasma bulk velocity both upstream and downstream of the shock is either field aligned and normal to the shock front (parallel), or where $\theta_{Bn} < 45°$ (quasi-parallel). Cross-field shocks, where the plasma flow is at an angle to both the magnetic field and the shock front, are labelled perpendicular when $\theta_{Bn} = 90°$ and quasi-perpendicular when $\theta_{Bn} > 45°$. The term oblique has been used to describe both the region between quasi-parallel and quasi-perpendicular orientations as well as the entire region that is neither exactly perpendicular nor exactly parallel (Kivelson and Russell, 1995).

In addition to categorising behaviour by geometric orientation an additional distinction is made on the basis of shock strength. The internal strength of a shock can be quantified using a comparative Mach number, the ratio of flow velocities upstream and downstream of the shock. Supersonic structures and flows may be highlighted using another Mach number, which is calculated by taking the ratio of the flow velocity to the characteristic information propagation speed for a shock. Since the Alfvén velocity in a plasma is the equivalent of the magnetic sound speed, the commonest Mach number used is the Alfvén Mach number, see equation 1.30:

$$M_A = \frac{V_{flow}}{V_A} \tag{1.30}$$

The largest locally observed shock is the bow-shock. This fast-mode shock has been studied in detail since the advent of in situ data (Farris and Russell, 1994; Merka et al., 2005). In addition other shock types have been confirmed through measurements taken by the ISEE, AMPTE and CLUSTER missions on multiple occasions, including but not limited to the following (Walthour et al., 1995; Bauer et al., 2001; Eriksson et al., 2004).

1.2.4 The Rankine-Hugoniot Jump Conditions

The Rankine-Hugoniot jump conditions are equations describing the continuity of macroscopic variables across a discontinuity boundary in a fluid (Rankine, 1870; Hugoniot, 1887, 1889). They are quantified in terms of upstream and downstream values of state variables and when applied to a magnetised plasma medium are represented, in their general form, below:

$$m\left[\frac{1}{\rho}\right] = [v_n] \tag{1.31}$$

$$m[v] + \hat{n}[p] + \hat{n}\langle B\rangle \cdot \left[\frac{B}{\mu_0}\right] - B_n\left[\frac{B}{\mu_0}\right] = 0 \tag{1.32}$$

$$m\langle\frac{1}{\rho}\rangle[B] + m\left[\frac{1}{\rho}\right]\langle B\rangle - B_n[v] = 0 \tag{1.33}$$

$$m\left(\left[\frac{p}{\rho}\right](\gamma-1)^{-1} + \left[\frac{1}{\rho}\right]\langle p\rangle + \left[\frac{1}{\rho}\right]\frac{[B]^2}{4\mu_0}\right) = 0 \tag{1.34}$$

$$[B_n] = 0 \tag{1.35}$$

Where for any particular quantity $[X]$ is defined as $(X_2 - X_1)$, i.e. the change across the discontinuity and $\langle X\rangle$ is the average value $\frac{X_1+X_2}{2}$. The jump conditions for specific types of discontinuity can be derived using different approaches:

- by applying constraints describing the defining qualities of the wave mode or discontinuity in question based on the MHD relations, dispersion or otherwise, for that mode.
- from the solutions of the determinant of the equation of state of the Rankine-Hugoniot equations.

An important distinction to be made is that the jump conditions apply to the initial and final states of the variables, up and downstream of the discontinuity. They do not specify the internal mechanics of the discontinuity itself.

1.3 Reconnection Theory

Reconnection was described by Dungey in 1961 in terms of auroral particle acceleration at magnetic field neutral points formed where the IMF and geomagnetic field intersected with anti-parallel field configurations (Dungey, 1961).

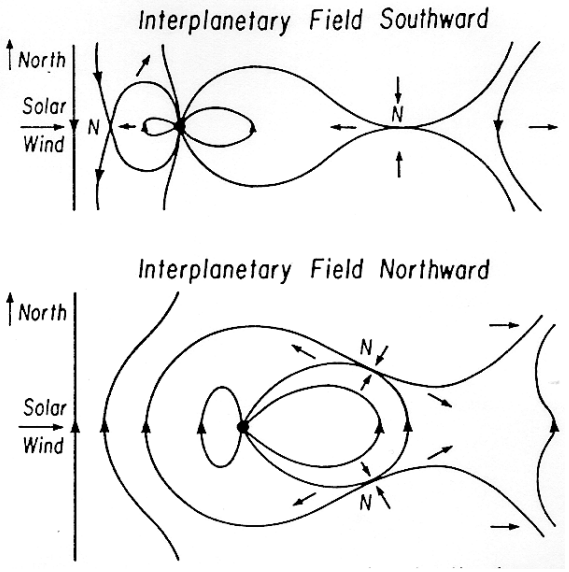

Figure 1.4: Dungey's original diagram depicting magnetic reconnection in the magnetosphere.

The current sheet that forms at the intersection of two magnetic regions, such as flux tubes, forms a boundary like that described in this original theory, the physical structure of which is illustrated in Figure 1.4. Since then much work has been done to describe locations where reconnection takes place such as in solar flares and at the magnetopause (Vaivads et al., 2004) or in the magnetotail (Eriksson et al., 2004), the frequency of such events and the mechanisms precipitating them (Eastwood, 2008).

The switch-on process of magnetic reconnection has not been comprehensively defined.

It is, however, reasonable to suggest, in general terms, that magentic diffusion and field annihilation take place under certain conditions such as when a current layer grows thin enough for the characteristic length scale of the magnetic variation across the boundary becomes very small. In theory terms such a situation might

be described in terms of the failure of MHD, in general, and of the frozen-in-flux approximation in particular (Semenov et al., 1992a). The reconnection process liberates energy stored in the local magnetic field which, in the presence of a classically resistive or anomalously (possibly MHD wave driven) resistive current, is then converted into thermal kinetic energy by the local plasma population giving rise to high speed plasma jets directed away from the reconnection site (Paschmann et al., 1979) as well as features in the distribution functions of the particle populations.

The diffusion region is, by definition, a region in which magnetic field diffusion becomes an important process. The plasma is then considered to be demagnetized. Physically it is considered to be a small region in which there is an electric field due to charge separation from the differential demagnetization of ion and electron species and a change in the magnetic field conductivity leading to a reorganisation of the local magnetic topography (Mozer et al., 2002). The new magnetic structure usually includes a non-zero magnetic field component in the direction of the magnetopause normal (B_N) that allows the particle populations to mix by travelling in a field aligned direction, along what can be thought of as reconnected field lines in this reorganised magnetic topology. Processes such as the relaxation of magnetic field tension and acceleration due to the reconnection electric field lead to acceleration of the particles comprising the plasma into reconnection "jets" that extend away from the diffusion region along the reconnection layer/magnetopause surface.

Although most models consider the above as generally true, due to observational evidence, the method of explanation of this behaviour differs.

1.3.1 Sweet and Parker Reconnection

The description that has come to be known as the "Sweet-Parker model" was suggested in 1957 and 1958 separately by Peter Sweet and Eugene Parker.

The simplest, historically first, theoretical framework for reconnection, the Sweet-Parker model is structurally uncomplicated. Figure 1.5 indicates the basic structure of the transition region, assuming a two-dimentional geometry. The magnetic field

lines in this case are indicated along with their orientation. The magnetosheath-side Interplanetary Magnetic Field (IMF) is shown on the left to be southward while the magnetosphere-side geomagnetic field is on the right and is orientated northward. The grey region in the centre is the previously mentioned diffusion region, with plasma flowing into it along the directions indicated with velocity **U**. Outflowing plasma is represented here at the top and bottom of the image with the velocity vectors, **V**.

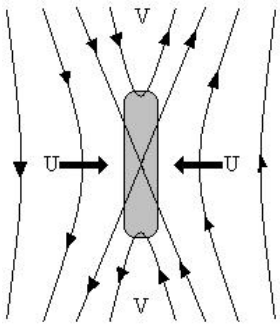

Figure 1.5: A schematic diagram of the Sweet-Parker scheme for reconnection detailing reconnection seperatrices, the diffusion region, inflow and outflow regions.

A defining descriptor of the Sweet-Parker model is that requires all the material in the in-flow regions to pass though a comparatively small diffusion region (as previously defined) where acceleration and thermalisation takes place (Kivelson and Russell, 1995). As this places a physical bottleneck in the plasma flow it is sometimes known as "slow-reconnection".

1.3.2 Petschek Reconnection

The Petschek model is, in essence, an attempt to extend the Sweet-Parker model. In a similar style to Figure 1.5, Figure 1.6 displays the basic structure of a two dimensional Petschek type reconnection region. The diffusion region, in this case, is comparatively considerably smaller and actually corresponds to the structure of the Sweet-Parker model in that all plasma passing through it along **U** undergoes post-demagnetised thermalisation in the same fashion. However in addition to this same basic structure with inflow, outflow and diffusion regions as the Sweet-Parker

model, energetic processes take place outside the diffusion region.

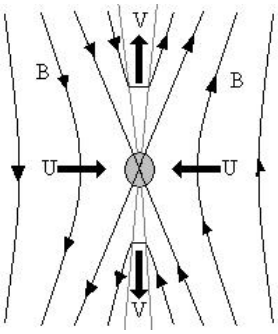

Figure 1.6: Diagram of a Petschek-type reconnection layer showing the reconnection x-line seperatrices and location of MHD wave modes, diffusion region, inflow and outflow regions.

The addition is in allowing large scale energy conversion to be carried out in standing MHD wave modes extending in an x-line topography from the central, small diffusion region to form magnetic seperatrices. At these standing waves magnetic field reorientation and conversion processes take place and the plasma passing through them is accelerated and thermalised. Alfvén waves achieve the required magnetic field vector rotation while slow mode waves or shocks accelerate the plasma (Kivelson and Russell, 1995). In this way a larger amount of plasma can pass through the reconnection region reducing the physical bottleneck in the Sweet-Parker model giving rise to this construction being attributed with "fast reconnection".

1.4 Riemann Boundary Layer Analysis

Riemann boundary analysis is defined as an initial value problem for a system of conservation law(s) in a piecewise data set and the formation of an analytical framework within which it can be solved.

A piecewise equation is one which has discontinuous values and behaviour depending on one or more input parameters. A simple example might be a pair of adjoining equations such as $y = x$ for $(x < 1)$ and $y = x^2$ when $(x \geq 1)$. In this case it is easy to see that although the equations define continous behaviour when taken together, they are themselves discontinuous. This discontinuity does not cause

problems when considered computationally as simple logical conditional statements can be used to select the correct equation for the parameters.

The parameter problem is solved, in this case, by the introduction of the boundary conditions from the observational data, which are used to define the nature of the structure as well as the quantitative behaviour in the layer interior. The boundary conditions are enumerated in terms of the value of two parameters: η and $|\mathbf{b}|$. η is defined as the ratio of upstream/downstream values of the magnetic field strength across a particular discontinuity, in this case a slow mode MHD wave. When enumerated, the parameter defines whether the slow mode MHD wave is resolved into a slow mode expansion fan or a steepened slow shock depending on two cases:

1. $\eta < 1$: There is a decrease in magnetic field strength which suggests the presence of a slow mode-shock component.

2. $\eta > 1$: The increase in magnetic field strength is taken to be a signifier of a slow expansion fan.

$|\mathbf{b}|$ on the other hand describes the magnetic coplanarity vector required for the two slow-mode waves. Increasing values of this parameter proportionally increase the complexity of the layer with respect to wave type. The precise mathematical behavour of both of these parameters is described in §2.5.2.

1.5 The CLUSTER II Observational Data

The four CLUSTER satellites carry a range of different instruments. Operational events have further affected the types of data available and thus the ways in which CLUSTER data can be used. A list of instruments used and basic information about them is presented in Table 1.2

1.5.1 The CLUSTER Ion Spectrometry (CIS) Instrument

The CLUSTER Ion Spectrometry suite (CIS) on the CLUSTER spacecraft is comprised of two component instuments: The COmposition and Distribution Function

Instrument	Measurement Type	Range	Time Resolution (s)
CIS - CODIF	Particle (3D composition)	25eV-40keV	4
CIS - HIA	Particle (3D distribution)	5eV-32keV	4
EFW	Electric Field (2D vector)	0.1mV/m-700mV/m	0.04
FGM	Magnetic Field (3D vector)	-4096nT ± 4096nT*	0.05

Table 1.2: Instrument Titles, Types, Range and Temporal Resolution for the CLUSTER II instruments used. [* Mode Selected range]

sensor (CODIF) and the Hot Ion Analyser (HIA) instrument.

CODIF provides compositional data for the plasma that the craft is passing through in a $360° \times 8°$ view within a 25eV/charge-40 keV/charge energy range. The data has a 22.5° angular resolution with the energy range being resolved into 31 energy bins with a $\frac{\Delta E}{E} \approx 0.14$ energy resolution.

The CODIF instrument selects species using a toroidal electrostatic analyser that differentiates by energy per charge by sweeping the voltage between the hemispheres in the analyser. These sweeps provide a partial distribution function, per polar angle, that is measured once every spin. The full function is compiled from these slices and thus is spin-resolution only.

The HIA instrument is similar in function to the CODIF instrument except that higher priority has been placed on having greater angular and time resolution across a greater dynamic range. As such the HIA's quadrispheric top-hat has an 180° view with angular resolution of 11.25° in each of the 8 sectors in each of the two sides to the instrument. The two sides are the low-sensitivity/gain (LS) and high-sensitivity/gain (HS). As such the former is primarily designed for use in the solar wind. Each spin, therefore, gives a full 360 distribution for each of these sensitivities across the 5eV/charge-32keV/charge energy range (Gloag et al., 2005).

The CIS instrument suite availability varies across the 4 CLUSTER spacecraft. Both CODIF and HIA are available on spacecrafts 1 and 3, CODIF alone is available on spacecraft 4 and neither are available on spacecraft 2.

1.5.2 The Electric Fields and Waves (EFW) Instrument

The Electric Fields and Waves (EFW) instrument is comprised of 4 spherical probes mounted orthogonally in the spin plane of the spacecraft so as to form two pairs of opposing probes at 90 degrees to one another. In this way the potential difference between two opposing probes can be used to measure the electric field in one vector direction, the same process being carried out with the orthogonal pair to provide the second vector in this plane.

The dynamic range over which the instrument is designed to measure is between 0.1 mV/m and 700 mV/m at a temporal resolution of 20 samples/second.

1.5.3 The Flux Gate Magnetometer (FGM) Instrument

The triaxial FluxGate Magnetometer (FGM) on each of the spacecraft provides full-time resolution data at 20 magnetic field vectors per second. The dynamic range, which is inversely proportional to the sensitivity, for these measurements is mode selected from 5 modes; 4 flight modes (2-5) and 1 test mode (7), with ranges from $\approx \pm 64nt$, $\approx \pm 256nT$, $\approx \pm 1024nT$, $\approx \pm 4096nT$ and corresponding sensitivities; $7.8 \times 10^{-3}nT$, $3.1 \times 10^{-2}nT$, $0.125nT$, $0.5nT$ and $8nT$ respectively.

However this is of significantly higher, by a power of ten, time resolution than any available ion data. As this analysis is based on equations that describe plasma medium changes in the order of a particle gyrotime such high resolution is not needed. For this reasons the choice was made to use the 5 magnetic field vectors/second data as this provides the required precision without introducing short term effects that are not considered or are averaged over in the analysis (Gloag et al., 2005). Early concerns about aliasing were raised and so comparison of 20Hz and 5Hz data has been carried out when possible in an attempt to minimize this possibility (Balogh et al., 2001).

The FGM instrument is currently operational on all 4 CLUSTER satellites.

1.6 The Signatures of Reconnection

1.6.1 Fluid Signatures

Several methods have been used to describe data bearing possible reconnection signatures. In 1979 confirmation of reconnection at the magnetopause, in terms of impulse acceleration, was observed in situ through examination of the velocity vector of the plasma (Paschmann et al., 1979). The vector had been tested against theoretical expectations using an application of the jump conditions for an Alfvén wave and examination of the net tangential Maxwell stress across the boundary. These and similar methods have been codified into widely applied quantitative measures since, including the use of de Hoffmann Teller (dHT) analysis, introduced in 1950 (de Hoffmann and Teller, 1950), (see §2.2), and Walen (tangential stress balance) analysis (see §2.3).

These macroscopic parameter variations and methods are considered to be indicative Fluid signatures of reconnection at a particular site (Paschmann and Daly, 1998). The mechanics of these methods is further explained in §2.2 and §2.3.

1.6.2 Particle Signatures

In addition to the macroscopic fluid signatures of reconnection microscopic indicators are also present. The nature of particle interactions with the magnetopause current layer have been studied both in theory (Cowley, 1982) and observation (Paschmann and Daly, 1998; Bauer et al., 2001; Phan et al., 2004; Retinò et al., 2005; Zheng et al., 2005). Considering the plasma populations near the magnetopause, both from the magnetosheath and the magnetosphere, a method commonly used to supply evidence for the occurrence of reconnection at a specific location is to examine velocity phase space distributions. In the localities bordering a reconnection region on either side of the magnetopause current layer specific D-shaped structures occurring as adjunct lobes to the deHoffmann-Teller velocity are visible. These highlight the reflection and transmission of magnetosheath and magnetospheric ion populations that are

either inflowing or outflowing from the magnetopause as well as the subsequent acceleration as they transition across a reconnection region. These populations are identified by specific compositional contributions and energy ranges characteristic of their source.

Chapter 2

Methodology

2.1 Boundary Normal Analysis

The data provided by the Cluster Active Archive (CAA) is in the Geocentric Solar Ecliptic (GSE) reference frame (Dandouras et al., 2005; Gloag et al., 2005). This frame defines the origin as the centre of the earth, the positive x-axis as sunward, the y axis as duskward in the ecliptic plane and the z axis aligned perpendicular to the ecliptic plane, orthogonal to the x and y axes.

To facilitate studying reconnection layers the data may be transformed into a frame defined by the layer itself rather than one defined by any other point, thus removing arbitrary constraints imposed by external coordinate systems. This approach allows for interpretation of vector data in terms of normal and perpendicular components with respect to the propsed layer and simplifies the model geometry considerably. It also allows analysis of layers as a group rather than individual cases. In most cases the frame is defined by a vector normal to the, assumed, planar surface of the crossing boundary; the boundary normal vector $\hat{\mathbf{N}}$.

Three methods have been applied to magnetopause crossing data in parallel to determine the boundary normal vector for any particular crossing. In the case of multiple transits of the same boundary results have been compared to try and compare and contrast local conditions and/or the accuracy of any one normal vector determination.

The three methods used are, in order of increasing complexity; Model Normal, Tangential Discontinuity and Minimum Variance Analysis.

2.1.1 Model Normal Method

The Model normal method is based around taking a surface defined by one or more magnetopause models, including Formisano 1979, Sibeck 1991 and Shue 1997, and taking the normal to the magnetopause at the spatial location where the spacecraft crossed this boundary. In this study use has been made of all previously listed models. Other models noted, but not currently used due to time constraints, were; Roelof and Sibeck 1993, Tsyganeko 1996 and Shue 1998. The resulting normal vectors have been compared and the mean taken as a purely geometric comparative value for the boundary normal as it does not take account of actual local conditions, such as surface waves generated at the reconnection site, which alter the normal vector attitude.

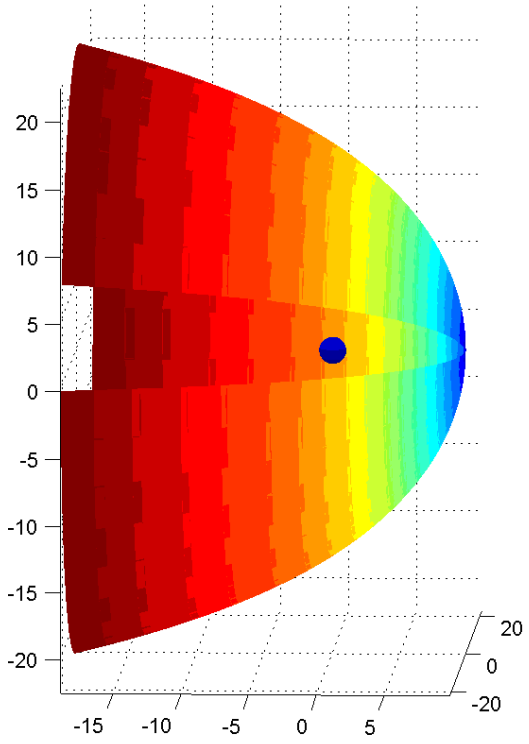

Figure 2.1: Model magnetopause based on the Shue et al. (1993) model.

2.1.2 Tangential Discontinuity Method

This method is predicated on the assumption that, for a purely tangential discontinuity, the magnetic field vectors upstream and downstream of the discontinuity will be parallel to the shock plane, and not each other. A possible example of this geometry is shown in Figure 2.2. A normalised vector cross product of the mean magnetic field vector on either side of the transition then provides a vector that is normal to both and thus, if the vectors do not share a significant parallel component, the assumed planar boundary itself (Paschmann and Daly, 1998).

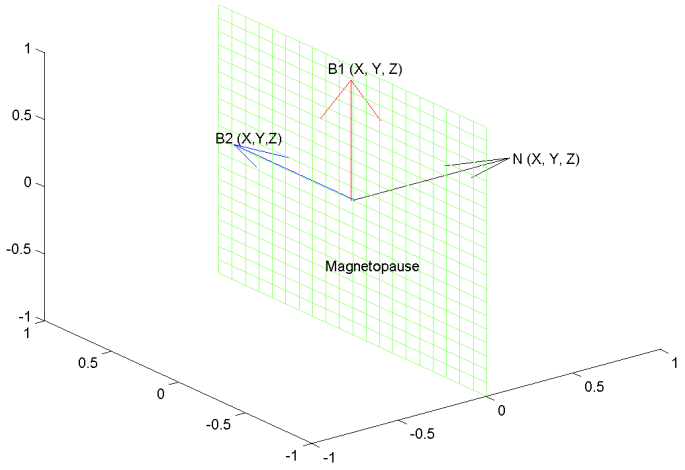

Figure 2.2: A sample magnetopause boundary (green) with magnetic field vectors before ($\boldsymbol{B_1}$) and after ($\boldsymbol{B_2}$) with an illustration of the resultant cross product normal vector ($\hat{\boldsymbol{N}}$)

$$\boldsymbol{B_1} = (B_{X_1GSE}, B_{Y_1GSE}, B_{Z_1GSE}) \tag{2.1}$$

$$\boldsymbol{B_2} = (B_{X_2GSE}, B_{Y_2GSE}, B_{Z_2GSE}) \tag{2.2}$$

$$\hat{\boldsymbol{N}} = \pm \frac{\boldsymbol{B_1} \times \boldsymbol{B_2}}{|\boldsymbol{B_1} \times \boldsymbol{B_2}|} \tag{2.3}$$

As this method relies on a single cross product of two vectors, it is not robust against local variations in those vectors. To decrease the sensitivity of this method

to the inherent variation in sampled magnetic field the arithmetic mean value of that field, in a period of stability in both field strength and direction on either side of the boundary, is used as an input to calculate the normal vector.

However, during periods of high variability in **B** or when the magnetic field vectors on both sides of the transition have significant parallel components then this method becomes increasingly less effective.

2.1.3 Minimum Variance Analysis Method

The Minimum Variance Analysis method was introduced by Sonnerup and Cahill (Sonnerup and Cahill, 1967).

If an idealised, one dimensional transition layer is considered such that the layer is aligned along the x-y plane, thus the only functionally variant direction is along the z axis, then using Maxwell's equation for the no magnetic monopole law we see that:

$$\nabla \cdot \boldsymbol{B} = \left(\frac{\partial B_x}{\partial x} + \frac{\partial B_y}{\partial y} + \frac{\partial B_z}{\partial z} \right) = \frac{\partial B_z}{\partial z} = 0 \tag{2.4}$$

So in making use of the property that across this boundary, in the direction normal to it, the divergence of the magnetic field vector should be zero. It is important to remember that under this condition alone B_Z is constant but not necessarily zero. It is possible to derive the normal vector to the boundary by finding the direction of least variance in the magnetic field vectors across it.

To do this the magnetic (co)variance matrix of the data is constructed, where elements are defined by:

$$M^B_{\mu\nu} = \langle B_\mu B_\nu \rangle - \langle B_\mu \rangle \langle B_\nu \rangle \tag{2.5}$$

Where the indices μ and ν describe the x, y and z components of the magnetic field in the eigenvalue equation:

$$\sum_{\mu,\nu=1}^{3} M^{B}_{\mu\nu} n_\nu = \lambda n_\mu \tag{2.6}$$

The eigenvalue solutions of this matrix equation correspond to the maximum (λ_1), intermediate (λ_2) and minimum (λ_3) variance of the magnetic field ($\sigma_{\mathbf{B}}$) in the direction described by the orthogonal eigenvectors. A measure, described in Paschmann and Daly (1998), of this orthogonality, and thus the applicability of the solution, is provided by taking the ratio of the intermediate and minimum eigenvalues ($\frac{\lambda_2}{\lambda_3}$) .

if $\lambda_2 \gg \lambda_3$ then the value of this ratio will be high ($\gg 1$). A high value denotes that the magnetic field evidences considerably greater variance in the direction of the intermediate solution than in the direction of the minimum variance vector solution calculated. A low value suggests that, as $\sigma_{\mathbf{B}}$ is similar along these two vector orientations, the calculated solution is degenerate and may not provide an accurate representation of the local conditions. This method is known as Minimum Variance Analysis of B Fields (MVAB), or when applied using a $B_N = 0$ constraint (MVABC).

The original method has been expanded upon and extended on several occasions, such as Sonnerup and Cahill in 1987 (Sonnerup et al., 1987), or Terasawa et al in 1996 (Terasawa et al., 1996) who suggested the method that would later come to be known as Minimum Faraday Residue (MFR) or in 1996 by Kawano and Higuchi who suggested extensions allowing in inclusion of electric field data into the determination of the normal vector direction (EBMVA) and a generalization of the method to apply to all boundary conditions (GMVA) (Kawano and Higuchi, 1997).

2.1.4 Application of Boundary Normal Analysis

The nature of the boundary normal frame for each spacecraft crossing for each of the events that make up each case is determined using a combination of methods. We take, as an initial criterion, that for a rotational discontinuity, or reconnection layer, the normal component of the magnetic field should have constant magnitude.

Using this we can apply statistical quantifiers to help select from within the set of normal vectors that are provided by the previously described methods. A simple linear fit of the normal component of the magnetic field would provide basic information over the transition. The gradient would describe the degree of agreement with the aforementioned condition and the offset would give a possible first order determination of B_N.

All three methods would be applied to each crossing case and then compared both graphically and statistically before the "best" was selected. This vector would then be used to transition of the vector data (B, V) from the GSE coordinate system into the required frame of reference with respect to the magnetopause boundary. In the frame defined by these new coordinate axes changes in magnetic field and plasma variables can then be used directly to describe this interaction layer in terms of the MHD wave modes that comprise the model.

2.2 de Hoffmann Teller Analysis

de Hoffmann and Teller, in 1950, examined, by means of jump conditions, the nature and behaviour of magnetohydrodynamic shocks (Paschmann and Daly, 1998).

Through this method they described a frame in which, when applied to a series of observations, the bulk velocity of the plasma is field aligned. The suggestion, should this construction prove accurate, is that there is a quasi-static flow and field based convecting structure such as a wave or current later within, what is in this case, the reconnection layer.

The presence of a quasi-static convecting structure gives rise to a convection electric field within the layer.

In the de Hoffmann Teller transformation frame this convective electric field vanishes when the bulk plasma velocity is transformed into a frame moving with the quasi-static structure. In this case electric field data can be obtained by two methods, either directly through instrumental measurement in situ or by derivation using ($E = -V \times B$) (Paschmann and Daly, 1998). The former method is preferable,

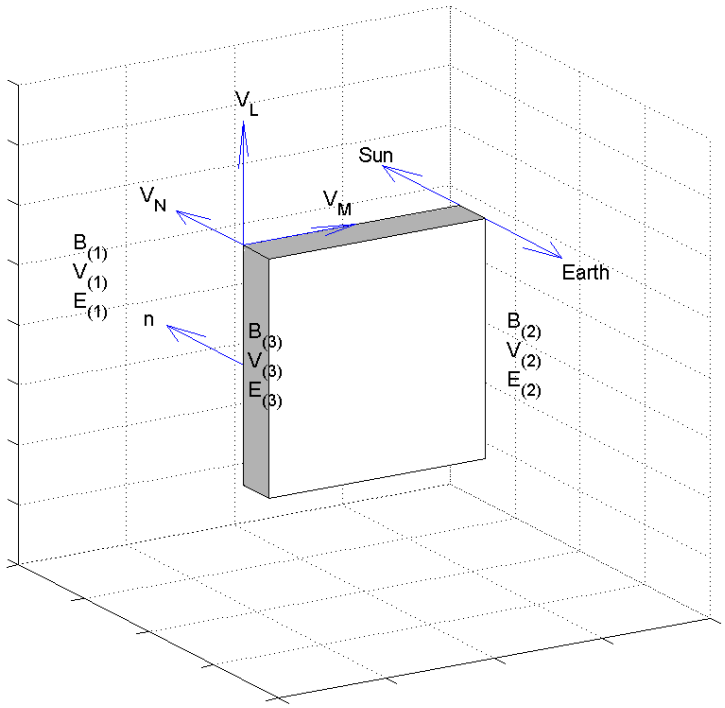

Figure 2.3: A simplified diagram depicting a section of the transition layer from the earthward side, with the quasi-static structure defined by the de Hoffmann Teller analysis (shaded section, B_3, V_3, E_3) between the sunward (B_1, V_1, E_1) and the earthward (B_2, V_2, E_2) layer boundaries (white planes).

as the electric field can be sampled at a higher frequency than the bulk flow velocity, and also any bias that may exist in the plasma instrument is not then introduced into the field quantities. The electric field measurements can, however, be incomplete which the requires the use of the second method.

Discovery of the parameters defining this frame, therefore, allows the removal of the influence of that convection which should lead to the underlying structure being highlighted rather than the velocity of that structure with respect to the satellite itself.

The velocity vector defining this frame is found by considering the mean square value of the electric field across the region of interest. This quantity is defined in equation 2.7 as D. The minimum value of this equation is therefore dependant on the vector difference of the bulk velocity (V_P), and this de Hoffman velocity (V_{HT})

(Bauer et al., 2001; Paschmann and Daly, 1998).

$$D = \langle |(V_P - V_{HT}) \times B|^2 \rangle \tag{2.7}$$

To achieve the minimization of this equation an iterative technique is used. Iterative and recursive techniques have been used in the past (Aggson et al., 1983), although seemingly not using genetic methods. Possible HT velocity vectors are iteratively generated by mutation from the vector evidencing lowest D in the previous generation. An example of this evolutionary process is presented in Figure 2.4.

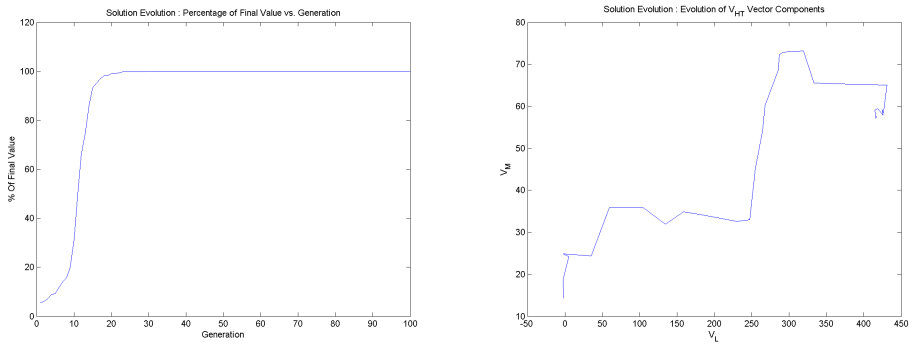

(a) shows the current value of the average convective electric field (D) each generation with respect to its final value. In this case D reached 99.9% of its final value in 38 iterations of the evolutionary algorithm, which with a D/D0 of $\approx 5\%$ describes a very well defined de Hoffmann Teller frame.

(b) illustrates the velocity phase space variation of the tangential components of the de Hoffmann Teller velocity vector. The initial position is in the bottom left hand of the diagram and the final position is in the top right.

Figure 2.4: Diagrammatic representations of the evolution of V_{HT} vectors.

Multiple attempts are made with different initial values to reduce the possibility of the solution only being a local minimum. To reinforce this initial condition is randomized with respect to the velocity phase space plane negating another possible source of bias. The appropriateness of the selected frame is tested by plotting, component by component, the derived convective electric field E_C against the de Hoffmann Teller frame transformation electric field ($E_{HT} = -V_{HT} \times B$) (Paschmann and Daly, 1998; Bauer et al., 2001).

A frame that is well defined should evidence a linear relation between E_C and

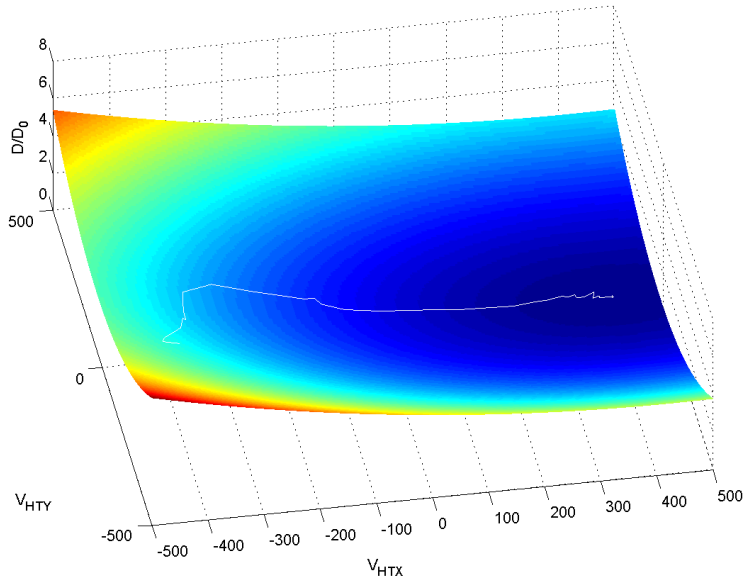

Figure 2.5: The evolutionary path of the dHT frame solution (white) with respect to a 2D (x,y) phase space plane. The z-axis shows the fitness of the solution D/D_0 and clearly indicates that, in this case, the solution found is a global, not a local, solution.

E_{HT}. Linear regression is therefore used to derive the fitness of this frame in terms of the gradient of the fit and the correlation coefficient of the data points to that fit.

Further evidence is described in terms of the comparison of the original value of D_0 as calculated from the raw data, where, in the above equation, $V_{HT} = (0, 0, 0)$ (i.e. with no dHT frame correction) and D_V as calculated using the determined V_{HT}.

If the value for the correlation coefficient is near unity and the ratio of D_V/D_0 is near zero then the frame is said to be well defined and useful, in this study, for determining a coherent reconnection layer structure.

A low correlation and D reduction coefficient suggest that any internal current or transition layer structure may either not be present or may be time-varying. Non-unity gradient values can occur and may have varying causal factors, an existing electric field will modify the linear regression parameters in terms of the offset, as long as that field is consitent across the layer, but not the gradient. Changes to the gradient can come about as an added effect, through system variability or possibly

instrumental noise, or as a factor inherent to the flow. This latter case describes a situation where there is a component of the bulk velocity tangential to the normal that is not described by the dHT velocity itself.

dHT analysis also provides a measure of the radial velocity of the magnetopause boundary in V_{HT}. For data that is in the boundary normal coordinate system then this values is given directly by V_N, other coordinate systems may require further analysis of the velocity with respect to the axes and origin. A low V_N suggests that the magnetopause is quasi-stationary. Not only does this suggest a more settled local environment, it also suggests preferable conditions for in-depth analysis as the spacecraft then transit the layer cleanly and with no effects due to relative boundary movement such as non-linear penetration paths or re-transiting the boundary as it moves over the spacecraft. Such conditions would, logically, only seem likely when the solar wind has evidenced no large scale variation over the time period shorter than that for magnetopause boundary reorientation or relocation.

2.3 Walèn (Tangential Stress Balance) Analysis

The Walèn or Tangential Stress Balance relation tests whether the plasma flow in a de Hoffmann-Teller convection frame, a rotational discontinuity or large amplitude Alfvén wave, is field-aligned and linearly related to the Alfvén speed. This has been suggested to be the case for reconnection events at the magnetopause (Paschmann and Daly, 1998; Bauer et al., 2001; Eriksson et al., 2004).

The Alfvén Velocity is given in equation 2.8 as:

$$v_A = \sqrt{\frac{B^2}{\mu_0 \rho_f}} \tag{2.8}$$

Which is then related to the plasma velocity in the dHT frame. If we allow for anisotropic pressures we get equation 2.9

$$V - V_{HT} = \pm \frac{B\sqrt{1-\alpha}}{\sqrt{\mu_0 \rho_f}} \tag{2.9}$$

Where B is the magnetic field, ρ_f is the ion species mass density and α is the pressure anisotropy, defined in equation 2.10 as:

$$\alpha = \frac{P_{\parallel} - P_{\perp}}{2P_B} = \frac{(P_{\parallel} - P_{\perp})\mu_0}{B^2} \tag{2.10}$$

Where $P_{\parallel}$ and $P_{\perp}$ are the parallel and perpendicular plasma pressures respectively and P_B is the magnetic field pressure (Bauer et al., 2001; Eriksson et al., 2004; Paschmann and Daly, 2008).

If isotropy is assumed then equation 2.9 reduces to a far simpler form.

A scatter plot is constructed in similar fashion to the previously described dHT analysis by plotting the components of V_A against $V - V_{HT}$; the components of the local Alfvén speed against the components of the local plasma bulk velocity in the dHT frame. A comparative example of this can be seen in Figure 2.6.

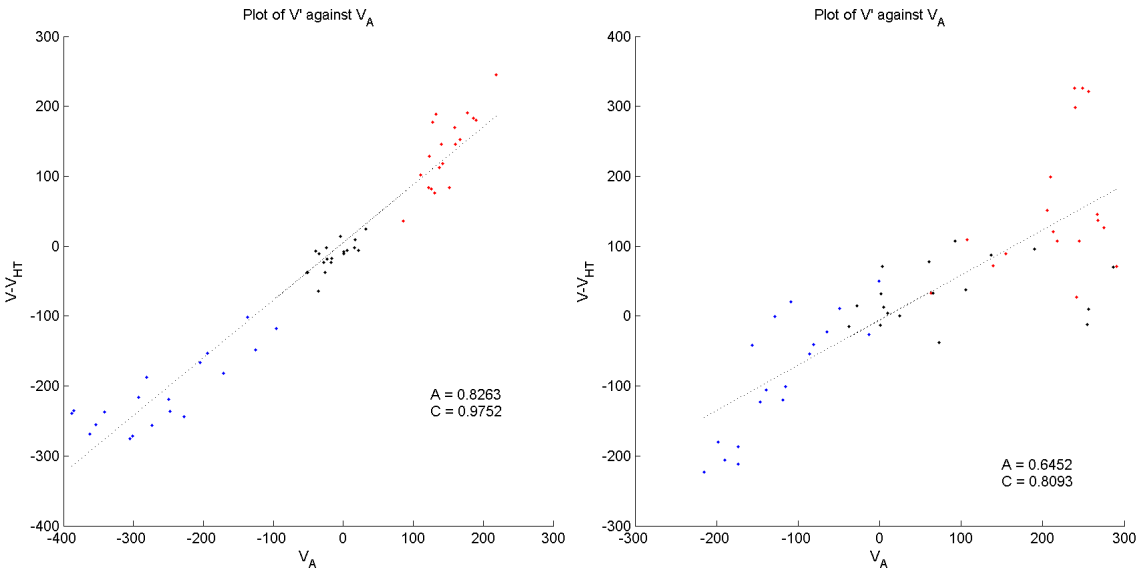

(a) (b)

Figure 2.6: Comparative results of applying the Walèn stress balance relation to two temporally adjacent transitions, one evidencing good agreement with the relation (frame a) and the other showing less coherence (frame b). Both were calculated from data recorded by Spacecraft 1 (Rumba) on April 1st 2003.

In the same way both the gradient and correlation coefficients for a linear regression line are produced. A low correlation coefficient is therefore indicative of the plasma in question not being driven by the reconnection source or if it was

that there have been other interactions than those allowed by the parameters of the Walèn analysis.

The correlation coefficient quantifies the appropriateness of the selected reference frame. A gradient magnitude of < 1.0 suggests entirely sub-alfvenic flow speeds. A value of ≈ 0.6, or $60\% V_A$ is considered (Øieroset et al., 2000; Eriksson et al., 2004) to suggest the presence of a slow mode shock connected to the diffusion region that would prevent acceleration of the plasma to super-alfvenic speeds. The sign of the gradient is indicative of whether the field aligned flow is parallel or anti-parallel to the field direction in the frame of the shock and so whether the spacecraft crossing is above or below the reconnection site based on the sign of B_N through the layer (Paschmann et al., 1979; Phan et al., 2004).

2.4 Particle Distribution Methods

The most common method associated with the analysis of particle distributions near the magnetopause is to examine them for evidence of acceleration and population selection (Cowley-D distributions) in the reflected ions from, and transmitted ions across, the magnetopause current layer (Paschmann and Daly, 1998; Bauer et al., 2001; Phan et al., 2004; Russell, 2003; Retinò et al., 2005; Zheng et al., 2005; Nykyri et al., 2006).

Regions exhibiting so called "open" magnetic field geometries ($B_N \neq 0$) such as reconnection layers might be indicated by the presence of trasmitted ion populations in addition to the source plasma population that would be expected in that location, such as magnetosheath ions on the magnetospheric side of the magnetopause or hot ring-current ions in the magnetosheath (Cowley, 1982).

A primary consideration is how, with respect to the convective plasma frame previously defined in §2.2, we may see distributions indicative of transmission and acceleration superimposed on the expected magnetopause/magnetosheath populations that have a cut-off at the de Hoffmann-Teller velocity. This is due to the fact that any material moving at slower than the convective frame speed will be lost

from the distribution.

This method has been, during this study, used as a confirmator of behaviour rather than an exploratory tool in its own right.

2.5 Constructing the Model

In the original publication (Heyn et al., 1988b), later refined by Biernat et al. (Biernat et al., 1989) and again by Rijnbeek and Semenov (Rijnbeek and Semenov, 1993), a method is presented to describe a reconnection layer in terms of the ideal MHD wave modes that may physically comprise it. The model is simplified to assist construction by being planar in nature and using single fluid ideal MHD and requires the conservation of total pressure (magnetic and plasma) across the simulation region. As such the limitations these simplications place upon the nature of the solution must be considered at each stage of any analysis using it. However, even considering such simplifications, the model can assist with the task of describing the nature of reconnection at many sites within the magnetosphere because it can provide a structure of up to 5 coupled wave modes, within which is described the nature and strength of particular wave modes that make up a particular layer. This possible structure can be used as a basis to establish parameters for a more in-depth analysis, that may not be subject to the limitations imposed by the use of ideal MHD. The model can also be applied quickly and simply to multiple crossings or events and may assist in building up statistical categorisation of the nature, location or timing of such reconnection events.

2.5.1 Model Structure

The model is constructed using a set of non-linear conservation relations derived from the general form of the Rankine Hugoniot shock-jump conditions for discontinuities in a plasma. These relations are arrived at through the application of behaviour specific criteria based on the characteristics of the wave modes we wish to describe:

Alfvén wave, Slow mode and Entropy wave (as a contact discontinuity). The first simplification is that of assuming the validity of ideal magnetohydronamics. The plasma itself is assumed to be a single ionic fluid. Plasma composition enters the system through a mass factor that is the average ionic mass in atomic mass units. A plasma completely comprised of H^+ would have a mass factor of 1.00, 98% H^+ and 2% He^+ would have a mass factor of 1.06 and so on.

The model also assumes a conservation of total pressure on either side of the layer. This assumption is entirely valid for the magnetopause boundary when it is near stationary, since this suggests that the total pressure on each side is equal, as the de Hoffman Teller derived V_N increases, meaning that there is a significant pressure imbalance across the layer driving its movement, this is less well observed. It may be possible to quantify this by plotting the final fitness of any one model against the calculated de Hoffmann Teller frame V_N.

As a direct reflection of the Petschek-type geometry which is defined to apply outside the diffusion region, where the frozen-in-flow condition and thus, where MHD breaks down, the reconnection layer is comprised of a collection of the aforementioned MHD wave mode types. It is assumed that the reconnection layer is planar (2-D) and that the layered MHD wave modes are modelled as planar discontinuities with large enough separation between modes that no mixing of modes takes place. The model is constructed using a maximum of 5 MHD wave mode layers of 4 different types. Each of the layers is included to carry out a different mechanical function upon the inflowing plasma.

The layer is bounded on either each side by an intermediate magnetosonic (Alfvén) wave to bring about the necessary rotation of the magnetic field direction.

Slow mode waves are included to convert the energy stored in the magnetic field geometry into an impulse acceleration in bulk velocity and a corresponding thermalisation of the plasma.

The contact discontinuity in the centre of the layer divides the two plasma pop-

ulations. There is no exchange of material across this boundary. A central discontinuity (entropy wave) is used to achieve the changes in [n] and [T]

Fast mode MHD waves are excluded from the model by the assumption of a conserved total pressure across the layer. The lack of significant pressure gradients deprives the fast mode waves of a driving mechanism and leads to their negligibility within the layer as they may be considered a perturbation. It is important to remember that this assumption only precludes fast mode waves inside the model layer, they may still occur outside the model layer where this assumption is not applied, or if a driving mechanism is present.

2.5.2 Model Behaviour

The model uses two factors to decide the internal structure of the reconnection layer it is being applied to. Both of these factors are calculated using the input boundary conditions. The first behavioural variable is the previously mentioned η factor. In terms of observed variables it can now be defined as in equation 2.11 below, where the u and d subscripts specify the magnetic field strength upstream and downstream of the slow mode structure in question:

$$\eta = \frac{B_u}{B_d} \tag{2.11}$$

As a selection factor η describes the status of the slow mode waves within the layer. If $\eta < 1$ that means there is a decrease in the magnetic field strength over the discontinuity, energy stored in the magnetic field geometry has been transferred to the plasma. On this basis the model uses a slow shock at that discontinuity position, whereas if $\eta > 1$ then the model is constructed using a slow expansion fan. The second selection factor is the magnitude of the magnetic field coplanarity vector ($|\mathbf{b}|$) required for aligning the slow mode waves within the layer.

The precise structure of the layer is not therefore, arbitrary, but arrived at mathematically from a re-arranged form of an equation for the conservation of energy to produce the aforementioned structural variable values. These are then compared to

an internal table of values defining the theoretical mathematical requirements for each wave type, (Heyn et al., 1988b). $|\mathbf{b}|$ is defined as follows in equations 2.12 - 2.14:

$$\boldsymbol{b_L} = \pm[v_{L0}^{'} - v_{L0} \pm (V_{AL0}^{'} + V_{AL0})] \tag{2.12}$$

$$\boldsymbol{b_M} = \pm[v_{M0}^{'} - v_{M0} \pm (V_{AM0}^{'} + V_{AM0})] \tag{2.13}$$

$$|\boldsymbol{b}| = \sqrt{\boldsymbol{b_L}^2 + \boldsymbol{b_M}^2} \tag{2.14}$$

The magnitude of this vector is used to decide the choice of layers within the model. The structural types and their numerical criteria are presented in Table 2.1.

Condition	Structure Type
$\|\mathbf{b}\| = 0$	ACA
$0 < \|\mathbf{b}\| < V_{At0} + \tilde{V}_{At0} G \frac{B_{t0}}{\tilde{B}_{t0}}$	ASCSA/ACSA
$V_{At0} + \tilde{V}_{At0} G \frac{B_{t0}}{\tilde{B}_{t0}} < \|\mathbf{b}\| < V_{At0} G \frac{\tilde{B}_{t0}}{B_{t0}} + \tilde{V}_{At0}$	ARCSA or ARCA
$V_{At0} G \frac{\tilde{B}_{t0}}{B_{t0}} + \tilde{V}_{At0} < \|\mathbf{b}\| < V_{At0} G(\sqrt{\beta + 1}) + \tilde{V}_{At0} G(\sqrt{\tilde{\beta} + 1})$	ARCRA

Table 2.1: The numerical regions defining reconnection layer structure in terms of $|\mathbf{b}|$.

From these values MHD wave modes are selected to form the reconnection layer from between 3 and 5 discontinuity sub-layers. The arrangement of which is defined by the previous parameters but allows for anything from an ACA structure in the slow-mode switch-off limit to complete ASCSA structures, in which either of the slow mode shocks can be replaced by slow expansion fans or removed entirely) or collapsing of weak wave modes should they prove to have no visible effect on variable behaviour.

In diagram 2.7, U is an 8-dimensional matrix variable compiled of the variables in brackets. U_0 and $\bar{U_0}$ are, therefore, the initial boundary states that are calculated from the observational data and are input into the model. Subscript 1 denotes the values after the action of the Alfvén wave (A) on either side, and 2 signifies that values on either side of the central contact discontinuity (C) after the changes

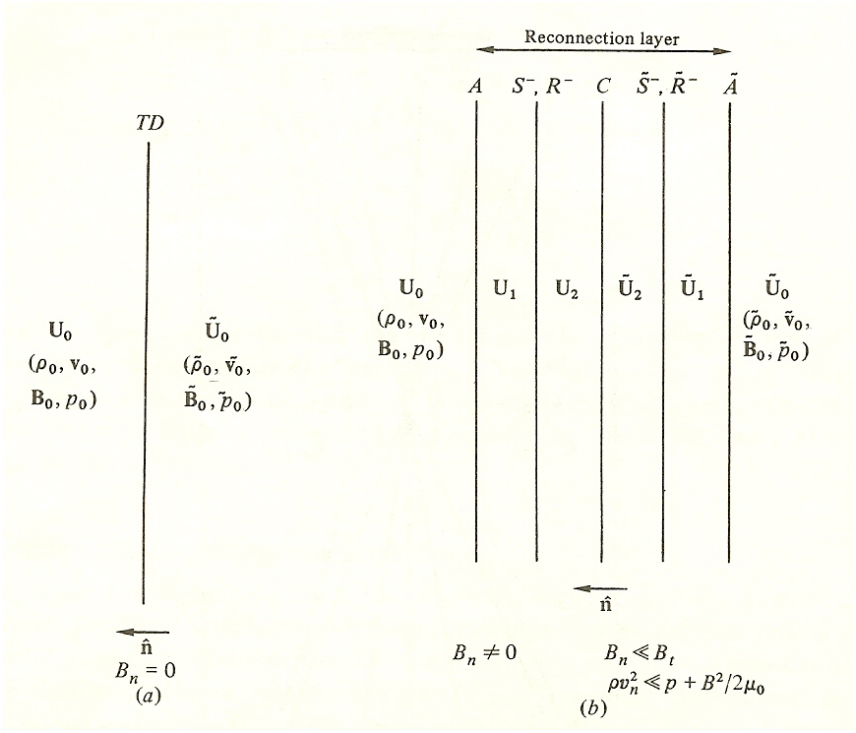

Figure 2.7: Diagram (from Heyn 1988) showing the initial Tangential Discontinuity described by the model and the reconnection layer it becomes. Subscripted variables indicated those steady states reached before and after the action of each type of wave mode shown.

brought about by the Slow Expansion Fan (R) or Slow Shock (S). The specific equations used in the simulation of these layers are presented in full in Appendix A.

The modelling process is defined, in this context, as producing predicted values for the variables describing magnetic field strength and direction, bulk velocity magnitude and direction, temperature, magnetic and plasma pressures, plasma beta and number density across each MHD wave mode.

The construction process runs thusly:

1. The variables are converted into dimensionless values
2. $|\mathbf{b}|$ is calculated from the bulk velocity and Alfvén velocity on either side of the layer.
3. η is derived.
4. The precise structure of the layer is decided upon and specified.

5. the equations are firstly applied to conditions on both outer edges of the layer and the behaviour of the variables is worked towards the central discontinuity.

6. The results for the different layers are compiled into a single model for the variables across the layer.

7. The layer model is output.

2.6 Past Use Of This Model

This model has been applied to data in the past. Both the ISEE and AMPTE/IRM missions saw previous use of this model.

In the initial paper outlining the model (Heyn et al., 1988b) they used the Rankine-Hugoniot jump conditions for non-linear ideal MHD to construct a model for a reconnection convection region layer based on Riemann boundary value analysis using inflow conditions from observational data. The model was discussed in terms of the input parameters and their effects on the solution behaviour and structure. The derivation of normal field and flow parameters were also touched on briefly as well as the angular or spatial extent of the reconnection layer itself. Later a paper (Heyn et al., 1988a) used the construction in the original paper and considers energy flows through the model as defined there. This flow now allows for anisotropies between the two input regions. Using the wedge shaped setup for the discontinuities, it enumerates the energy flows between each of the discontinuity pairs in terms of the inflowing component, and two outflowing components, one directed into the next discontinuity and the other exiting the system as a reconnection jet aligned with the magnetopause boundary. It should be remembered that due to the addition of the contact discontinuity there is effectively no transmission of plasma across the layer itself. This is not the case realistically as density gradient driven plasma penetration and the non-zero normal component of the magnetic field in a realistic field geometry ensure some transmission that will then influence behaviour. Comparisons are made between the predictions of this behaviour and an event recorded by the

ISEE1 satellite on the 8th of September 1978. The results in this case highlighted the Alfvén wave as a conversion sink for electromagnetic energy into kinetic energy, especially on the magnetosheath side, in addition to the highlighted shortcomings imposed by not allowing coupling between wave modes in this model. This same event was used as the basis of another paper (Rijnbeek et al., 1989), in which it was explored extensively in terms of the model. Shortcomings were highlighted in terms of heavy ion populations, variations in pressure and normal field and flow components, the assumed uniformity of the inflow regions and the features not modelled by the single fluid MHD approach. These considered in context, however, the model does continue to prove itself as a useful analysis tool for interpreting data in addition to exploring the behaviour of the reconnection process itself (Rijnbeek, 1992; Biernat et al., 1989). Further theoretical work was continued on this model until the introduction of a fundamental change in 1992 (Semenov et al., 1992a) from a steady-state solution to a time-dependant one with a consequent summary paper describing the behaviour of this new construct (Rijnbeek and Semenov, 1993). Later extensions to the model have come in the form of three-dimensionality (Biernat et al., 1998) and even an accounting for relativistic effects (Tolstykh et al., 2007).

However, the model was always applied according to arbitrary specifications and so to a very few events. So since inheriting the basic model from R. Rijnbeek there have been significant alterations within the model in addition to the larger ones external to it. This study has also set out to analyse a larger number of events with fewer recourses to abitrary conditions. The latter has been achieved by the application, through genetic algorithms, of calculated boundary conditions. Using a purely mathematical basis for construction of the model is likely to lead to results that are more robust and less susceptible to variance or bias due human decision making processes. The original use of the model was also carried out without direct calculation of the degree of accuracy or fitness for comparison between models of the same type from different events or cases. The model, as applied, also lacked the internal ability to modify the structure of the layer itself, to either compress

or remove degenerate modes from the result. Heavy ion factors were also, in some cases, calculated from implied values based on average proportions in particular plasma populations. The ability to now use CIS-CODIF data means a far more direct approach can be taken during the calculations. These factors, along with the easy applicability of the model and its high information return to input resource ratio made it the perfect basis for testing extensions based on this method.

2.7 Applying the Model & the Genetic Algorithms

The structure of the reconnection layer as described by the model is based on the observed variable parameters on either side of the layer input into the model as initial boundary conditions. The selection of these conditions introduces a degree of dependence of the resultant model on the criterion applied to that choice of conditions. For example, using data from the 17th of February 2004, the variable sets in the pre-layer region were sampled over the course of one minute. The tangential magnetic field components in this case were $(B_L, B_M) = (-0.03, -16.14)$nT, a one second translation in beginning and end point of this interval, within a relatively settled period of activity, now gives $(B_L, B_M) = (-0.07, -16.14)$nT. While this may not mean a fundamental shift in behaviour it does provide the possibility that the best sampling interval may not be the one first selected.

One reason that the tools of evolutionary programming have been introduced, is to attempt to decrease the effect of this dependence and to give results in terms of a modelled reconnection layer that is more robust against these minor changes and is not subject to the arbitrary factors imposed, inherently, by visual selection. By using a purely numerical basis for application of a model, it is possible to apply multiple models to a single event and compare the results. The method itself is not model specific and so may prove useful in the evaluation of different analytical models for particular cases or types of events.

Application of the tools was achieved with a linked pair of algorithms; the first algorithm modified the sampling range for the boundary values, the second worked

structurally by changing the spacing of the modelled discontinuities within the layer itself.

The nature of the program is such that it starts with an initial value set, from this initial set a certain number genes are created by mutation of the parameters contained within that set to produce offspring sets. The mathematical fitness of each of the offspring sets produced is calculated based on a system derived from the equations that make up the model and constructed empirically.

Fitness systems that have been tried include:

1. An absolute difference method that computes the sum difference of each variable across each layer in the natural units of the variable in question. Obvious issues arose early during testing using this method as variables with higher comparative value, for example bulk velocity $\approx 100s$ or km/s vs. number density $\approx 10 particles/cm^3$, tended to drive the evolutionary optimization leading to, effectively, a single variable result.

2. A percentage difference method that works out the difference as a function of the total value per unit time. This approach has the advantage of being unitless and therefore comparable between variables. The only inherent bias is in those variables that are naturally subject to greater variance, or a higher rate of sampling.

3. A weighted variable fitness system with each downstream region being compared with the model with only those variables that change according to the jump conditions included and each of those weighted by the power of that variable in the equations.

The numerical basis for a mode's fitness is based on a percentage difference per unit length of time.

The one with the greatest fitness is selected and set as the new parent gene. The process is then continuously repeated.

This study has used a combination of systems 2 and 3, in that the values combined are those provided as the unitless percentage difference per unit time but the way they are combined is by using a weighted fitness system based on the equations of the model jump conditions. In each case the physical observables used to calculate the fitness of the model can be specified beforehand. The decision was made to make primary use of non-derived quantities such as the magnetic field magnitude, bulk velocity, number density and temperature as these may be less susceptible to methodological inaccuracy due to simplifying assumptions that may be present in derived quantity calculations, through the use of ideal MHD for example.

The repetition process ceases once a stable fitness point has been reached. The resultant values comprising the "fittest" gene are then returned. The entire process is repeated several times, as before, for each spacecraft and for each crossing to ensure that located minima are global.

2.7.1 Boundary Value Sampling Range (BVSR)

The BVSR algorithm works by modifying the four parameters associated with the selection of boundary values, these are the beginning and end points of the pre-layer sampling period and the same for the post-layer sampling period. These values, at this time, are stored as index values of the data array for the magnetic field. Future versions may, instead, hold these values in terms of the a time index in seconds, removing any dependence on the data file used rather than on the data itself.

These four index values form the "gene" in this algorithm and are specified in the initial execution stage. From this initial gene set a number of "offspring" are generated using randomised mutation within preset limits. These limits may be specified directly in the initialisation stage of the simulation, or through the use of the RLDS algorithm described in §2.7.2. It is important to note that the limits are imposed, primarily, to prevent the algorithm from selecting parts of the transition layer itself as candidates for the boundary conditions of that layer. A demonstration of the variability present in this method, as presented in Table 2.2,

has been constructed from the first generation of mutated "genes" produced by the algorithm.

Variable	Value (units)	σ	Range	
B	17.53 (nT)	2.92	14.63	23.25
V (CODIF)	179.37 (km/s)	4.74	171.10	185.59
N (CODIF)	7.40 (N/cm^3)	0.18	7.22	7.71
T (CODIF)	2.61 (10^6K)	0.08	2.48	2.69

Table 2.2: A selection of pre-layer variable values, standard deviations and ranges to illustrate the variance in initial values using the BVSR modification approach. In this case spacecraft 4 model data is used from the 20th February 2002 at 14:00UT.

Each gene in turn is them used to construct a set of boundary values over the range it describes. These values, once calculated, are entered into the simulation routine to produce a candidate reconnection layer that exhibits minor variations in comparison to the progenitor set. The fitness of these layers are then enumerated and the fittest one is chosen, the process then repeats until a stable point is reached. The relation between the initial model and that selected as being the fittest is highlighted in Figure 2.8, it can be seen that in every variable the final model is a significantly better fit for the data than the original. This is the goal of this method.

2.7.2 Reconnection Layer Discontinuity Spacing (RLDS)

The RLDS algorithm is somewhat more complex in both function and application than BVSR. In this case the evolutionary programming controls the parameters associated with the points in the current data time-series where the spacecraft interacts with each of the discontinuities that comprise the theoretical reconnection layer.

Although it is possible to have calculated the 5-variable value in"fitness space" of every possible configuration, given the range, accuracy and number of variable this was felt to be less effective than an evolutionary approach. The approach is even more efficient if an initial structure is inputted into the algorithm to be used as a template.

The selection of the initial discontinuity positions is an important part of the

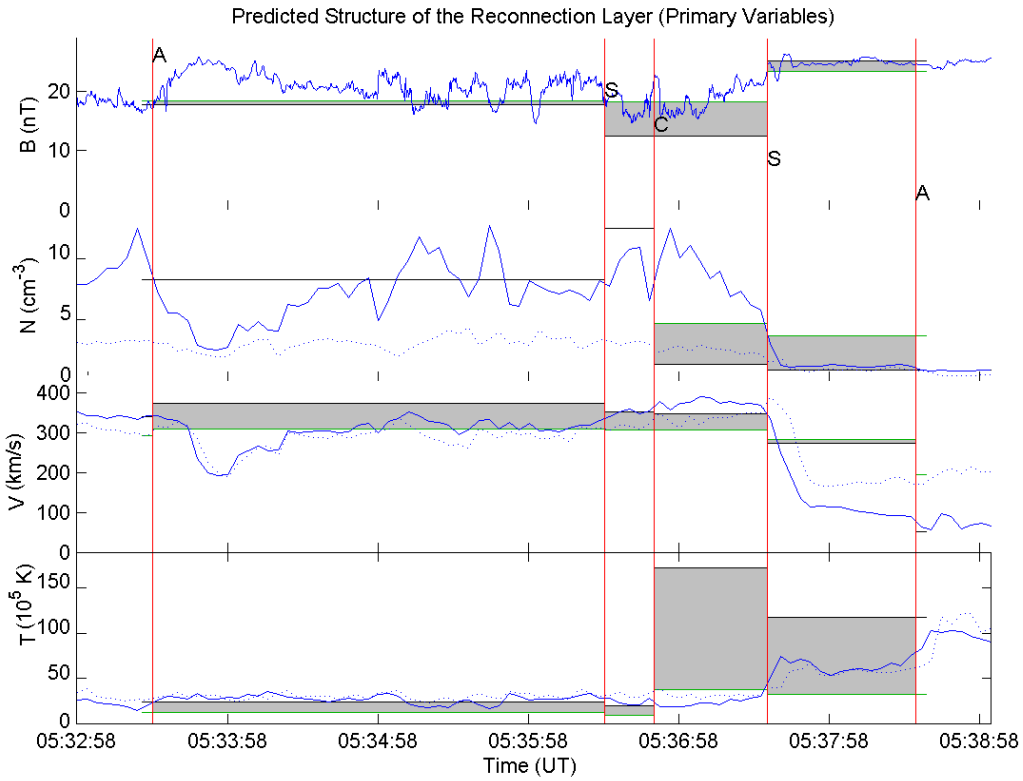

Figure 2.8: Overlaid comparison of the models created using initial sampling ranges (black) and those produced by the BVSR method (green). The change between the two is highlighted by the grey filled area between the two lines. This event occurred on the 3rd July 2001 and was observed by spacecraft 3 FGM and CIS-HIA instruments.

process. This is because repetitive selection of the same, or very similar, initial conditions may lead to localization of final solutions. If the algorithm is being used to fine-tune a pre-decided structure then this is not only a positive aspect but the very point of using the algorithm in the first place. If, however, the algorithm is being used to describe a structure that may exist within the data but has not already been outlined then this can be conducive to gaining bad solutions. In the latter case several methods have had to be applied during the study to calculate the initial states. These have been:

1. A conventional spread system.

   All discontinuity time indexes are assigned randomly with a check to make sure that all are in the order defined by the model.

2. A sector designated randomisation system.

   The transition interval is divided into 5 sectors, matching the 5 discontinuity components to be compiled, and within each sector the initial position of the discontinuity is selected randomly.

3. A consecutively assigned and randomized sector system.

   The first discontinuity time is set randomly across a possible range of the entire interval. Proceeding from this initial condition the allowed interval range is then shortened from this first position to the end of the initially specified interval. This process continues through indexes 3-5 until the entire layer has been assigned within the increasingly smaller period.

Method 1 is simple and easy to apply quickly to a particular transition. One drawback to this approach is that the initial system is constructed as a single entity, as such the range of positions available is somewhat compromised. Method two is an improvement on the first method as the variable range is specified by the interval itself rather than externally, yet it still holds the possibility of exhibiting localised solutions. Method 3 takes the best of both situations by allowing the entirety of the initial interval as a starting point for the layer, and so attenuating the probability of localised solutions, while still remaining simple enough to not present a significant computational resource sink. The results, for a single discontinuity, of one of these repeated series are presented in Figure 2.9.

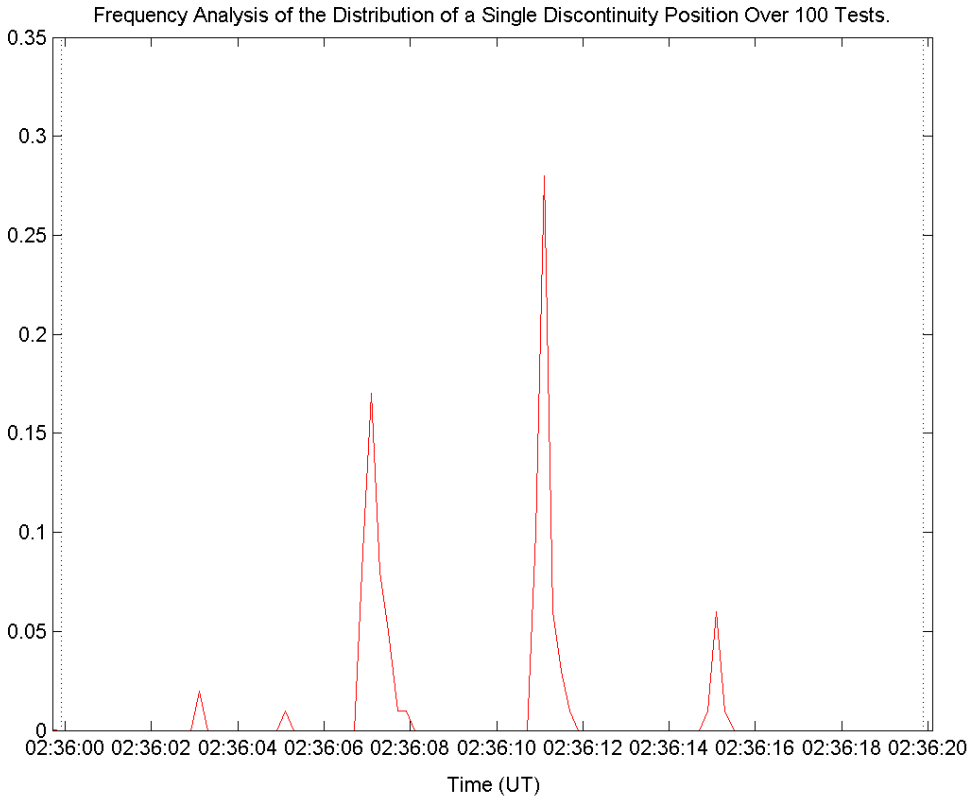

Figure 2.9: The frequency distribution, in time, of solutions for the location of a single MHD discontinuity in the model after 100 tests.

Chapter 3

Presentation of Case Studies

3.1 Case Study Parameters

The presentation of the case studies examined will be hierarchically by physical structural type. Absolute time, in this case, is effectively a secondary event label. Considering this it has been decided that case studies should be presented grouped and in order of increasing structural complexity of the simulated MHD wave modes.

3.1.1 Case Study Selection

Case studies for this investigation have been selected from events already published. The only selection criterion was that the event should be located in the dayside magnetopause and should have been described in terms of the presence of reconnection established by either fluid (dHT or Walèn) or particle (velocity phase space distribution) evidence.

The basis for the selection was not to question whether an event showed the existence of precise MHD or kinetic reconnection layer structure but how well the observed data signatures could be modelled and explained by this approach.

This approach was decided upon so as to provide an unbiased basis for further study of these events and possible identification of these events from a larger body of data in an automated or semi-automated fashion.

3.1.2 Case Study Presentation

Each case will consist of 3 subsections:

1. The pre-simulation analysis section will describe the overview of the event in terms of event location, satellite geometry and general behaviour.

2. The non-simulation events subsection will relate information gained through boundary normal analysis, de Hoffmann-Teller analysis, the Walèn stress balance relation test and distribution function, phase space or other kinetic analyses that relates to any interactions that impinge or highlight aspects of the case without being subject, specifically, to analysis with the Petschek-type reconnection layer model.

3. Simulative analysis will then deal directly with the application of the model to observational data, the construction of the first-pass reconnection layer model through simulation and the features of that model. The analysis through the use of genetic algorithms to derive a self-consistent non-arbitrary solution and then describe the resultant factors defining that model's health will be presented in Chapter 4 (Analysis using Genetic Algorithms). A discussion of all models produced for this event will follow and a collation of data into comparative format for reference in Chapter 5 (Summary of Cases) and with other cases in this chapter.

3.2 STRUCTURE TYPE II : (ASCSA), 1st April 2003

The original account of this event analysis was carried out by Zheng et al. in 2005 when they described evidence for observing accelerated flows in both the pre and post cusp regions that were associated with the reconnection process using evidence gained from both fluid and particle methods.

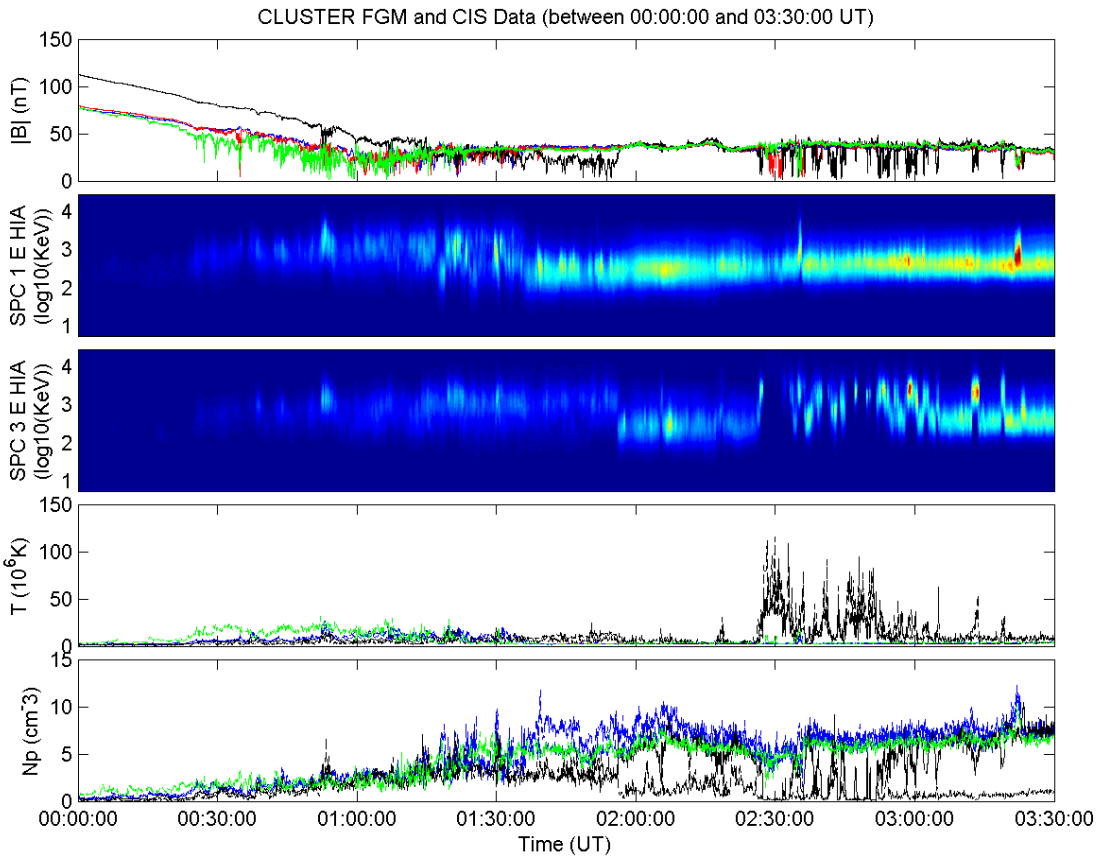

Figure 3.1: An event overview for the period between 00:00 and 03:30 UT on 1st April 2003 compiled using data from the active FGM and CIS instruments on all CLUSTER spacecraft. Omni-polar, omni-azimuthal energy spectrograms are provided using CIS-HIA data from spacecrafts 1 and 3.

The specified period of interest, from 00:00-03:30 UT on 1st April 2003 (Zheng et al., 2005), contains multiple transports across the magnetopause boundary. Significant differences are to be expected between this case and that dealt with in §3.3 due to the different spatial location, with respect to the GSE coordinate system.

In this case, the transits take place near the northern cusp with the CLUSTER group traversing the $GSE_Y = 0$ line during the period in question on an outbound trajectory. The positions of the spacecraft during this period have been plotted on a model magnetopause constructed using the Sibeck 1991 model (Sibeck et al., 1991) in Figure 3.2.

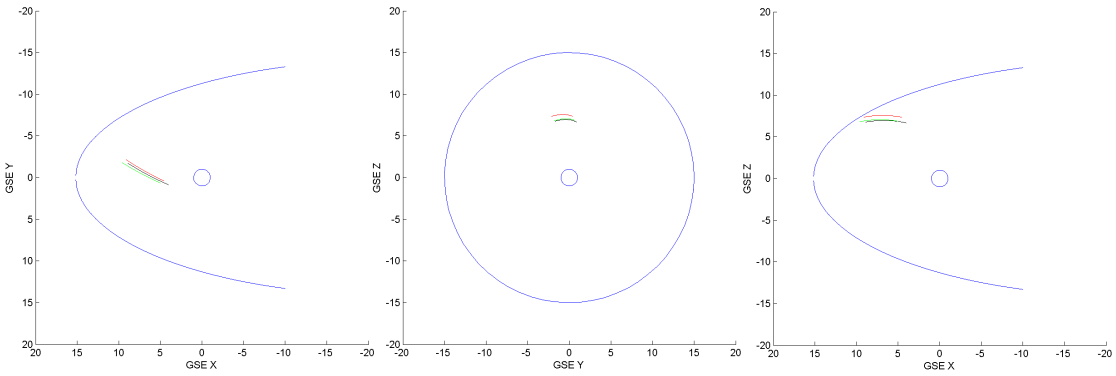

Figure 3.2: The spatial location and movement of the cluster spacecraft during the period stretching from 00:00 to 03:30 UT on the 1^{st} April 2003.

3.2.1 Pre-Simulation Analysis

The data presented in Figure 3.1 shows evidence of multiple magnetopause crossings during the time period that it covers. CLUSTER spacecraft 1, 2 and 4, show highly similar behaviour during this period in terms of the timing of various crossings, even if there is variation in the data recorded during them. The strong crossing feature seen, for these spacecraft, at 01:30 UT is subject to a temporal displacement, for spacecraft 3, of ≈30 minutes and is visible in the data at 02:00 UT. Because of this, the CLUSTER spacecraft observations during this period will be considered in terms of two groups. The explanation for this displacement in observational activity that was presented in the original paper, is the transition from the tailward cusp boundary, through the open cusp region and into the sunward magnetosphere. Zheng et al. (2005) drew this conclusion using the T96 model (Tsyganeko, 1996) to define magnetic location. The position data from the satellites at this time suggests this to be a reasonable explanation. Confirmation of this, however, is beyond the remit of this study at this time.

Before the transition feature at 01:30 UT there is evidence of multiple crossings undertaken by each of the spacecraft, these are located on the basis of significant changes in magnetic field direction and magnitude coupled with changes in temperature, number density and bulk velocity data. Each of these crossings, if apparently complete, were subject to boundary normal analysis, de Hoffman-Teller frame analysis, Tangential Stress Balance relation (Walèn) tests were carried out and the spatial

and phase space particle distributions were examined.

3.2.2 Non-simulation events.

To provide clarity and highlight similarities in the data recorded, by each satellite, during interactions with the magnetopause, the collated observations from all spacecraft for a particular time will be presented together, instead of the analyses for each spacecraft in turn being presented separately. The complete magnetopause transitions that have been studied occurred; at 01:17 UT, 01:19 UT, and 01:35 UT for spacecraft 1; 01:56 UT for spacecraft 3, which corresponds to the transition at 01:35 UT for spacecraft 1; and 01:16 UT and 01:19 UT for spacecraft 4, there is a later crossing for this spacecraft but it is incomplete.

Pre-simulation analysis therefore consists of the comparison of the transition data for spacecrafts 1 and 4 at 01:17 UT and 01:19 UT, and between spacecraft 1, at 01:35 UT, and spacecraft 3, at 01:56 UT.

At 01:17 UT the spacecrafts 1 and 4 passed, for a short interval, out of the magnetopause into the magnetosheath. The changes in number density (N), temperature (T), and bulk velocity ($\mathbf{V}$) all suggest a comparatively short transition period with easily recognisable changes in each variable. Clear, if low shear, signatures in the magnetic field mark the borders of the transition. The transition may be regarded as low shear as the rotation of magnetic field vector is only 60°. The state variable behaviour overview for this, and the following, transition can be seen in Figure 3.3.

The perturbations are more clear and of a smaller temporal extent in the data recorded by spacecraft 1, suggesting that each of the spacecraft passed through the transition layer at a differing angle or through different conditions. Local surface waves might present a possible explanation for the nature of these fluctuations

Boundary normal analysis on the first of these crossings resulted in the vectors in Table 3.1, with angular values $(\theta, \phi) = (-8.6°, -10.3°)$ and $(\theta, \phi) = (-23.6°, 40.2°)$ for spacecrafts 1 & 4 respectively. The significantly lower values for θ and ϕ for spacecraft 1 provide evidence for the more perpendicular approach explanation.

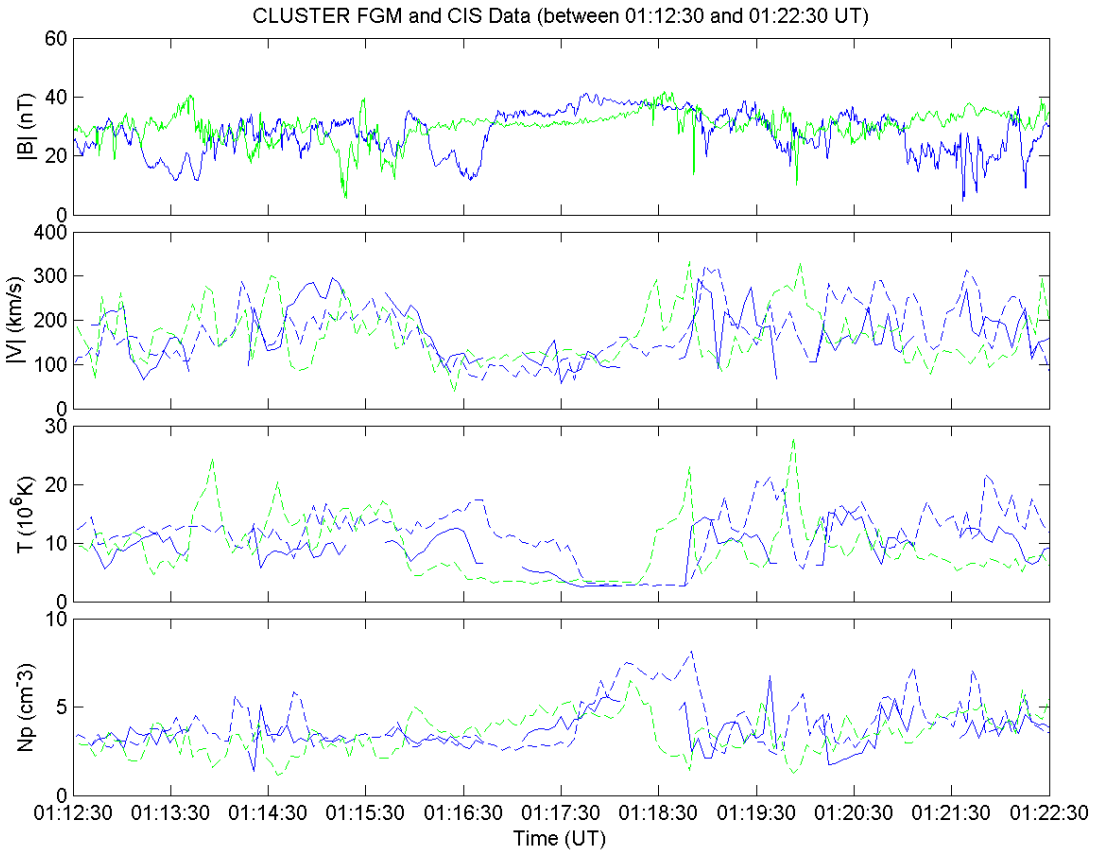

Figure 3.3: Plasma parameter overview for spacecrafts 1 (blue), and 4 (green) during the transitions that occurred at approximately 01:17 UT and 01:19 UT. The solid line shows CIS-HIA data, the dashed line is that from CIS-CODIF.

SPC	N_X	N_Y	N_Z
1	0.9729 ± 0.0008	-0.1466 ± 0.0054	-0.1786 ± 0.0050
4	0.7001 ± 0.0298	-0.3058 ± 0.0065	0.6453 ± 0.0323

Table 3.1: Normal vectors calculated for the transitions of spacecrafts 1 & 4 during the first crossing at 01:17UT

Once translated into the frame of the boundary the perturbations become clearer. The bulk velocity profile of the transition in Figure 3.4 highlights this. There are strong features suggesting both the rotation and acceleration of bulk plasma flow at 01:14-01:15 UT and a significant rotation, but not acceleration, of perpendicular flow as it completes the transition at 01:17:30 UT.

The extent of these velocity features was subjected to de-Hoffmann Teller analysis in an attempt to derive a frame, preferably common, that defines a quasi-static structure internal to the transition layer that would lend evidence to the existence of reconnection at this time in this location (see Table 3.2 for the results).

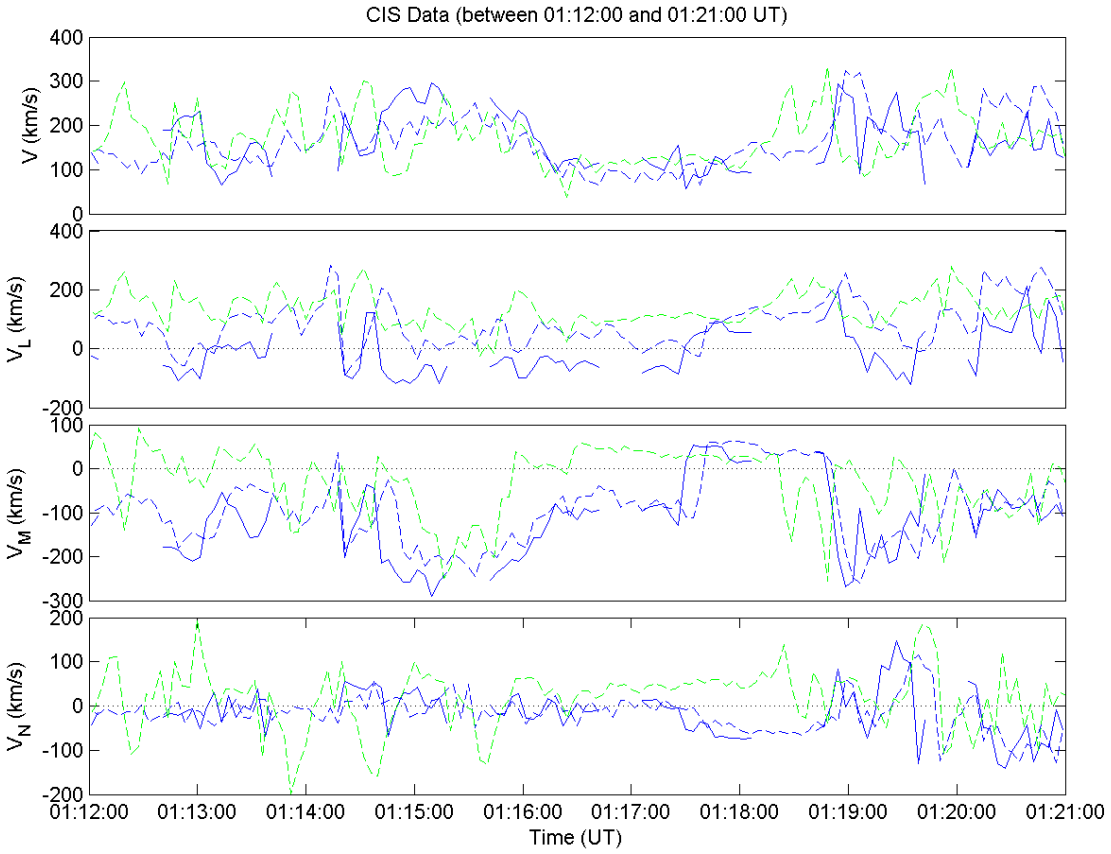

Figure 3.4: LMN-component bulk velocity data for spacecrafts 1 (blue) and 4(green). It can be seen that spacecraft 4 completes the velocity changes earlier, corresponding to the changes in the other ion and magnetic field observations.

Spacecraft	V_{HTL}	V_{HTM}	V_{HTN}	A	C	D/D0
1	212.67	-180.88	-41.87	1.02	0.92	0.12
4	156.06	-164.06	43.86	0.88	0.93	0.13

Table 3.2: Results of dHT analyses over the boundary transitions at 01:17 UT for spacecrafts 1 & 4.

de-Hoffmann Teller (dHT) frames are not inherently intercomparable. Not least, in this case, because the tangential components of the normal vector are nearly orthogonal to each other. The frame quality factors for spacecraft 1 describe a well defined frame with the gradient almost exactly unity and the correlation coefficient in excess of 0.92. The reduction factor (1-D/D0) is only 88% however this is an acceptable value in terms of the confirmation of fluid signatures. In the second case the gradient is non-unity which may, for example, suggest an incorrect sampling range within which lies observations of plasma populations that are not directly related to the convecting structure providing the frame that dHT analysis is attempting to describe. The correlation coefficient and reduction factor, however, are certainly indicative of the presence of a quasi-static structure during this transition being greater than 0.93 and 87%. The correlation plots for these two spacecraft are presented in Figure 3.5.

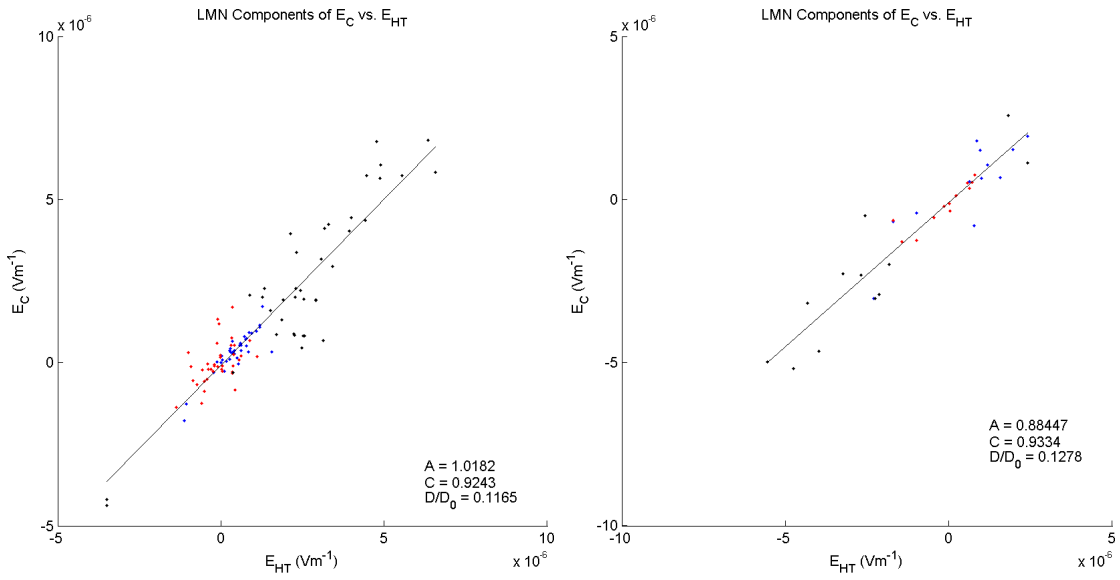

(a) Spacecraft 1.

(b) Spacecraft 4.

Figure 3.5: de Hoffmann-Teller analysis linear regression results for spacecraft 1 & 4 during the transition at ≈01:17:30 UT

Walèn stress balance analysis was carried out on these two features over the same limits used in the dHT testing, between 01:15:30 and 01:18:00 UT, and 01:15:45 and 01:16:30 UT respectively. The results in both cases were fairly conclusive. Both

tests evidenced a correlation constant of better than 0.90 with values of 0.94 and 0.98 respectively, and had similar linear regression gradients of 0.66 and 0.78, the graphs for these intervals are displayed in Figure 3.6. In these case, both suggest the presence of connection to a reconnection site.

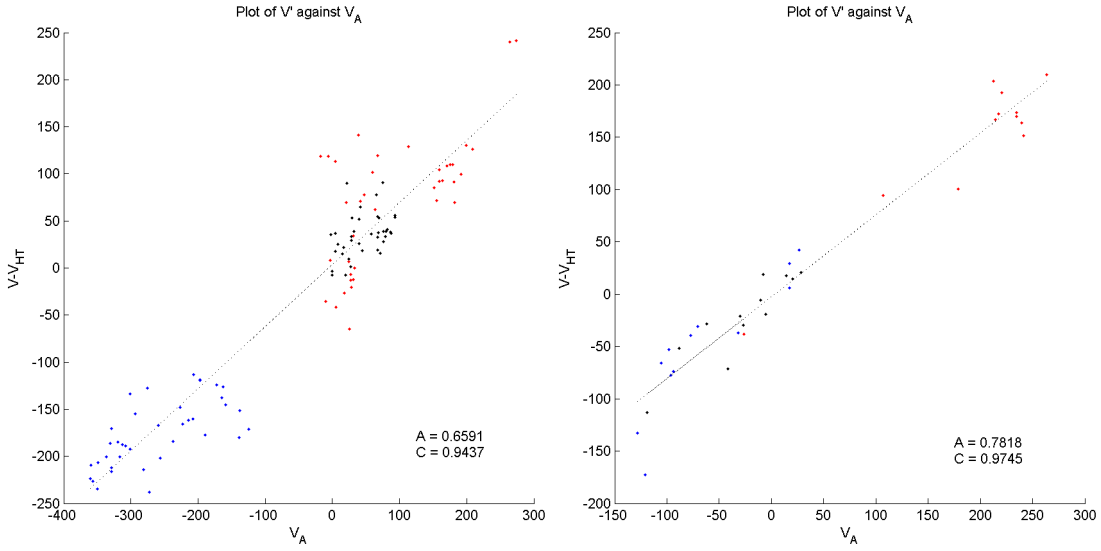

(a) Spacecraft 1 (b) Spacecraft 4

Figure 3.6: Results of the Walèn relation, tangential stress balance, test for spacecrafts 1 & 4, showing a component-wise plot of the local Alvén velocity ($\mathbf{V}_A$) against plasma bulk velocity in the de Hoffmann Teller frame ($\mathbf{V}'$) at ≈01:17:30 UT

The phase space data available for these transitions includes both the CIS-CODIF and CIS-HIA instruments for spacecraft 1 but only the CIS-CODIF instrument for spacecraft 4. Examination of the velocity phase space data for each of these indicates the existence of possible transmitted and reflected accelerated ion populations forming d-shaped Cowley distributions which stands as particle evidence for the presence of reconnection in the active interval between 01:15:00 and 01:18:00 UT. An example of these distributions is displayed in Figure 3.7 taken at 01:15:24 UT.

Similar behaviour is visible in the Tango (Spacecraft 4) data with possible D-shaped distributions present in data frames at 01:12:49, 01:13:29, 01:14:05, 01:14:53, 01:15:06, and 01:15:54 UT. Coincident with these observed frames are often strong modifications in the local bulk flow velocity magnitude and orientation that may now

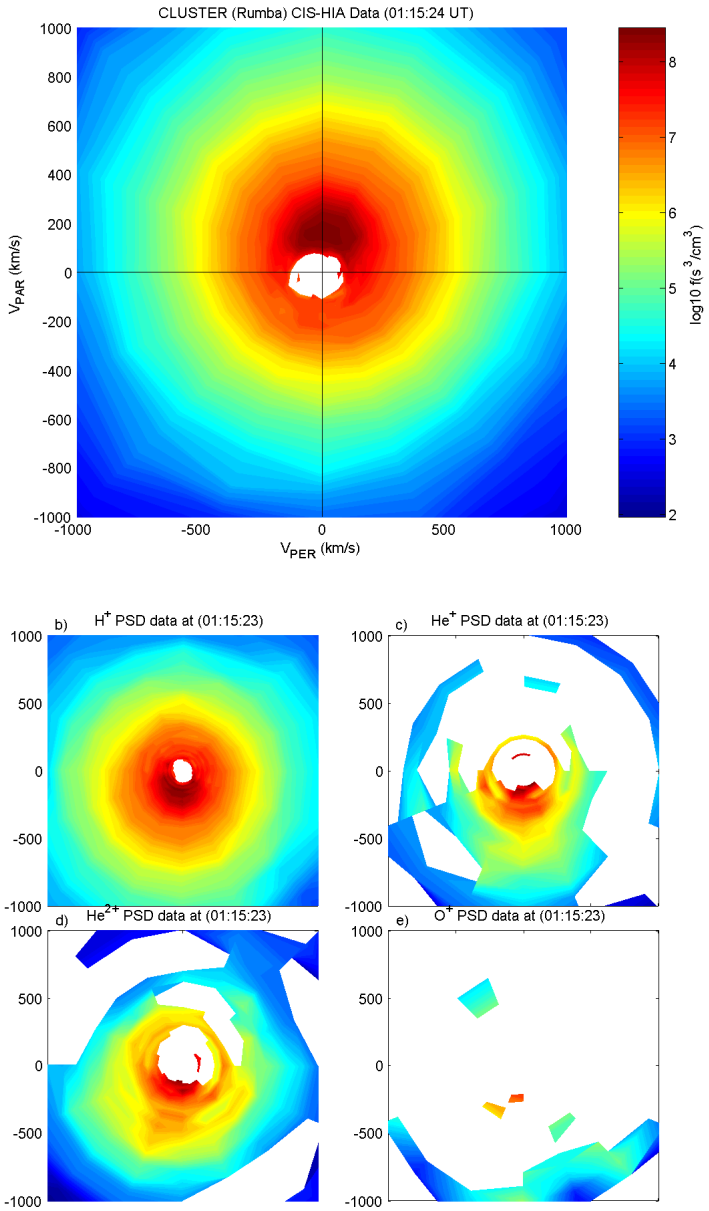

Figure 3.7: Spacecraft 1 CIS instrument data, from 1st April 2003 at ≈01:15:23 UT. Collected data from CIS-HIA (a, top) shows the D-shaped particle distribution in velocity phase space data, and CODIF (b-e) for different ion particle species; b) Hydrogen, c), Helium 1+, d) Helium 2+, d) Oxygen+.

be associated with the reconnection process. In this case the variance in observed data may not be due to the difficulty of estimating distributions based on low particle counts but by the spacecraft interacting with the boundary in an incomplete fashion due to a combination of magnetopause and spacecraft movement.

The recrossing of this boundary takes place a short time later and is clear in both magnetic and ion data for all of the CLUSTER spacecraft at approximately 01:18-01:19 UT. The data show significant variance after this crossing suggesting an incomplete transition of the boundary, a fluctuating boundary location, a highly turbulent transition region or different crossing geometries. As such accurate determination of the end point of the transition is difficult as there is no obvious stable region of observations. The normal vectors determined for the transition, therefore, show greater variance from one another than would usually be expected. The respective time of crossing and the related boundary normal vector is presented in Table 3.3.

SPC	Time (UT)	N_X	N_Y	N_Z
1	01:18:52	0.9668 ± 0.0014	-0.2470 ± 0.0042	0.0654 ± 0.0047
2	01:18:59	0.4321 ± 0.0182	-0.8315 ± 0.0193	-0.3492 ± 0.0378
3	01:19:01	0.7616 ± 0.0364	-0.5510 ± 0.0581	-0.3412 ± 0.0380
4	01:18:22	0.9179 ± 0.0212	-0.0326 ± 0.0157	-0.3955 ± 0.0494

Table 3.3: Calculated boundary normal vectors for the grouped transition at 01:19 UT listed by spacecraft number. The results of multiple methods have been compiled and used here along with the time index each spacecraft interacted with the transition layer. Normal vector 1 is the result of the Tangential Discontinuity method, vectors 2, 3 & 4 are derived from Minimum Variance Analysis.

The model normal vector for this crossing using the Shue et al. (1997) model gives a vector of $GSE(x, y, z) = (0.8747, -0.0211, 0.4843)$. This shows significant divergence from the values arrived at through other methods. Close examination of the positional information shows that the spacecraft transits may indeed be across the cusp region leading to transitions while apparently still within the magnetopause as defined by this model. The vector may therefore be representative of the surface at the spatial extent of the magnetopause boundary without being applicable to the trans-cusp crossing itself.

A model based on mapping the magnetic morphology, including field lines, such as T96 (Tsyganeko, 1996) gives a better approximation.

The higher variance also makes this crossing unsuitable for simulation. It does not, however, prevent the use of de Hoffmann-Teller analysis and application of the Walèn tangential stress relation. The results of the dHT and Walèn analysis methods are presented numerically in Tables 3.4 and 3.5, and graphically in Figures 3.8 and 3.9 respectively.

Spacecraft	V_{HTX}	V_{HTY}	V_{HTZ}	A	C	D/D0
1	185.95	-286.79	-7.17	1.01	0.90	0.18
2	N/A	N/A	N/A	N/A	N/A	N/A
3	224.16	-323.50	-71.14	1.00	0.95	0.08
4	169.41	-217.05	-104.38	1.06	0.97	0.04

Table 3.4: Results of dHT analyses over the boundary transitions at 01:19 UT on 1st April 2003 for all spacecraft.

Spacecraft	Linear Regression Gradient (∇)	Correlation Coefficient (C)
1	0.65	0.81
2	N/A	N/A
3	1.49	0.83
4	0.92	1.00

Table 3.5: Results of tangential stress balance, Walèn relation, linear regression testing for all spacecraft at 01:19 UT on 1st April 2003.

Each of the spacecraft, with an approximately unity gradient, high correlation coefficient and significant decrease in convective electric field meets the criteria of describing a possible quasi-static structure, a possible reconnection layer. Further evidence is found in the Walèn results. In each case the correlation coefficient is significant. The different gradients suggest different acceleration mechanisms, however. A unity gradient is viewed as a confirmation of Alfvénic acceleration taking place whereas a 0.66 gradient, as in spacecraft 1, is said to suggest the presence of a slow shock. This does, of course, depend on the data range sampled and a reconnection layer evidencing both wave modes, as in the model, may show both at different times.

These results present evidence that there is not only a quasi-static structure to

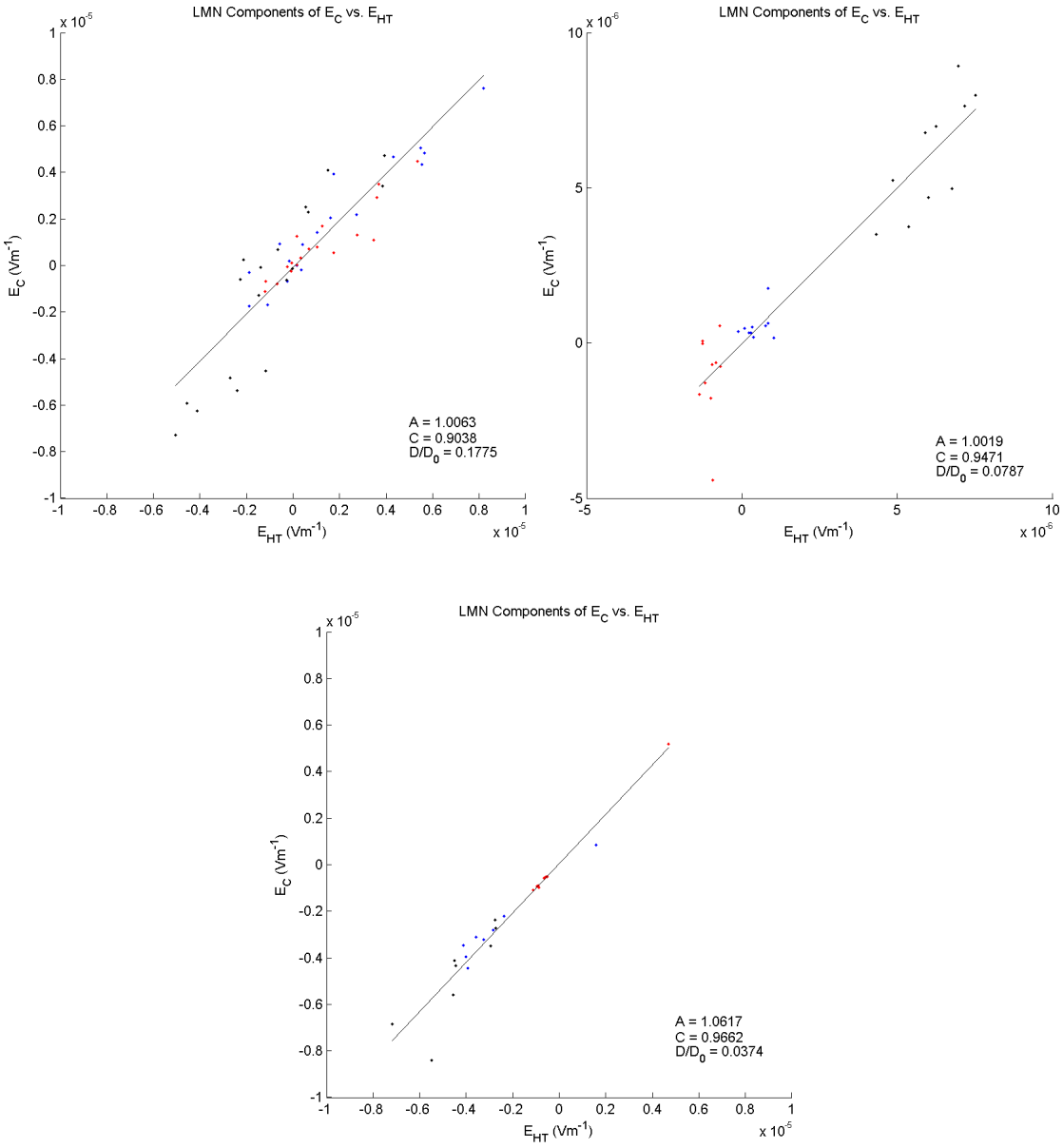

Figure 3.8: de Hoffmann-Teller analysis plots for spacecrafts with active CIS instruments (1, 3 & 4) at 01:19 UT on 1st April 2003.

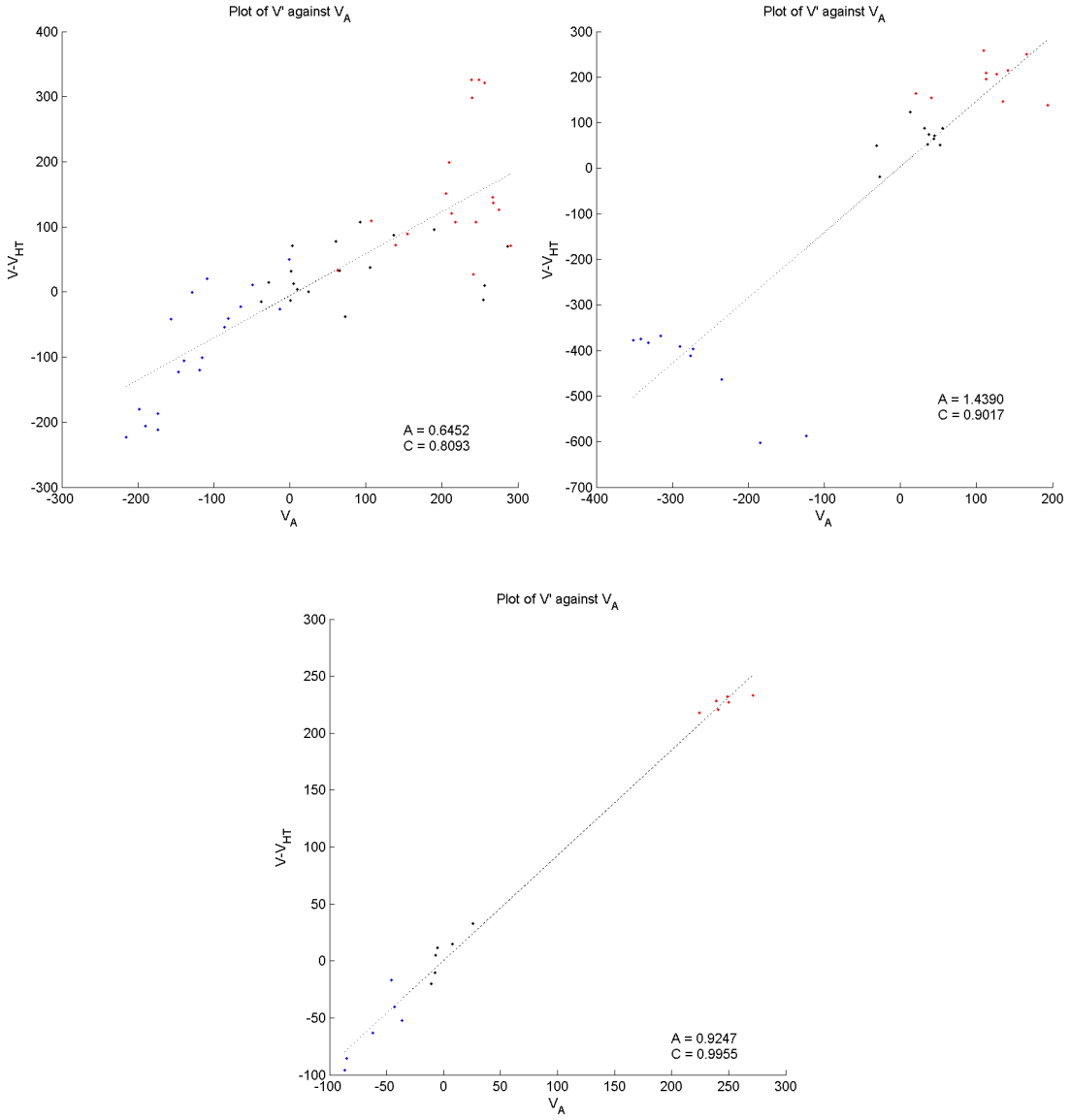

Figure 3.9: Scatter plots for Walèn relation test data for the transitions at 01:19 UT on 1st April 2003 carried out for spacecrafts 1, 3 & 4.

the transition layer that the four CLUSTER spacecraft are passing though, but that quasi-static structure may be subject to Alfvénic acceleration of the bulk plasma velocity in line with the predictions of reconnection theory.

The particle velocity phase space distributions for these features suggests the presence of coherent structures but does not, in fact, show clear d-shaped distributions that could be correlated with reconnective behaviour.

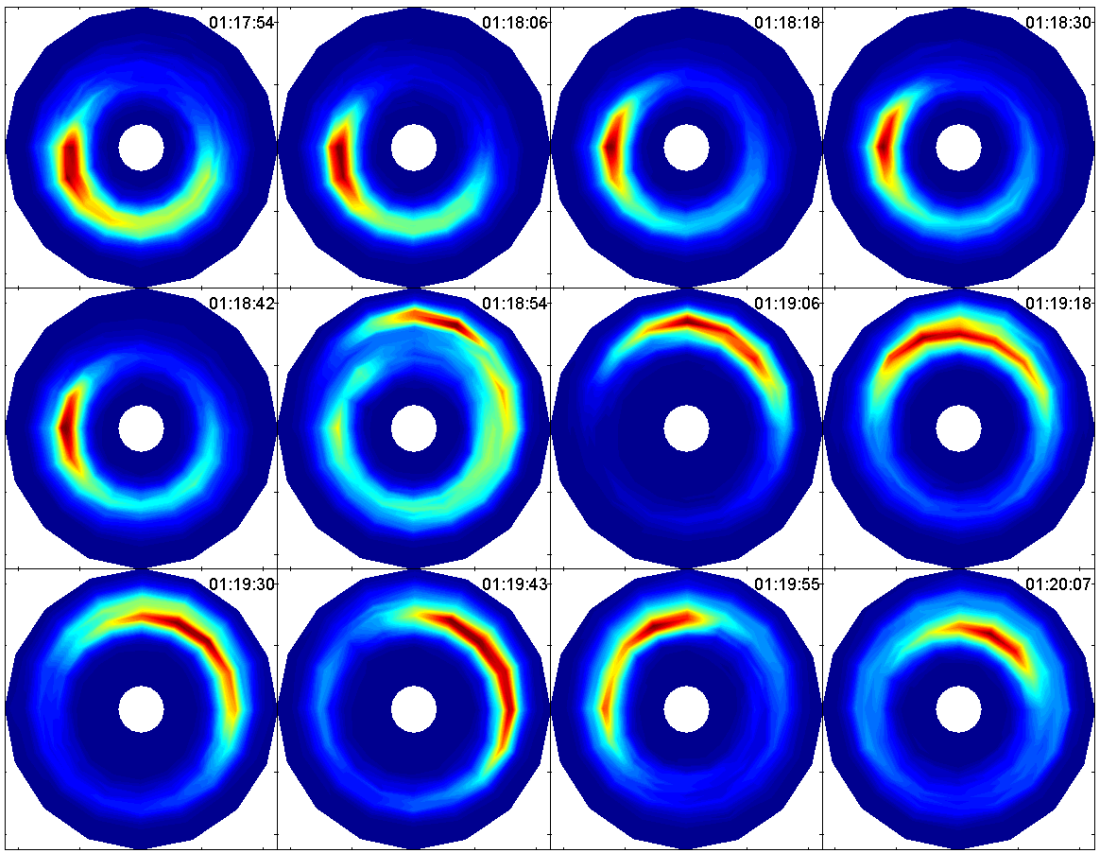

Figure 3.10: Omnipolar, azimuthal energy spectrograms, compiled from CIS-HIA data collected by spacecraft 1, of the transition at ≈01:18:52 UT on 1st April 2003. Increasing energy, as a log10 value, is represented by radial distance from the the centre of each spectrogram. The energy range shown is 6ev to 29KeV. In this case the transition frame is clear at 01:18:54 UT where the pre-crossing and post-crossing flow patterns are both recorded in addition to a possible direction of travel.

The spectrograms in Figure 3.10 show clear signs of a focussed distribution both before and after the transition at 01:18:52 UT. Smearing of the distribution may be due to variability in the plasma being sampled due to being in the cusp boundary layer or minor interactions with the magnetopause itself. While these factors do not preclude the simulative methods being used in this case, they do introduce further

factors which make it unsuitable for inclusion in this study.

The final complete crossing in the initial period of activity takes place at across an extended period depending on the spacecraft in question.

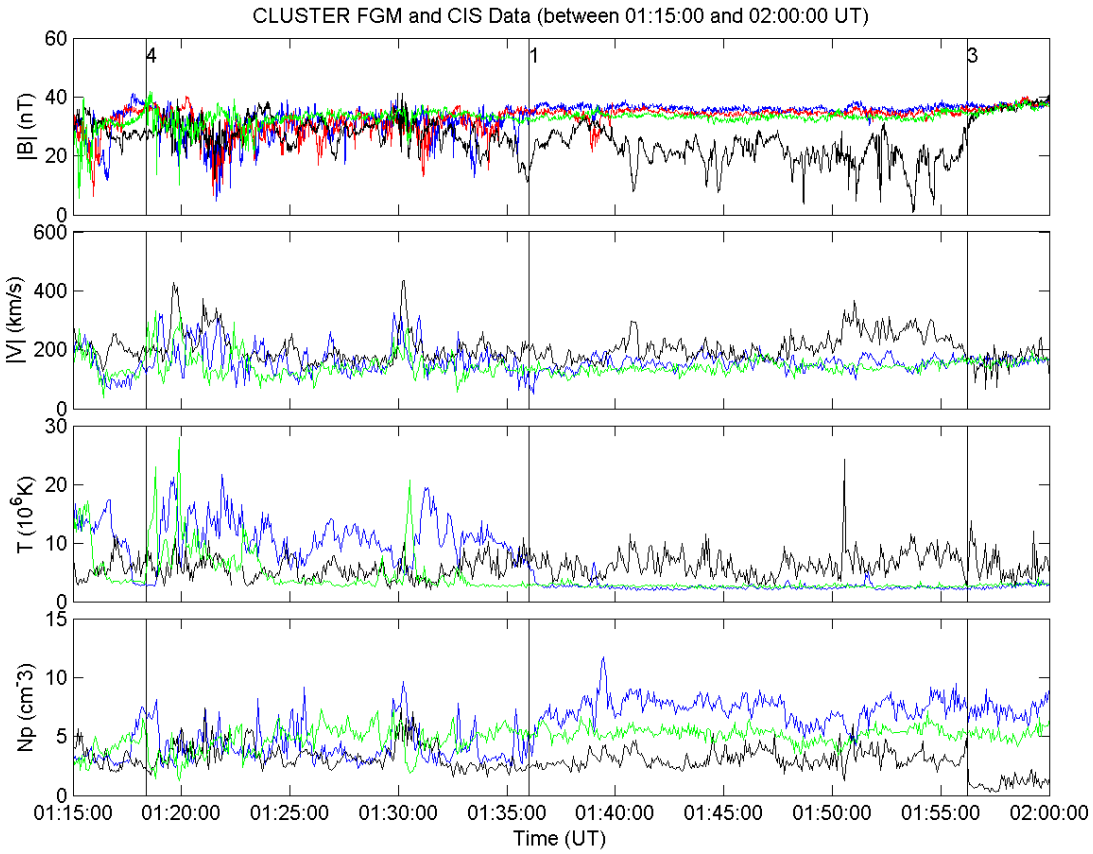

Figure 3.11: Plasma parameter data for all spacecraft from 01:15 to 02:00 UT on 1st April 2003, with vertical bars denoting the timing of the final crossing for each spacecraft with an active CIS instrument [1 (blue), 3 (black) & 4 (green)]

In this case the boundary normal analysis has been somewhat simplified due to the increasing, but not tangentially discontinuous, magnetic shear of the transitions which leads to a decrease in the possibility of degeneracy of the normal vector solutions calculated. The maximum separation between the spacecraft has been calculated as being ≈5500km, taking into account the mean velocity of the spacecraft during this time (≈280km/s) the temporal separation of crossings due to traversing this intervening distance should only be of the order of 20 seconds. As the separation is almost 20 minutes this suggests structural differences along the transition paths of the spacecraft. The spacecraft position and velocity data for spacecrafts 1 and 4 for this period were the same in the data retrieved from the CLUSTER Active

Archive.

SPC	Crossing Time (UT)	N_X	N_Y	N_Z
1	01:36:00	0.9779 ± 0.0015	-0.2022 ± 0.0059	0.0524 ± 0.0056
2	01:34:35	0.9763 ± 0.0023	-0.2130 ± 0.0084	0.0380 ± 0.0012
3	01:56:15	0.9799 ± 0.0010	-0.1987 ± 0.0056	-0.0157 ± 0.0087
4	01:18:22	0.9866 ± 0.0049	-0.1631 ± 0.0241	0.0095 ± 0.0707

Table 3.6: A summary of the boundary normal vectors for the 4 spacecraft during their final, identifiable, transition before the onset of the cusp transition described by Zheng et al. (2005) at 01:30 UT. All were calculated using the tangential discontinuity method.

The vectors in Table 3.6 show significant congruity in value even across the significant temporal interval. The tangential discontinuity method providing solutions that best fit the criteria for selection may add credence to the observation of increased magnetic shear in these latter cases.

SPC	V_{HTL}	V_{HTM}	V_{HTN}	∇	C	D/D0
1	287.01	-181.59	-3.31	1.00	0.96	0.07
2	N/A	N/A	N/A	N/A	N/A	N/A
3	-136.59	-105.82	-30.86	0.95	0.98	0.03
4	197.39	-211.57	-54.61	1.07	0.98	0.04

Table 3.7: The results of dHT analyses over the final pre-cusp boundary transitions for all spacecraft on 1st April 2003, showing de Hoffmann Teller velocity (V_{HT}), linear regression gradient (∇), correlation coefficient (C) and convective electric field reduction factor ($D/D0$).

The near unity values of the linear regression gradient suggest the presence of a quasi-static structure convecting, in this case, along the magnetopause boundary. The low value of the residual D/D_0 factor shows it to be well defined, for all spacecraft.

SPC	Linear Regression Gradient (∇)	Correlation Coefficient (C)
1	0.83	0.9751
2	N/A	N/A
3	0.08	0.77
4	0.93	1.00

Table 3.8: Results of tangential stress balance, Walèn relation, linear regression testing for all spacecraft, on 1st April 2003, during the final pre-cusp boundary transition.

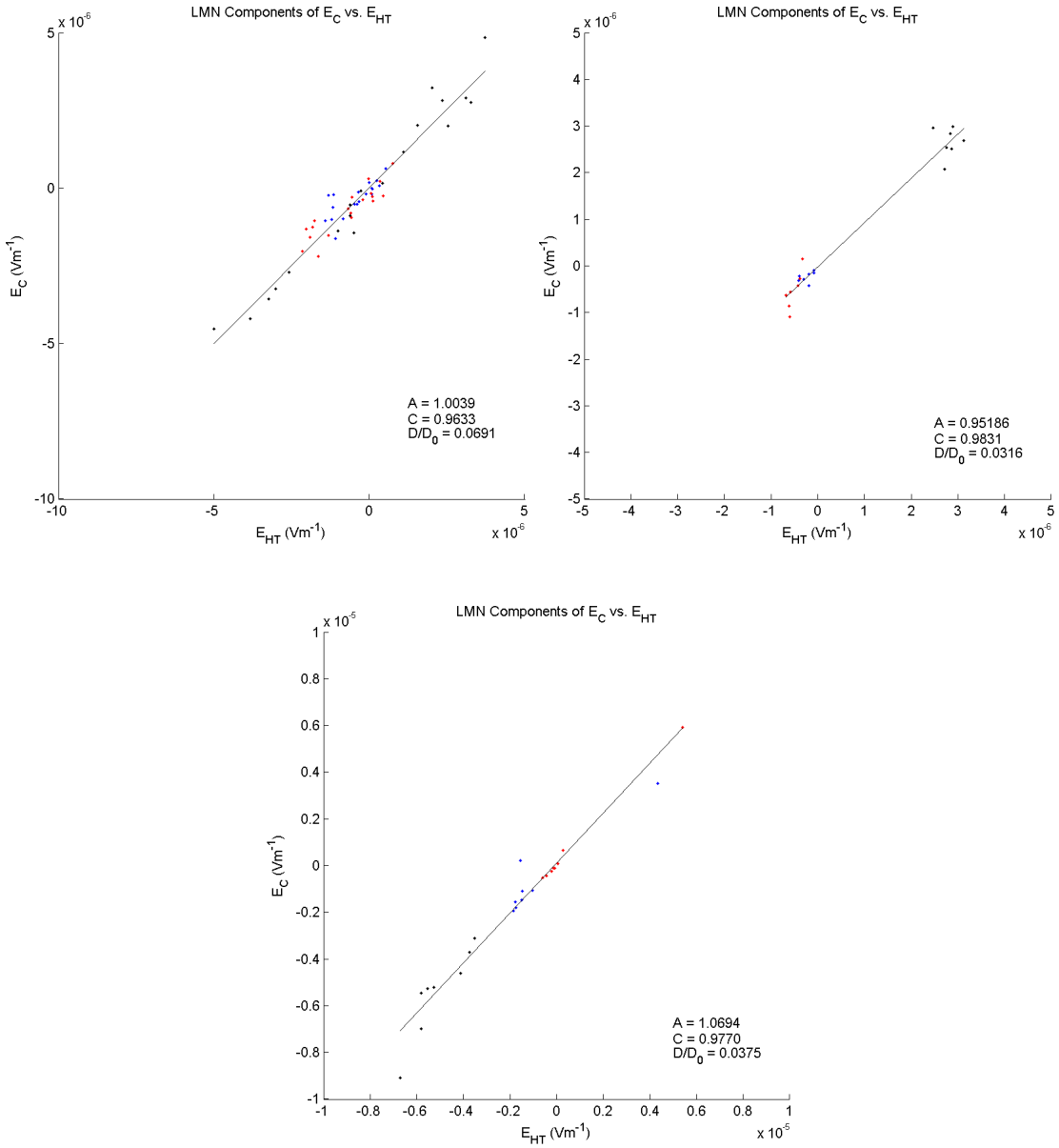

Figure 3.12: de Hoffmann-Teller analysis plots for spacecrafts with CIS instruments (1, 3 & 4) over the final identifiable crossing in the pre-cusp transition period of activity.

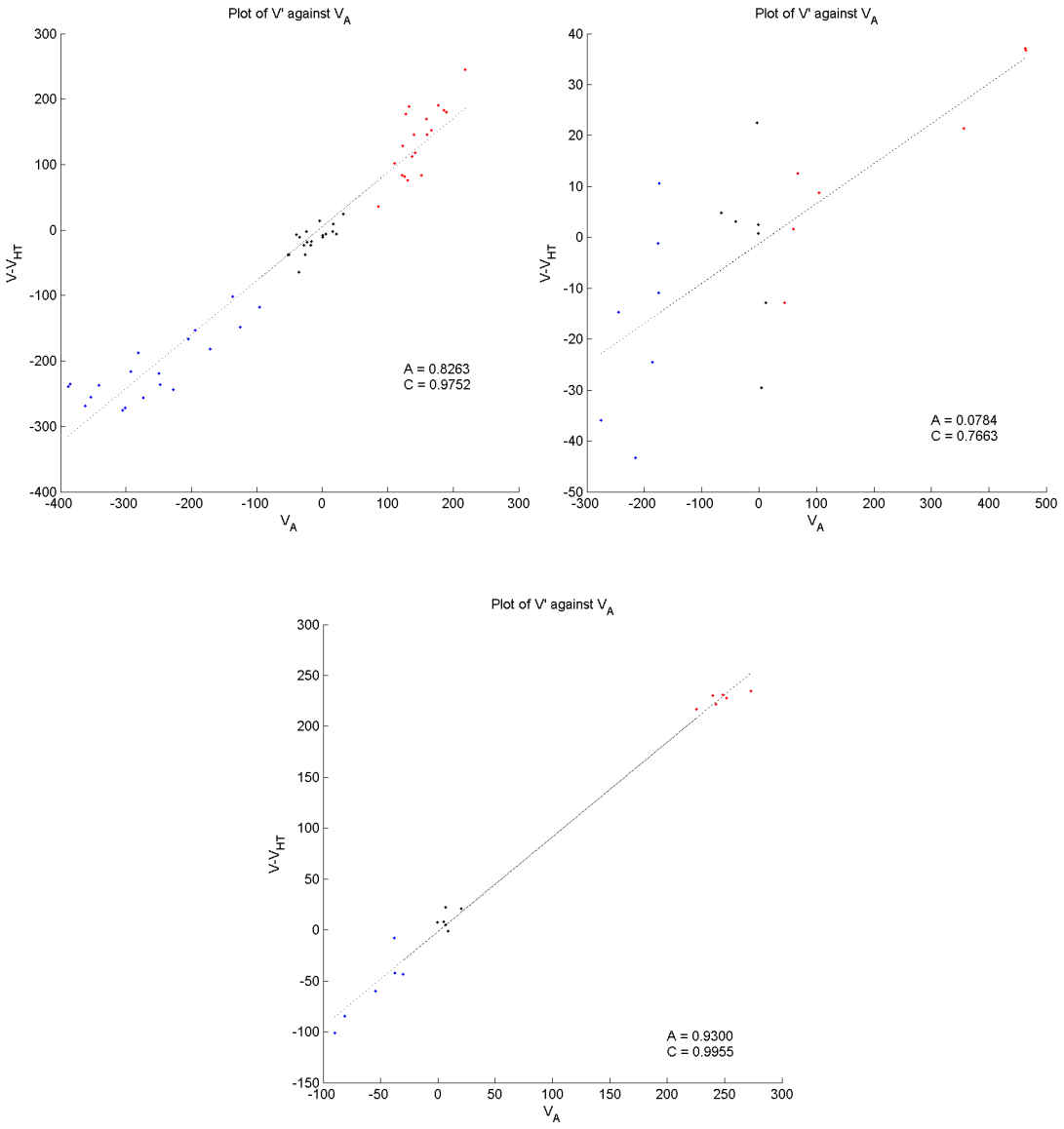

Figure 3.13: Tangential stress balance (Walèn) linear regression plots for spacecrafts 1, 3 and 4 over the final crossings at ≈ 01:18:30UT (1 & 4) and ≈ 01:56:00UT (3).

Velocity phase space distributions for the crossings at these times show evidence of the presence of transmitted and reflected ion populations that correlate with the degree of agreement with the Walèn relation. In Figure 3.14, for spacecraft 1, we see that the strongest feature is not perfectly field aligned. This may lead to the non-unity regression gradient calculated during the Walèn test. There is, however, a coherent velocity flow, suggested by the correlation coefficient of 0.98, that is aligned along the magnetopause boundary, as might be expected from material exiting a reconnection region as a jet. Spacecraft 3, for this crossing does not show good agreement with the Walèn relation. Being temporally separated from the other two spacecraft crossings it is important to consider the possibility that both the spatial and temporal factors affected this result. In fact the bulk velocity data for spacecraft 3 at this time does not show the strong signatures present for the other spacecraft, but during earlier incomplete crossings that occur at coincident times with those observed by the other spacecraft, at ≈01:20 and ≈01:30 UT. Both of these show velocity enhancements of several hundred km/s. Spacecraft 4, with access only to the CODIF instrument, again evidences flow both parallel and perpendicular to the calculated magnetopause normal suggesting the presence of ion flow across the magnetopause in addition to accelerated flows along it.

Apart from these complete crossings there are multiple cases in the first period of activity where the spacecraft clearly interact with a structure that evidences both field and ion effects but are not demonstrably complete. In these cases it is possible to examine normal vectors from such methods as minimum variance analysis as well as calculating the results of the de Hoffmann Teller analysis and the Walèn tangential stress balance relation. Without a clear normal vector, and thus the ability to translate the data into the frame of the moving magnetopause, it is difficult to relate these results to the other more complete interactions.

Evidence of reconnective flow behaviour was reported in the original paper at a multitude of times. A few were expressed in specific terms. I have conducted my own analyses of these “flow reversals”. The results are presented in Table 3.9. There

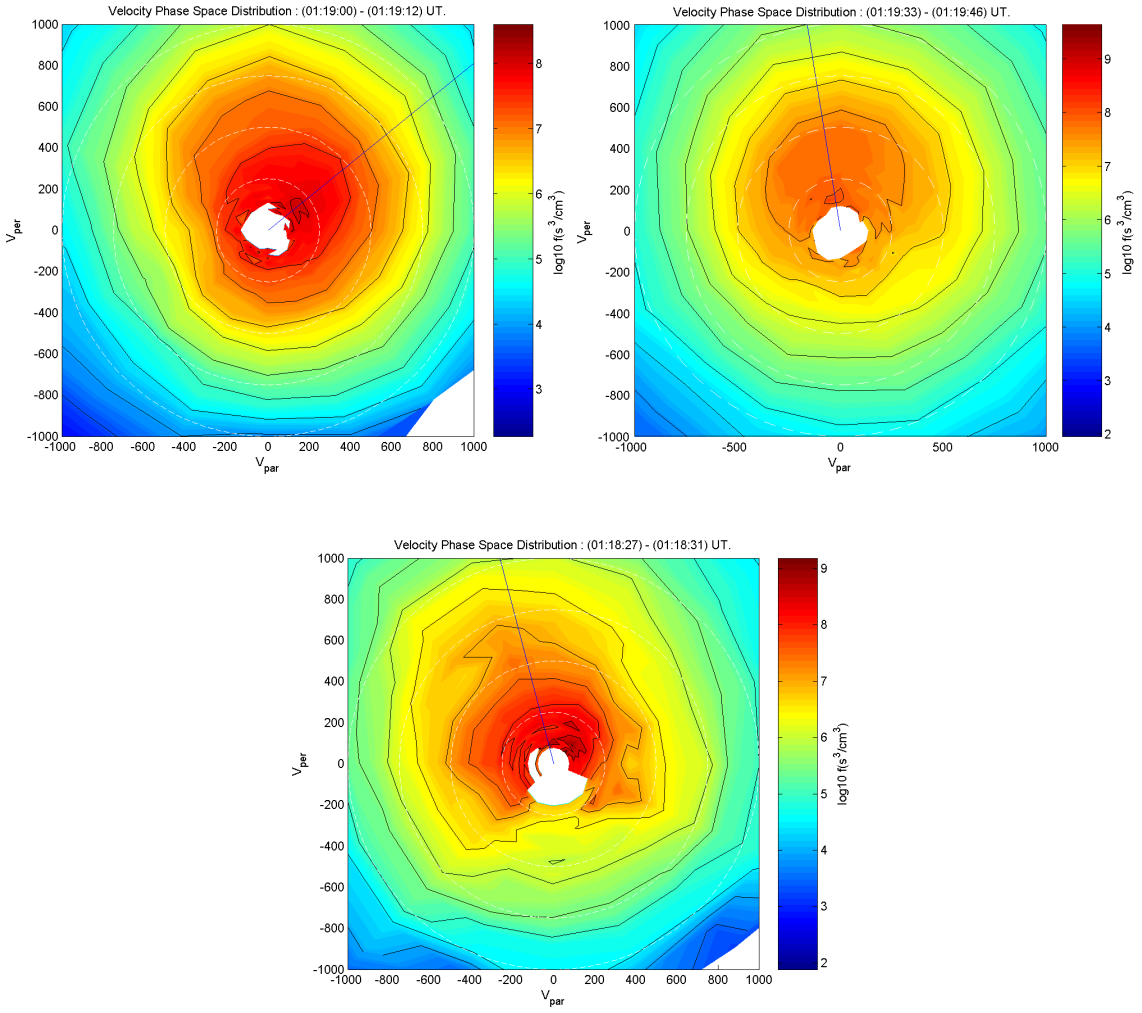

Figure 3.14: Sample velocity phase space diagram frames for each spacecraft showing incidence of transient ion populations and possible Cowley d-shaped distributions for spacecrafts 1 (HIA), 3 (HIA) & 4 (CODIF). The normal vector, denoting the direction of the magnetopause, has been calculated for each event and is shown by the blue line.

is clear evidence of meeting both the criteria for a well defined dHT frame and that the correlation coefficient of the Walèn relation is high enough to suggest that the accelerated flow in question has its roots in a region that either is undergoing, or has undergone, reconnection.

		de Hoffmann Teller				Walèn	
SPC	Time (UT)	V_{HTN}	∇	C	D/D0	∇	C
1							
	01:17:30	-72.45	1.01	0.96	0.05	0.80	0.99
	01:19:00	-7.17	1.01	0.90	0.18	0.65	0.81
	01:29:30	-51.98	1.00	0.99	0.03	1.09	0.97
	01:31:00	12.15	1.00	1.00	0.00	0.46	0.97
3							
	02:34:00	-36.25	1.00	1.00	0.00*	-1.04	-1.00
	02:41:30	-107.43	1.00	1.00	0.00*	0.83	1.00
	02:53:30	-54.20	1.04	0.96	0.08	0.54	0.80
	02:55:30	-33.38	1.01	1.00	0.00	0.63	0.95

Table 3.9: Results of non-crossing-specific accelerated flows specified in (Zheng et al., 2005) after testing for a de Hoffmann-Teller transformation frame and agreement Walèn Stress Balance relation, quantified in terms of the linear regression Gradient (∇) and Correlation Coefficient (C). The starred cases denote a test carried out on a single data, mid acceleration peak, point.

3.2.3 Simulation Analysis

Event 1: 02:27UT

As can be clearly seen in the event overview presented in Figure 3.15, the transition across the layer is comparatively short, with modifications to all affected variables taking place over a period spanning somewhat less than 3 minutes.

Large perturbations in all state variables are visible in addition to significant migration, in the energy spectrum, of the particle population across the boundary. The nature of these changes, change from lower temperature, higher density to higher temperature lower density suggests a spacecraft passing inwards from the magnetosheath into the magnetopause transition region.

The unshifted data show evidence of enhancements in the bulk velocity coincident with the transition.

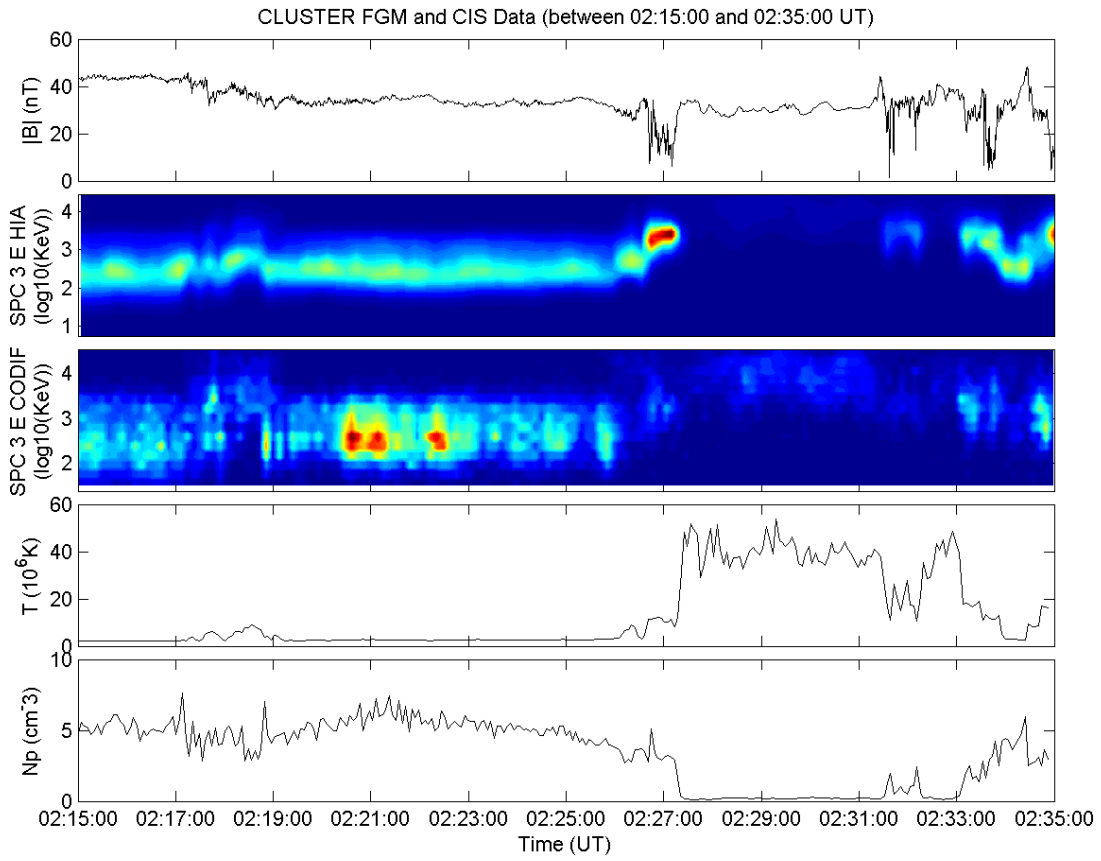

Figure 3.15: An overview of plasma parameters B, T and N, using spacecraft 3 data from 1st April 2003, with omni-directional azimuthal energy spectrograms for the HIA (upper) and CODIF (lower) instruments. The transition across the reconnection layer is clear between 02:25 and 02:28 UT.

Calculation of the boundary normal vector for this transition is comparatively simple given the high shear and clear beginning and end points. The extensive stable regions on either side of the layer give room to use the tangential discontinuity method in addition to the basis model normal and more complex minimum variance analyses. The results of these calculations are that the method with the lowest gradient and variance over the sampled region is MVA which provides a normal vector of $GSE(x, y, z) = (0.5299 \pm 0.0168, 0.2013 \pm 0.0190, 0.8238 \pm 0.0151)$.

When the data is transformed into the boundary normal frame the trends become clearer. Both the CIS-CODIF and CIS-HIA instruments record impulse acceleration of the bulk plasma velocity across the transition that is temporally coincident with changes in the magnetic field magnitude. Before subjecting this data to de Hoffmann Teller analysis to attempt to establish a structural frame, the energy spectrograms

for this event were scrutinised to explore the degree of coherence or dispersion of the distribution function across the transition.

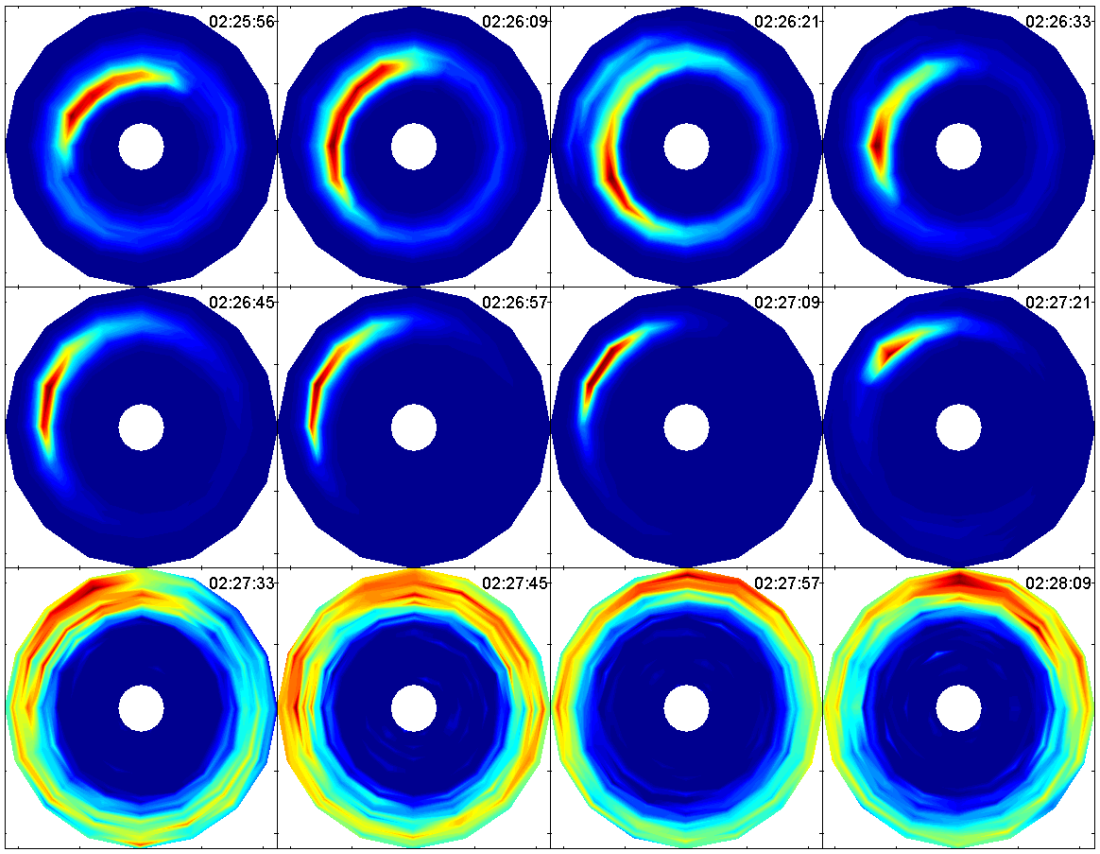

Figure 3.16: Omnipolar, azimuthal energy spectrograms sampled by the CIS-HIA instrument across the spacecraft 3 transition at 02:27 UT on 1st April 2003. The axes used are the same as those described in Figure 3.10.

The spectrograms in Figure 3.16 clearly show that between 02:25:56 and 02:27:21 UT the azimuthal and energetic coherence of the distribution is well defined. From 02:27:33 UT onwards this definition is lost. The data for the corrected total counts shows that at this point, between 02:27:03 and 02:27:27 UT, there is a 94% decrease in the number density of the particles which, using subsequent moment data is a reduction from 3.3 particles/cm^3 to 0.2 particles/cm^3. This change is a significant enough reduction to explain the observed subsequent smearing of the distributions.

Structures suggesting the presence of D-shaped velocity phase distributions are present in the data from approximately 02:26:27 to 02:27:27 UT. An example of one of these distributions can be seen in Figure 3.17. This suggests field aligned particle flow and mirroring in such a way as to give evidence to the plasma sampled being

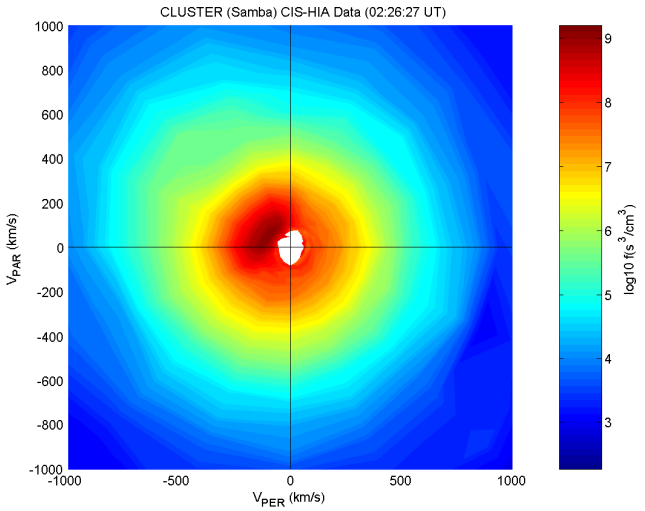

Figure 3.17: An example of a possible D-shaped distribution in the Velocity Phase Space data for spacecraft 3 during the transition. The sample time for this particular frame was from 02:26:21UT to 02:26:33 UT on 1st April 2003.

within a region of open field topology (Cowley, 1982).

Examining the bulk velocity profile for the transition event (Figure 3.18), the previously described significant enhancements in the tangential component corresponding with the magnetic field changes are seen to occur between 02:26:30 and 02:27:30 UT. At this same time there is comparatively little alteration in the parallel component or, in fact, the vector alignment of the flow. This latter observation may help to explain why these changes are, in fact, so clear since any acceleration acting with the pre-existing flow rather than against it will be enhanced.

Sampling from the region over which the velocity evidences these changes in the CIS-HIA data, de Hoffmann Teller analysis was performed in two places, from 02:26:40 to 02:27:05 UT and 02:27:17 to 02:27:29 UT. The numerical results are presented in Table 3.10, the linear regression plots for each of these two periods are in Figures 3.19 (a) and (b) respectively.

Time (UT)	V_{HTX}	V_{HTY}	V_{HTZ}	A	C	D/D0
02:26:53	314.91	-296.21	64.50	0.98	0.98	0.03
02:27:23	186.79	-238.09	70.46	1.00	0.96	0.07

Table 3.10: Results of dHT analyses on CIS-HIA data over the boundary transitions for spacecraft 3 in the vicinity of the two times specified.

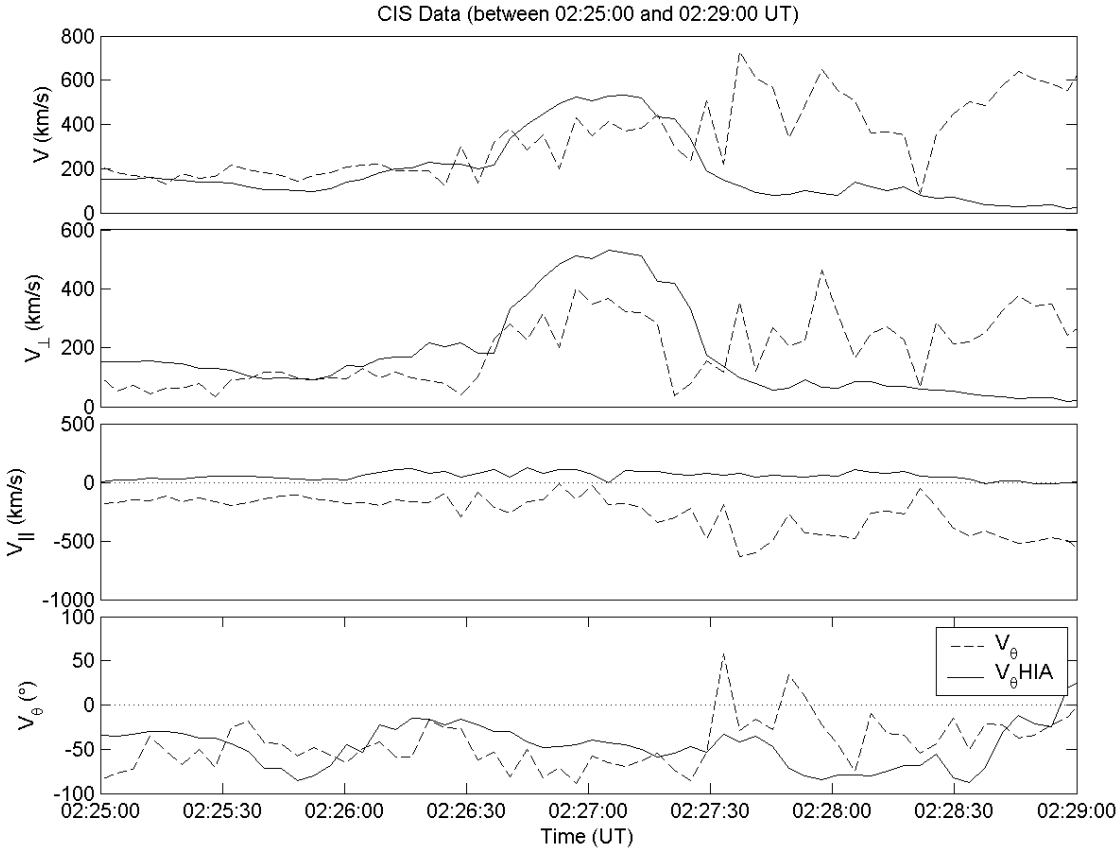

Figure 3.18: Bulk velocity data, in the boundary normal frame, for spacecraft 3 instruments CIS-CODIF (dashed) and CIS-HIA (solid). The top frame contains the magnitude $|V|$. The $V_{\parallel}$ and $V_{\perp}$ data are constructed with respect to the previously calculated magnetopause surface normal. V_{θ} is then calculated based on the alignment of $V_{\perp}$. $V_{\parallel}$ is therefore a scalar quantity as V_{θ} supplies the required orientation information.

Using the deHoffmann-Teller velocities calculated above a pointwise comparison to the Walèn relation was carried out. Individual vector comparisons with the Walèn relation hold as well as interval testing and also give a possible way to identify points in the time series where there is onset of a particular flow through increasing correlation values, changes in flow orientation and identification of orientation of the spacecraft with respect to the reconnection x-line. In each of the above cases we can see, in Figure 3.20, a very similar calculated behaviour across the feature itself. Both evidence negative correlation coefficient and gradient on the nearside, switching to positive in the second half of the feature.

Taking into consideration the high variability seen in the moment data for this crossing after the number density had decreased, longer intervals than usual were

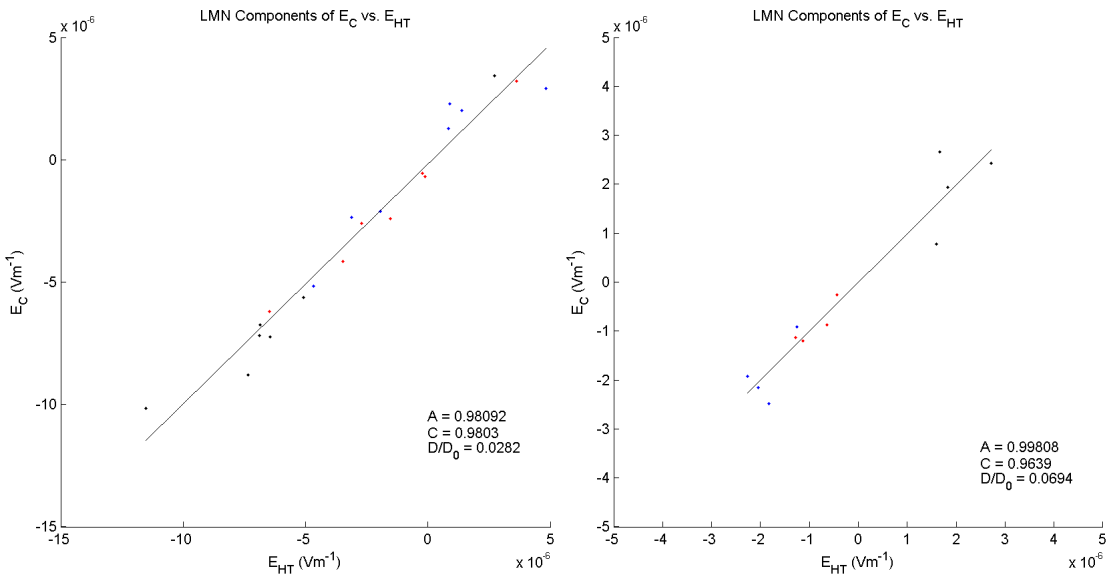

Figure 3.19: The dHT analysis results for the two periods comprising the acceleration of flow at (a) ≈ 02:26:53 UT (left) and (b) ≈ 02:27:23 UT (right). Both evidence comparatively good agreement with the criterion for the existence a well defined de Hoffmann-Teller frame.

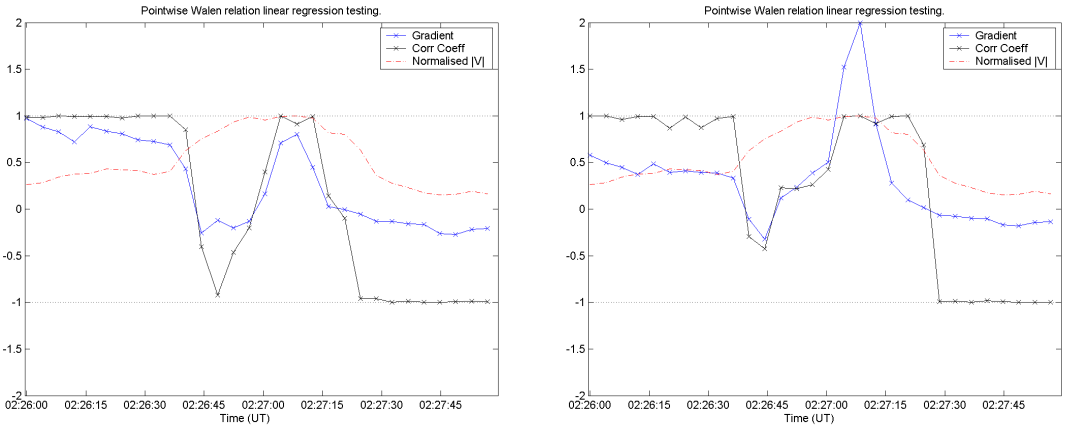

Figure 3.20: The results of a pointwise (4 second resolution) incremental scan across the feature interval, using a general linear regression fitting test against the predictions made by the Walèn relation and recording both the gradient and correlation coefficient of each vector comparison. The dHT frame velocities used for these two tests are those given in Table 3.10.

used on either side of the crossing as a measure to decrease the effect of local noise during the averaging process.

Pre-Layer Components. Taken from 02:23:00 to 02:25:00 UT			
Variable	Value	Absolute Statistical Error	Percentage Error
$B_L(nT)$	-6.2162	2.62	8.03
$B_M(nT)$	31.4533	1.05	3.22
$V_L(km/s)$	96.1633	1.78	1.85
$V_M(km/s)$	-91.0985	1.14	1.25
$N(/cm^3)$	5.1521	0.06	1.20
$T(10^6K)$	26.3520	0.21	0.79
Post-Layer Components. Taken from 02:28:00 to 02:31:00 UT			
Variable	Value	Absolute Statistical Error	Percentage Error
$B_L(nT)$	15.3890	1.49	4.97
$B_M(nT)$	-24.1463	1.47	4.90
$V_L(km/s)$	-18.0325	3.53	19.58
$V_M(km/s)$	-32.7769	3.21	9.79
$N(/cm^3)$	0.2013	0.00	2.12
$T(10^6K)$	399.3610	7.14	1.79

Table 3.11: Pre and post crossing plasma parameter components used to provide the initial pass at creating the model for the event recorded at 02:27 UT on 1st April 2003.

As can be seen from Table 3.11, the long intervals were successful in keep statistical errors down, in all but one case, to less that 10% of the total magnitude. These values, once calculated were used to create the first pass of the model structure.

The structure created immediately gives us 2 important results:

1. Both of the η values calculated were less than unity (0.8113 and 0.8676), suggesting the presence of two slow shocks in the layer.

2. The value of $|\mathbf{b}|$ was such that it was above the switch-on point for reconnection in this model but less than the limit at which one of the slow shocks becomes a slow expansion fan.

3. It should be noted, however, that the value of $|\mathbf{b}|$ was 98% of the value for a Region III structure and so raises the question of whether it is possible to see an evolution of wave type with time/space. In this limit the theory suggests that the slow shock on the side where there is the lower magnetic field strength

disappears. This is something that was borne in mind when comparing the resultant structure to the observational data.

Consequent analyses through the use of genetic algorithms are collected and presented in §4.1.1 and §4.2.1 for the RLDS and BVSR algorithms respectively.

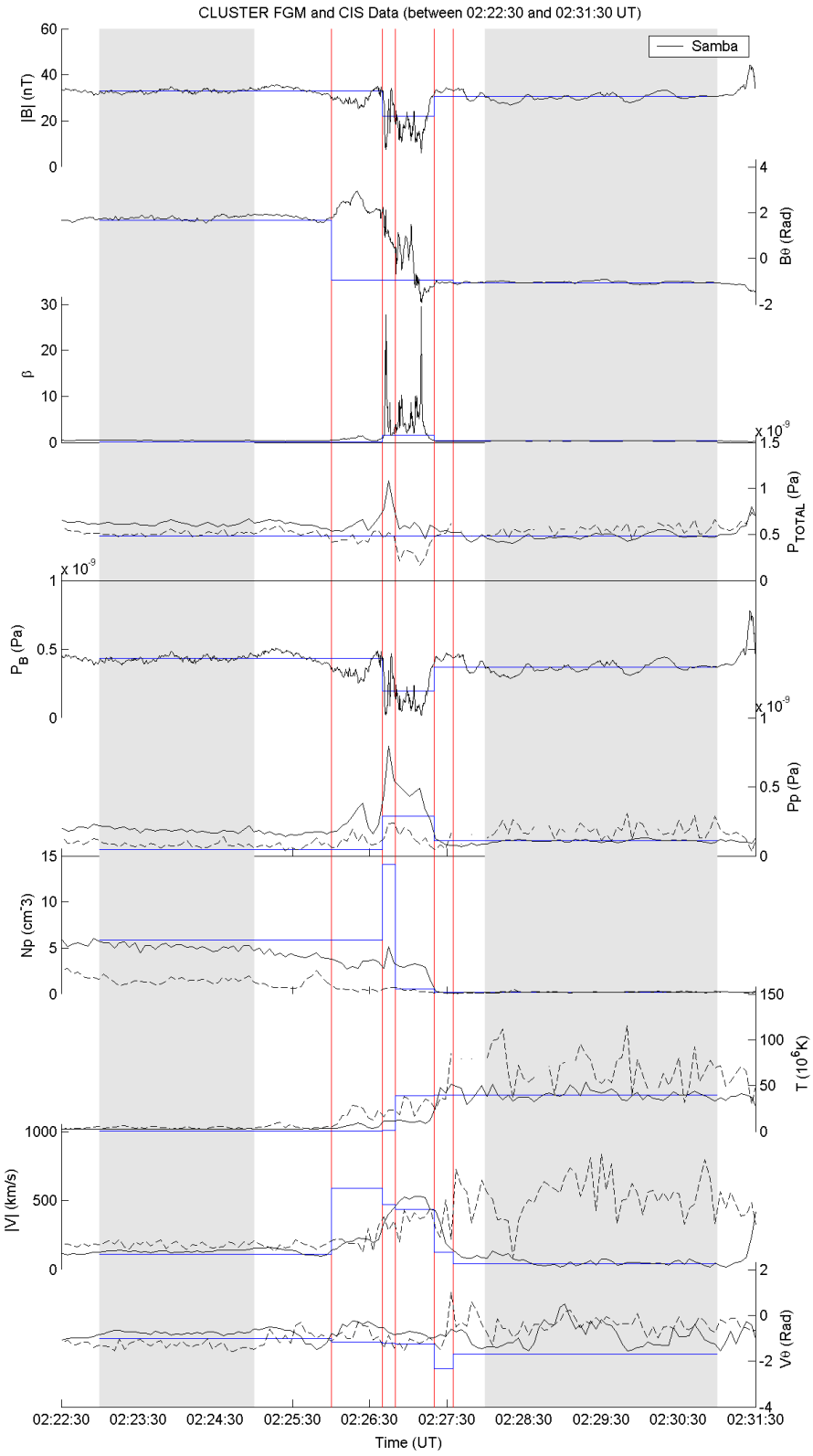

Figure 3.21: Comparative overlay of the reconnection layer model created by the simulation using the initial conditions previously specified for all magnetic and plasma variables. Observed data is presented in black, modelled in blue, the discontinuities are marked by red vertical lines and the ranges used for boundary condition sampling are shown in grey.

Event 2: 02:35UT

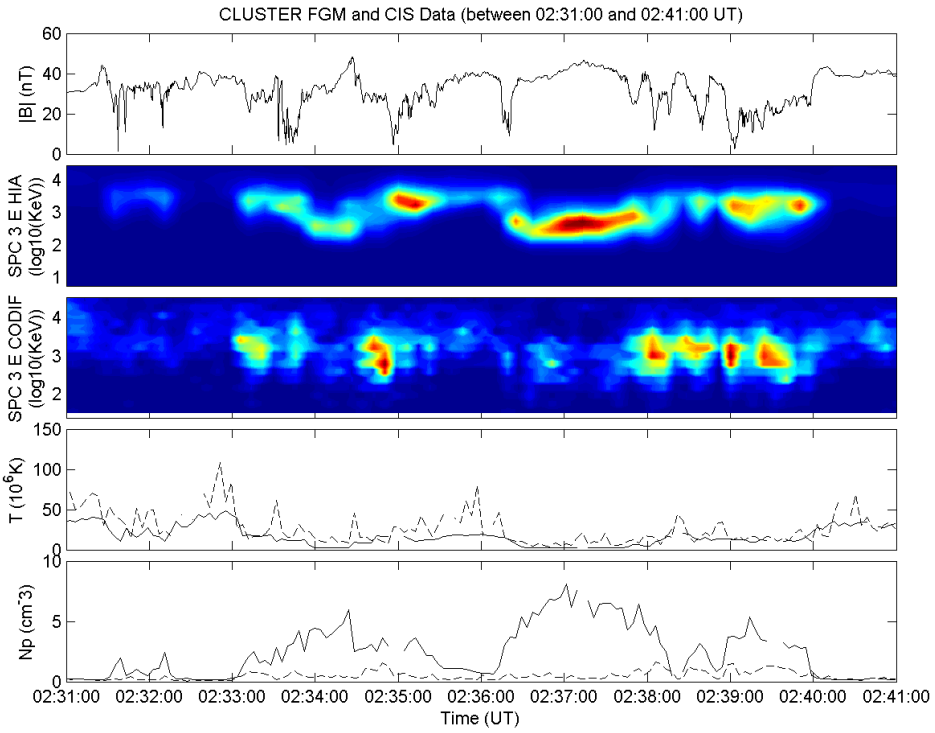

Figure 3.22: Event overview in plasma parameters with omni-directional energy spectrograms for the CIS-HIA and CIS-CODIF instruments from spacecraft 3 data from ≈ 02:31:00 - 02:41:00 UT on 1st April 2003. Data from both CIS instruments is also presented for T and N, this CIS-HIA data in this case is represented by the solid line.

This event evidences strong signatures in both the magnetic field and plasma data shown in Figure 3.22. There is, significant variance present in plasma variables during periods of low number density. While signatures are present in the data from both spacecraft those variations are clearer in the HIA data as they seem to be subject to less variation. This is likely due to the higher number of recorded particles (number density) which allow more accurate, and stable, calculation of the moments from the distribution. As such, primary use will be made of the CIS-HIA data.

The spacecraft at this time are located almost directly sunwards of the earth in the high-latitude northern hemisphere ($GSE(x, y, z) \approx (8.6, -1.2, 7.0)R_E$) determination of the grouping is complicated by the fact that the location and velocity data procurable for this time suggest that the position and velocity vectors of spacecrafts

1 and 4 are identical. This is unlikely to be accurate and may be due to an archival error. It may be possible to consider defining which spacecraft the mixed data corresponds to in terms of the interval between the times at which each spacecraft interacts with the structures comprising this crossing. The spacecraft 1 & 4 data details a position that is geometrically between, in pure distance for the earth terms, spacecrafts 2 & 3 and as such it might simply be expected that it would interact with the transition layer at a time between these two. Since neither spacecraft fulfill this simple requirement completely it is impossible to easily say which spacecraft this data should be attributed to. As such, it is only possible to consider the positions of the two unique spacecraft (2 & 3) and one conglomerated one, (1 & 4). The geometry in this case ten reduces to a planar arrangement, a triangle, with the distance order running from spacecraft 3 as the closest to 1 & 4 together followed by 2. The average separation between the spacecraft during the interval covered by Figure 3.22 is of the order of ≈4000km.

Boundary normal determination analysis was attempted for each of the 4 CLUSTER spacecraft as there were observed co-temporal fluctuations in magnetic field strength and orientation for all spacecraft. The magnitude of these was not uniform across the group but showed significant variation from spacecraft to spacecraft. As such, the results of each type of method analysis will be presented separately before being collated to compare resultant normal vectors. It is important to note, at this time, that only spacecrafts 2 & 3 evidenced similar signs of having completed the transition across the magnetopause, and of these two only spacecraft 3 retains a working CIS instrument. Therefore, on the basis of the previously described criteria, only the event as seen by spacecraft 3 was suitable for analysis.

Boundary normal analysis for spacecraft 3 was somewhat simplified by the presence of periods before and after the crossing that showed high stability in terms of magnetic field components. This gave the advantage of being able to use the Tangential Discontinuity and both Minimum Variance Analysis methods with comparative confidence in the accuracy of the result.

Method	∇	$\langle B_N \rangle$	Variance (σ_{B_N})
Tangential Discontinuity	0.01	-0.25	9.80
MVA	0.03	-1.07	10.02
MVAB	0.04	0.45	10.58

Table 3.12: A comparison of gradient, average normal magnetic field component magnitude and variance for all four boundary normal vector determination methods for spacecraft 3 over the feature at ≈02:35 UT on 1st April 2003.

The results in Table 3.12 show that, in this case, the tangential discontinuity method provided the highest coherence with the predefined criteria. This is likely due to the almost anti-parallel ($\approx 140°$) nature of the magnetic fields on either side of the transition layer in the frame of that layer. The calculated normal vectors for all three spacecraft are presented in Table 3.13. The distribution of vectors shows significantly more variance than would usually be the case, this is a reflection of the highly variable nature of the magnetic field vectors in the pre-transition region and, the incomplete nature of the crossings of spacecrafts 1 and 4.

SPC	Time (UT)	N_X	N_Y	N_Z
1	02:35:30	0.7402 ± 0.0182	-0.6615 ± 0.0194	-0.1210 ± 0.0325
2	02:36:20	0.6024 ± 0.0527	0.0838 ± 0.0781	0.7938 ± 0.0529
3	02:36:20	0.7879 ± 0.0054	0.5679 ± 0.0090	0.2382 ± 0.0216
4	02:35:45	0.6145 ± 0.0517	0.6123 ± 0.0457	0.4976 ± 0.0675

Table 3.13: A summary of the boundary normal vectors for the 4 spacecraft during the interaction with the magnetopause transition layer at ≈ 02:35UT.

When the data is translated into the boundary normal frame both B_N and V_N fall to almost zero. The reorientation of field and flow quantities is therefore primarily tangential. The component of the bulk flow velocity that is tangential to the boundary drops significantly from ≈675km/s to ≈163km/s, a reduction of over 75%.

de Hoffmann-Teller (dHT) analysis was carried out over an interval spanning the crossing for spacecraft 3 using CIS-HIA data. The results showed a high degree of coherence with the criterion describing a well defined convective frame, the gradient of the linear regression applied was ≈1.00, the correlation coefficient was high at ≈0.99 and the electric field residual factor (D/D_0) was ≈0.02, i.e.

the calculated electric field within the defined dHT frame after galilean transformation was 2% of its original value. The transformation velocity calculated was $\mathbf{V}_{HT}(L, M, N) \approx (363, -303, -69)$. The normal component of $\mathbf{V}_{HT}$ is small in comparison to the tangential component and is of similar order to other calculated values at this time, the negative sign suggests an earthward directed movement which may have contributed to the variability of the measured variables during the crossing. Using this value for the dHT velocity the transition region was examined for local coherence with the predictions of the Walèn relation, the results of this are in Figure 3.23.

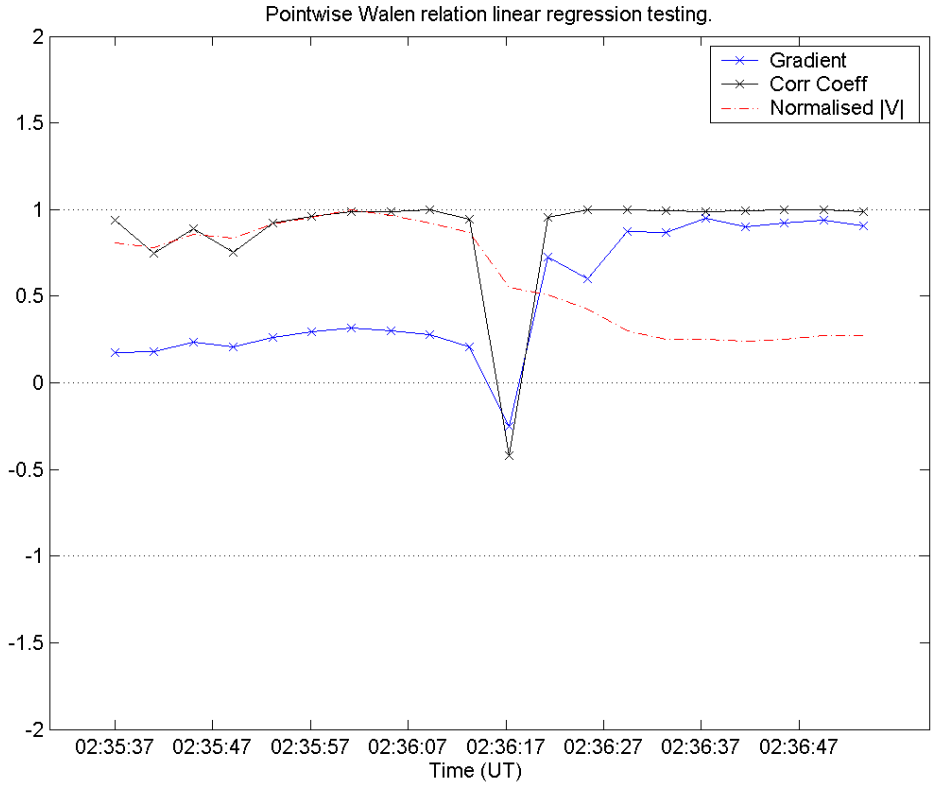

Figure 3.23: The results of a pointwise scan across the transition interval at 02:36:20 using spacecraft 3 CIS-HIA data to test against the predictions made by the Walèn relation.

The time series shows an interesting mix of behaviour that can be divided into three distinct periods. The immediate pre-transition period evidences a consistently high correlation coefficient suggesting that there is a field aligned flow in the frame defined by the previously calculated de Hoffmann-Teller velocity. The gradient at

this time is also consistent in value but is significantly less than the unity value expected for Alfvénic acceleration, this is as expected as there is no suggestion in the velocity data that the spacecraft is interacting with the layer at this time. This period finishes exactly at the edge of the region where the bulk velocity changes. The first data point within the transition region itself evidences a complete reversal of orientation. Both the correlation coefficient and gradient are now negative. This period is, however, so short that it is unlikely that this behaviour is consistent with respect to time, i.e. the local conditions are changing quickly enough that the instrumental determination of the spin averaged fluid properties is unlikely to be entirely representative. Following this reversal the flow seems to return to its original orientation, with respect to the field direction, but this time although the correlation coefficient is similar at unity, the gradient increases to between 0.60 and 0.73. This indicates greater evidence of a driven flow that might be associated with either Alfvénic or slow mode shock based acceleration mechanics.

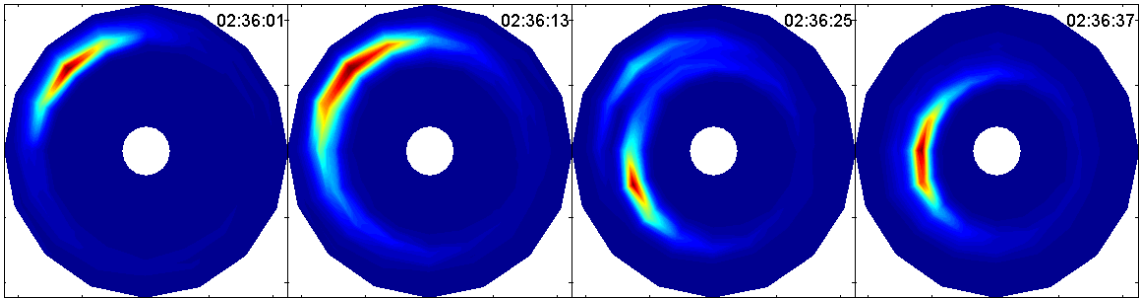

Figure 3.24: The omnipolar, azimuthal energy spectrograms for the CIS-HIA instrument, collected during the transition at 02:35 UT by spacecraft 3 on 1st April 2003. They qualitatively illustrate the coherence of the particle population across the transition. The axes used in each image are the same as those described in Figure 3.10.

Looking at the omni-polar azimuthal energy distributions presented in Figure 3.24 a high degree of distribution coherence across the transition can be seen. The change from the higher energy pre-crossing distribution to post-crossing lower energy distribution is comparatively clean with little evidence of distribution smearing or indistinctness. As such it is possible to say that the single fluid MHD approach is likely applicable in this case.

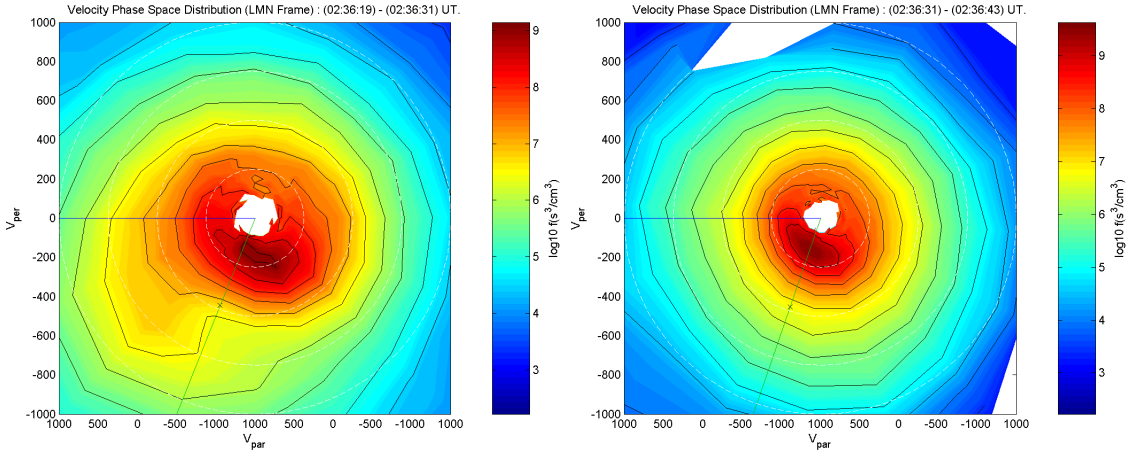

Figure 3.25: Velocity phase space diagrams showing consecutive sampling times across the transition created from spacecraft 3 CIS-HIA data. The coordinate system for both images has been transformed into the boundary normal frame. The normal vector calculated for the magnetopause at this time is plotted (blue line) along with the calculated deHoffmann-Teller velocity (green line).

Examining the velocity phase space data from the CIS-HIA instrument for this time (Figure 3.25) it is immediately apparent that there is plasma flow from both of these local regimes across this boundary. If the distribution with respect to the dHT velocity is considered, in a) we see that there is a large component that is flowing into the magnetopause (-VE V_N) and a smaller, high energy either flowing out or being reflected (+VE V_N), this data was collected almost entirely during the crossing however due to the long sampling time it is a possibility that this second component is a remnant of the plasma in the previous region. In the second, later frame, the spacecraft has passed through the transition layer itself and is now again in a relatively settled region. The flow is now almost perfectly aligned with the dHT velocity. This is evidence that there was a convecting quasi-static structure at this location.

The initial boundary value sets required for the reconnection layer simulation were created using data from two stable periods, one before and one after the transition layer. The timing of these periods and the values derived from them can be seen in Table 3.14.

The structural constants from this simulation clearly define the constructed

Pre-Layer Components. Taken from 02:35:36 to 02:35:52			
Variable	Value	Absolute Statistical Error	Percentage Error
$B_L(nT)$	-0.7332	1.38	3.66
$B_M(nT)$	-37.8204	1.38	3.64
$V_L(km/s)$	291.8898	14.45	2.56
$V_M(km/s)$	-483.9956	20.21	3.57
$N(/cm^3)$	1.0455	0.04	0.01
$T(10^6K)$	18.1991	0.25	0.04
Post-Layer Components. Taken from 02:36:30 to 02:36:50			
Variable	Value	Absolute Statistical Error	Percentage Error
$B_L(nT)$	-23.8564	1.64	4.42
$B_M(nT)$	28.4691	1.01	2.72
$V_L(km/s)$	141.5806	7.26	4.39
$V_M(km/s)$	-85.6353	4.40	2.66
$N(/cm^3)$	5.7044	0.33	0.20
$T(10^6K)$	2.5538	0.20	0.12

Table 3.14: Initial boundary values input into the reconnection layer model.

model as being of the Region II (ASCSA) type. η and $\tilde{\eta}$ (defined in 2.5.2) were 0.50 and 0.51 for the magnetopause and magnetosheath sides respectively. Both values are significantly below unity and as such clearly describe slow shocks, rather than slow expansion fans, in the constructed model. The coplanarity factor $|\mathbf{b}|$ is calculated to have a value of 787.03, the upper limit of Region II is 807.96. Lying between 0 and this upper limit also confirms this structure type. The coplanarity factor is, however, near the upper limit and so might lead to a situation where the slow shock on the side with the lower magnetic strength disappears. Considering this, the initial pass model (Figure 3.26) fits well. The initial timings were based on different variable sets depending on type and where the appropriate variations were most clearly seen. The position of the bounding Alfvén waves were, in this case, linked to the bulk velocity data as that is where the changes are most noticeable. The times of the slow mode waves comprising the next layer towards the centre were specified by the significant changes in the magnetic field, most notably the field magnitude. Since the contact discontinuity only affects the number density and temperature, it was those variables that were used to choose its location. There is a significant divergence quantitatively in these variables, however, qualitative behaviour could still be used. The degree of coherence is generally good. There is, as

usual, significantly better agreement between model and data in the magnetic field variables than in the plasma variables. This is as expected as the model does not carry as many simplifications that apply to the magnetic field, as opposed to the now single fluid single species plasma. Further analysis of this event in terms of this model is continued in §4.1.1, where the analysis through the genetic algorithms is presented.

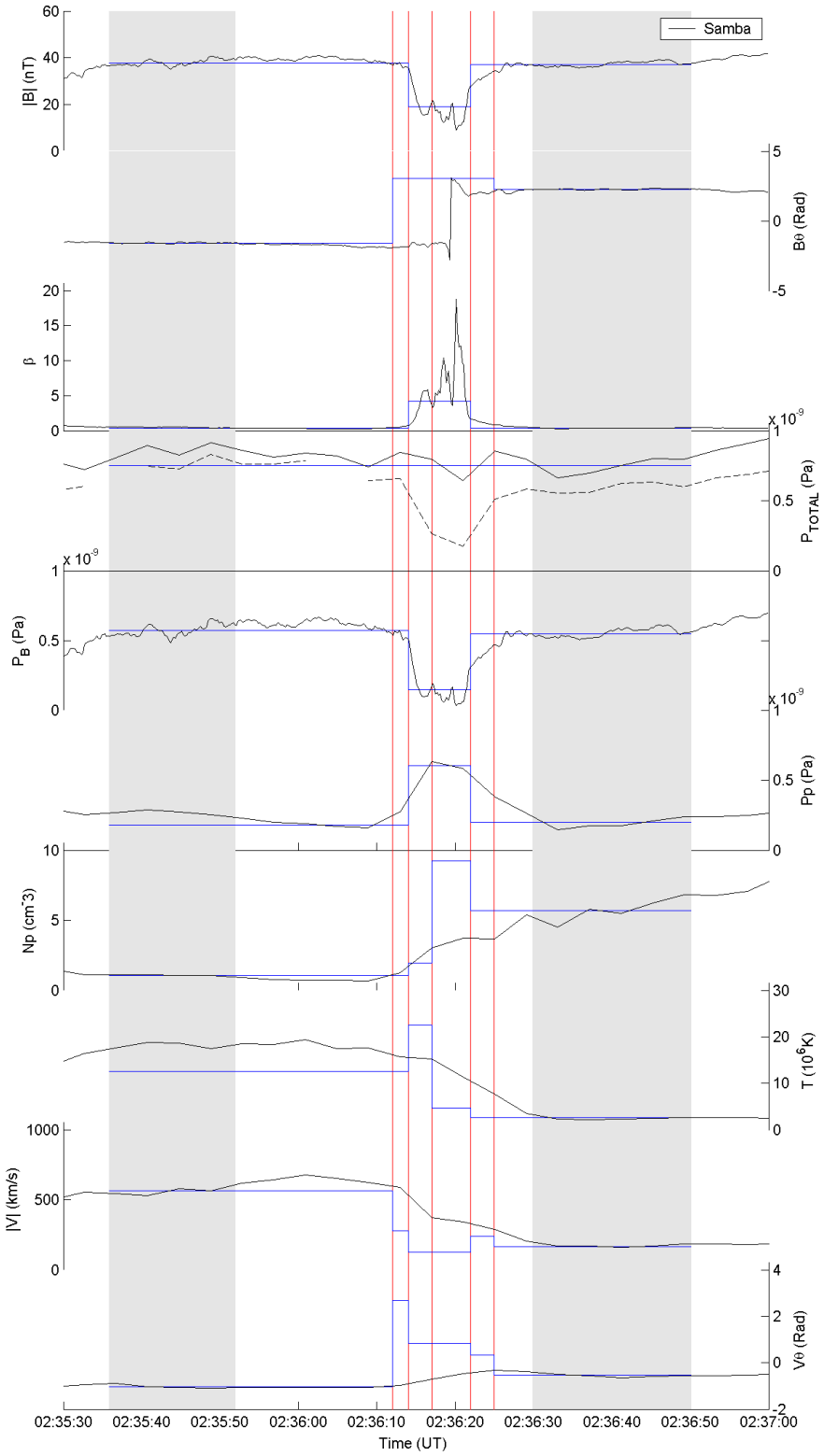

Figure 3.26: Comparative overlay of the reconnection layer model for April 1st 2003 at 02:35 UT created by the simulation using the initial conditions previously defined for all magnetic and plasma variables from spacecraft 3 data. Observed data is presented in black, modelled in blue, the discontinuities are marked by red vertical lines and the ranges used for boundary condition sampling are shown in grey.

3.3 STRUCTURE TYPE III : (ARCSA), 3rd December 2001

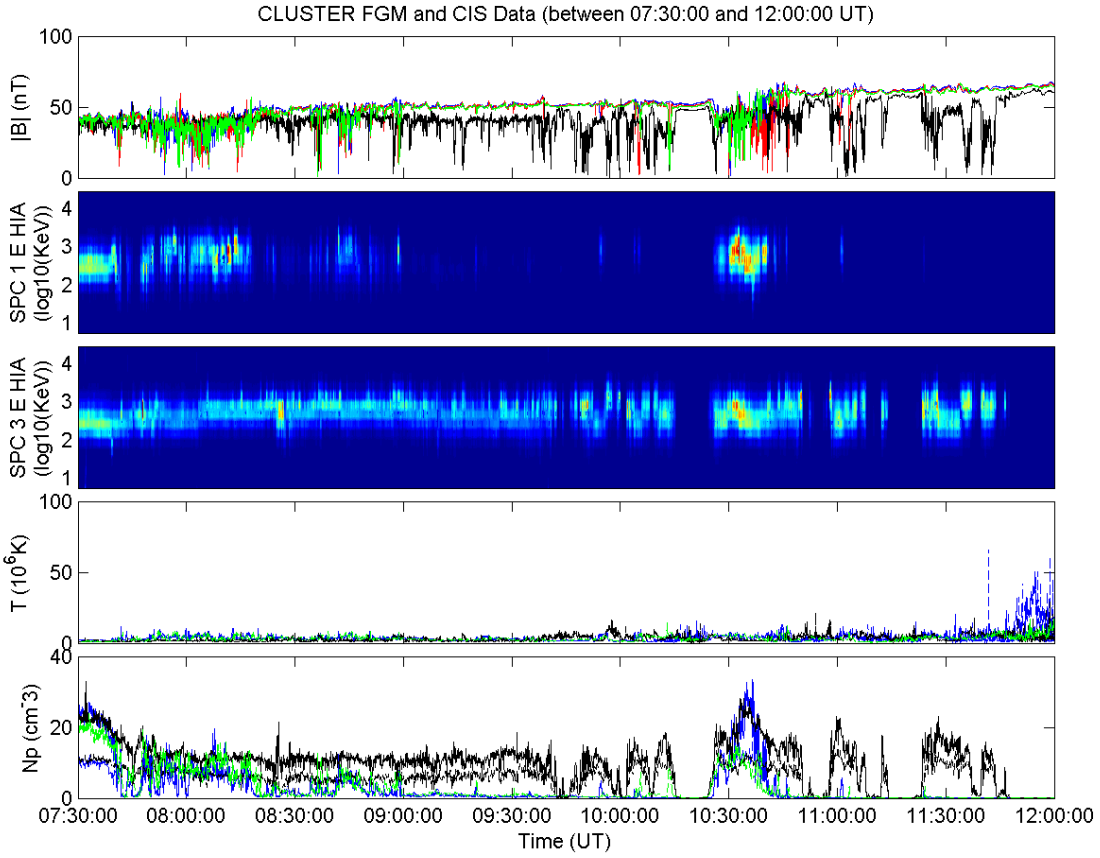

Figure 3.27: An overview of all spacecraft data for magnetic field strength, temperature and number density with attendant energy spectrograms for the CIS HIA instruments on spacecrafts 1 and 3 to highlight the differential behaviour between the two.

On this date the Cluster spacecraft were on an out-bound pass out of the magnetosphere. The transit was located in the southern duskside magnetopause. As can be seen from the second diagram in Figure 3.28 the constellation reaches apogee and begins transit back towards earth during this period.

This event consisted of multiple crossings of the duskside magnetopause over the course of several hours from ≈7:30-12:00 UT. It was discussed in terms of the presence of continuous reconnection by Retinò et al. (2005) in the context of providing reasonable evidence for reconnection having been prolonged and active at this location over the 3 hour period of the study.

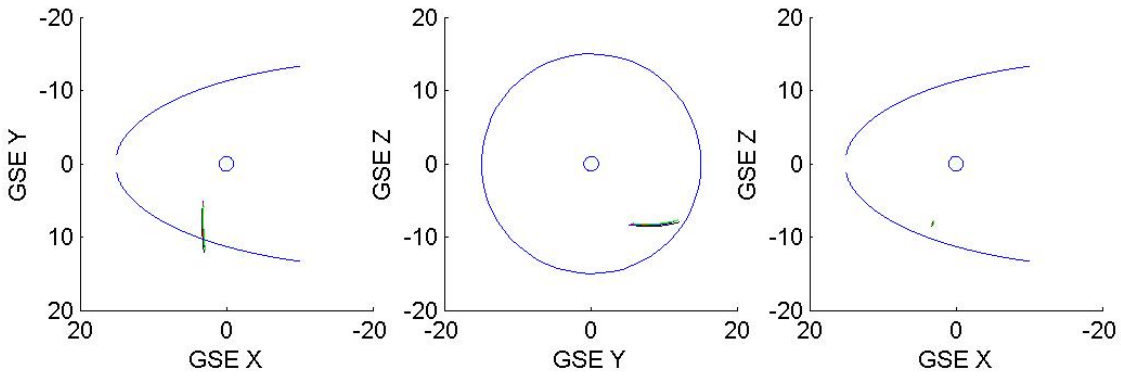

Figure 3.28: A diagram of spacecraft position from 07:30 to 12:30 UT on 3rd December 2001 against a model magnetopause produced using Sibeck et al. (1991).

During this period the data recorded by the different spacecraft evidenced significantly different behaviour patterns both morphologically and quantitatively. The arrangement of spacecraft during this period was such that during the period of interest the spacecraft separation was between ≈2000km - 6700km. Spacecrafts 1, 2 & 3 began the interval in a fairly close semi-linear grouping set significantly further from the earth than spacecraft 4. This grouping changed during the later stages of observation as spacecrafts 1 & 3 moved near to spacecraft 4, leaving spacecraft 3 at a greater distance. These structural groupings do seem to be reflected in the data collected.

3.3.1 Pre-simulation Analysis

During the period highlighted by Retinò et al. (2005) from 07:30 to 12:00 UT there are multiple transits of the magnetopause by the CLUSTER group. As may be seen from Figure 3.27, the transition behaviour can be clearly separated into two distinct groups: Spacecrafts 1,2 and 4 in one group and spacecraft 3 in the other.

While the former group remain, for the most part, within the magnetosheath during this period with infrequent transitions spacecraft 3 retained a continuous presence within the magnetopause boundary layer and underwent continuous transitions of the magnetopause boundary during the whole of this period. To a degree it is the continuous nature of this sampling of the magnetopause that allowed Retinò

et al to make their case for the observation of continuous reconnection.

As such each crossing event was then analysed, in both behavioural groups, from multiple bases. Primarily analysis was carried out on each event essentially in vacuo, treating it as a single spacecraft event with no wider context. Secondary analysis then built on this and attempted to establish behaviour and structure in terms of the spacecraft functioning as a coherent case group.

3.3.2 Non-simulation Events

Several crossing signatures are present before the primary ones listed in the paper. These signatures are defined as significant perturbations to both the magnetic field direction and magnitude in concert with changes to number density, bulk velocity and temperature.

These events are, for the most part, either partial crossings, single spacecraft crossings or are in some other way unsuitable for simulation during this study. They are, however, useful for testing for the extended nature of the reconnection behaviour during this period with the fluid and particle testing methods previously described (de Hoffmann-Teller analysis in §2.2, Tangential Stress Balance testing in §2.3 and distribution function analysis).

The period of interest seems to be divisible into two distinct subsections. For group I there are periods of significant transition activity between 07:30 and 09:00 UT and from 09:45 until 11:15 UT. Group II (spacecraft 3) shows a shorter initial period from 07:30 to 08:00 UT but the latter period is significantly longer from 09:30 to 12:00 UT.

The earliest and clearest of these events occurs at approximately 07:41 UT. Signatures for this crossing are present in the data of every one of the CLUSTER spacecraft. They are, however, much stronger in the group I data than group II. Spacecraft 3 is further sunward than the others and as such the transitions may either be incomplete or continuous whereas those encountered by the other spacecraft are complete and therefore highly visible.

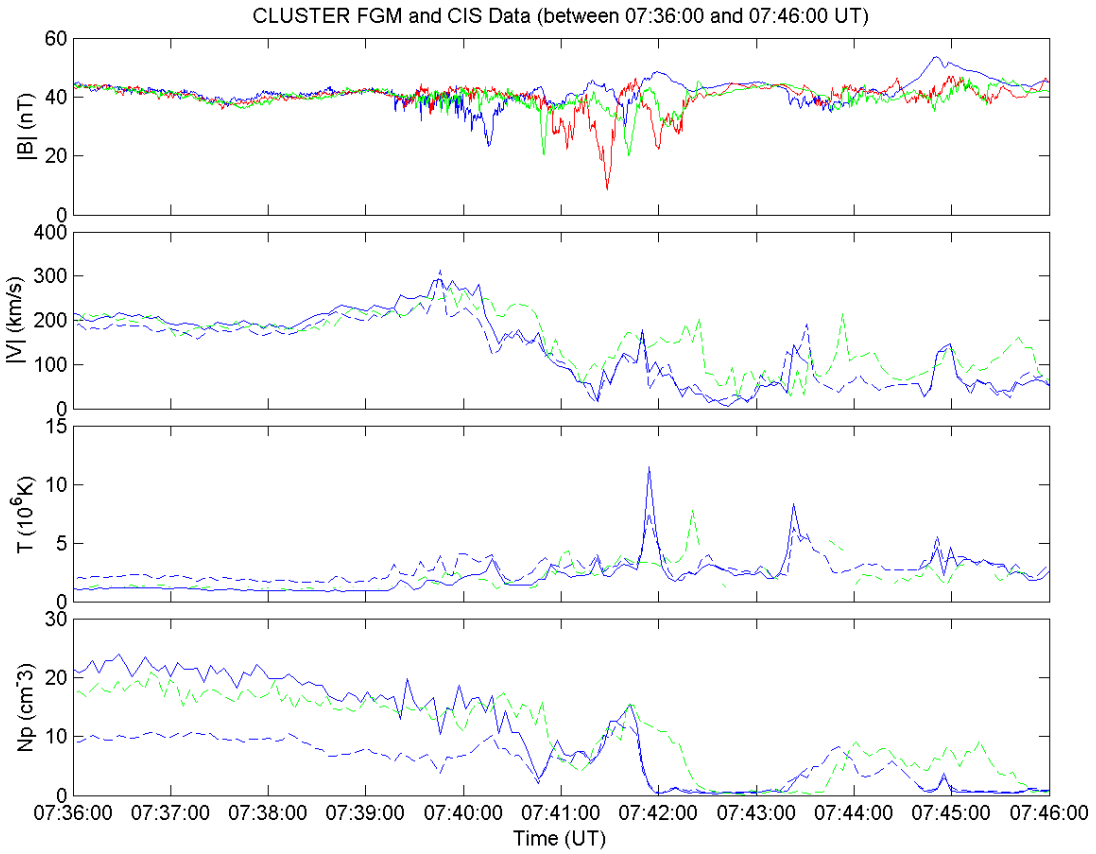

Figure 3.29: An overview of the parameters of spacecrafts 1 (blue). 2 (red) and 3(green) over the non-simulation crossing at 07:40 UT. Spacecraft 3 is not shown as it did not interact with the magnetopause during this period.

The crossing itself, as evidenced by rotation of magnetic field vectors, takes place at slightly different times for each spacecraft. These times are recorded in Table 3.15. All times are given in UT.

SPC	Start Rotation	End Rotation	Rotation Centre
Rumba (1)	07:40:12	07:40:20	07:40:16
Samba (2)	07:40:53	07:41:03	07:40:58
Salsa (3)	07:42:34	07:43:30	07:43:06.5
Tango (4)	07:40:47	07:40:52	07:40:49.5

Table 3.15: An example illustrating the different times (UT) that all 4 spacecraft crossed the magnetopause boundary that are categorised as a single event occurring at 07:41 UT on 3rd December 2001.

These distinct periods were each subjected to boundary normal analysis separately. In this case tangential discontinuity vectors were calculated from the averaged data between 07:37:00 and 07:38:00 UT before the event and 07:42:30 to 07:43:00 UT after it. In the same fashion the minimum variance analysis was conducted

over multiple expanding ranges to be certain of the method not being susceptible to selection bias. As can be seen from this figure, the B_N constrained minimum variance analysis method (MVAB) provides a frame that evidences significantly less variance during the transition period.

Spacecraft 1, 2 and 4 all showed strong evidence of crossing this boundary at about the same time whereas the magnetic field rotation signatures are much weaker for spacecraft 3. The completed boundary normal analysis gave the results of which are in Table 3.16.

SPC	X_{GSE}	Y_{GSE}	Z_{GSE}	θ	ϕ
1	0.7189	0.4615	-0.5198	32.6964	-31.3201
2	0.7648	0.4862	-0.4227	32.4424	-25.0059
3	0.7083	0.4860	-0.5120	34.4590	-30.7942
4	0.7404	0.5580	-0.3748	37.0039	-22.0128
Model	0.6467	0.6286	-0.4320	44.1846	-25.5951

Table 3.16: Boundary normal coordinate values for the multi-spacecraft transition across the magnetopause at 07:41 UT on December 3rd 2001.

There is significant agreement between these values. They provide a mean normal magnetic field magnitude of $\approx$ 2nT in the positive normal (sunward direction) for spacecrafts 2 & 4 which all had strong signatures but $\approx$-2nT for spacecrafts 1 & 3. These vectors are also consistent in terms of the orientation with respect to the model magnetopause.

The data, after being translated into a coordinate frame defined by the normal vector for each spacecraft, was subject to de Hoffmann-Teller analysis. The consequent de Hoffmann Teller frame velocities and quality factors from the linear regression applied are presented in Table 3.17, the scatter plots themselves showing the fitted relations are in Figure 3.30.

The results in Table 3.17 show a high degree of agreement between the two spacecraft sets. In both bases the correlation coefficients are above 0.96 and the reduction in convection electric field is between 93- 96%. This suggests that in both cases a well defined frame has been calculated. The analysis also shows that the boundary is quasi-stationary as the calculated values for V_{HTN} are only -15km/s

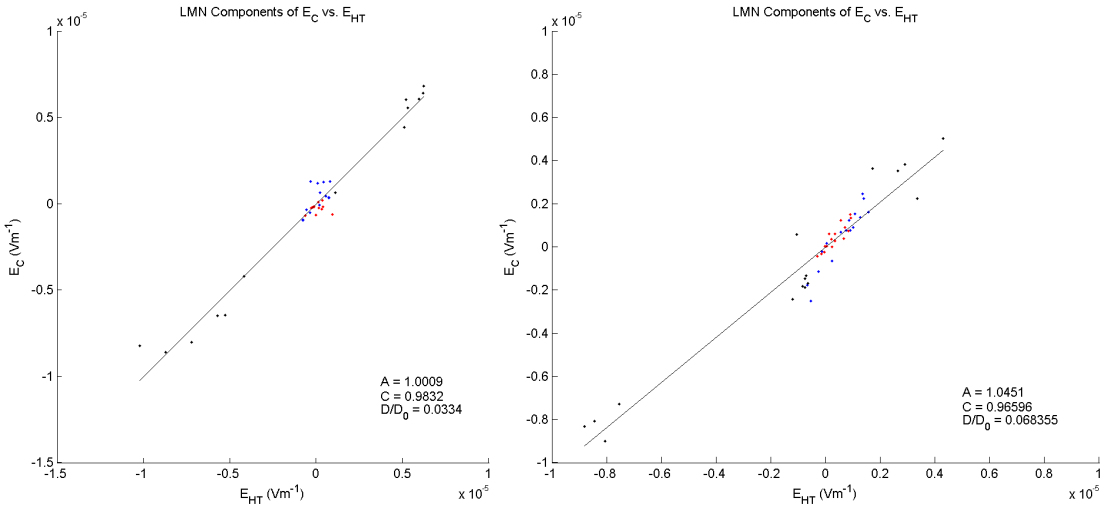

Figure 3.30: Linear regression scatter plots produced during the de Hoffmann-Teller analysis carried out for spacecrafts 1 (left) and 4 (right) between 07:38:00 and 07:42:30 UT on 3rd December 2001.

SPC	V_{HTX}	V_{HTY}	V_{HTZ}	∇	C	$D/D0$
1	146.18	-234.75	-15.49	1.00	0.98	0.03
4	129.15	-185.13	9.10	1.05	0.97	0.07

Table 3.17: de Hoffmann-Teller analysis velocities and regression values for spacecrafts 1 and 4 indicating similarity of structure while highlighting possible differences in local conditions.

and 9km/s for spacecrafts 1 & 4 respectively.

Walèn Analysis, when applied to spacecraft 1, between the bounds of the transition gave the result that the linear fit gradient is -0.91 with a correlation coefficient of -0.98, these results are plotted in Figure 3.31.

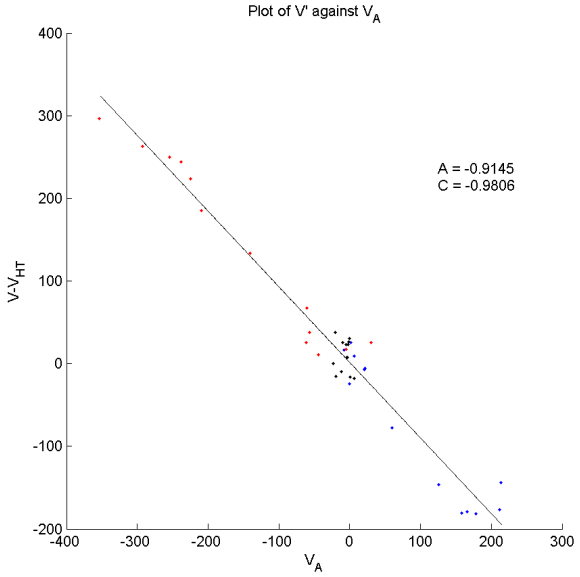

Figure 3.31: Tangential Stress Balance (Walèn relation) linear regression analysis for spacecraft 1 on 3rd December 2001 at 07:40 UT.

The same analysis applied to the spacecraft 4 data does not give the same degree of cohesion with a gradient of -0.33 but a correlation coefficient of -0.59. This would suggest that the feature described is not, at this time, field aligned or Alfvénically driven.

These results would suggest that this transition layer contains a quasi-static structure and that that structure is well described as being field aligned and convects in relation to the local Alfvén speed. Both of these are indicators of the presence of reconnection. The negative gradient and correlation coefficient suggest that BN +VE across the transition i.e. is the spacecraft is passing southward of the reconnection diffusion region. This confirms the sign of the mean value calculated at the point of boundary normal determination.

Further crossings at later times offer similar information. For brevity only the first 3 cases where all 4 spacecraft interacted with the layer will be reproduced and

Time (UT)	N_X	N_Y	N_Z	SPC
07:47:30	0.6854 ± 0.0122	0.4515 ± 0.0124	-0.5713 ± 0.0137	1
	0.7219 ± 0.0077	0.4891 ± 0.0056	-0.4895 ± 0.0098	2
	0.6318 ± 0.0084	0.6104 ± 0.0080	-0.4778 ± 0.0060	3
	0.7111 ± 0.0071	0.4836 ± 0.0040	-0.5102 ± 0.0103	4
07:49:00	0.6191 ± 0.0103	0.5506 ± 0.0081	-0.5600 ± 0.0140	1
	0.6782 ± 0.0087	0.5546 ± 0.0070	-0.4820 ± 0.0103	2
	0.5643 ± 0.0117	0.6000 ± 0.0097	-0.5669 ± 0.0132	3
	0.6588 ± 0.0106	0.5390 ± 0.0082	-0.5248 ± 0.0135	4
07:51:30	0.5496 ± 0.0561	0.4959 ± 0.0353	-0.6723 ± 0.0719	2
	0.7879 ± 0.0397	0.5766 ± 0.0110	-0.2163 ± 0.1537	4

Table 3.18: Compiled boundary normal data for magnetopause interactions of 3 sample non-simulation events sorted by the time they crossed the transition layer.

in those cases only the times of these interactions and their calculated normal vector components will be listed in Table 3.18.

Drawing this information together there is, within experimental and methodological accuracies, a high degree of agreement between the different events and between different spacecraft within each transition event. The direction of the boundary normal vector varies but this may be due to the presence of local perturbations such as surface waves that are beyond the scope of this work.

The presence of well defined dHT frames and some evidence for bulk velocity behaviour in agreement with the Tangential Stress Balance (Walèn) relation provides fluid evidence for the presence of reconnection related flows and structures at these locations at these times.

Particle evidence for the presence of reconnection comes in the form of specific structures visible in the velocity phase space distribution.

Looking for the characteristic D-shaped structures in the velocity phase-space distributions recorded by the two CIS-HIA instruments during each crossing we find that the structures are present in many of the distributions at approximately the same time as perturbations in the bulk flow velocity which might suggest reconnection as the causal factor for these modifications. A clear example of one of these occasions is shown in Figure 3.32.

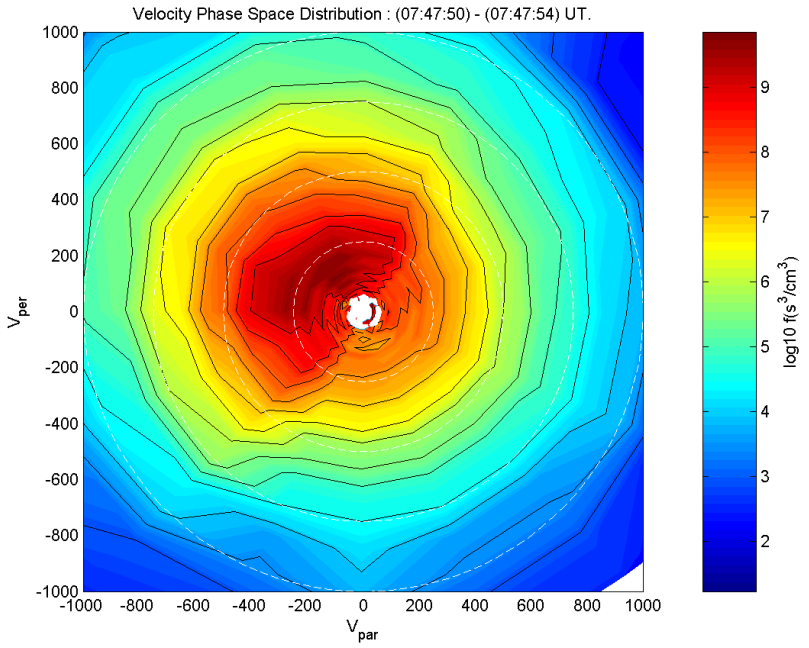

Figure 3.32: The phase space velocity distribution of ions during the first crossing present in Table 3.18 for spacecraft 3. The expected D-shaped distribution denoting a reconnection process is clearly present near the origin in the -ve $V_{\parallel}$, +ve $V_{\perp}$ quadrant.

3.3.3 Simulation Analysis

The two events written up as primary events and subjected to the most extensive analysis in the original paper were those at 10:50 and 10:58 and were observed, primarily, by spacecraft 3.

Event 1: 10:50UT

Spacecraft 1 crosses the transition layer some minutes before this time, as can be seen from the summary Figure 3.33. If, as Retinò et al. suggest, reconnection is continuous then if the spatial extent of the feature is greater than the average separation during this period of about 4000km it too should sample this reconnection region. Considering the nature of the length scales associated with the reconnection process itself, in addition to the continuous transport of reconnected flux tubes anti-sunwards this is a reasonable expectation.

In Figure 3.34(a) it can be seen that the transition from the magnetosphere

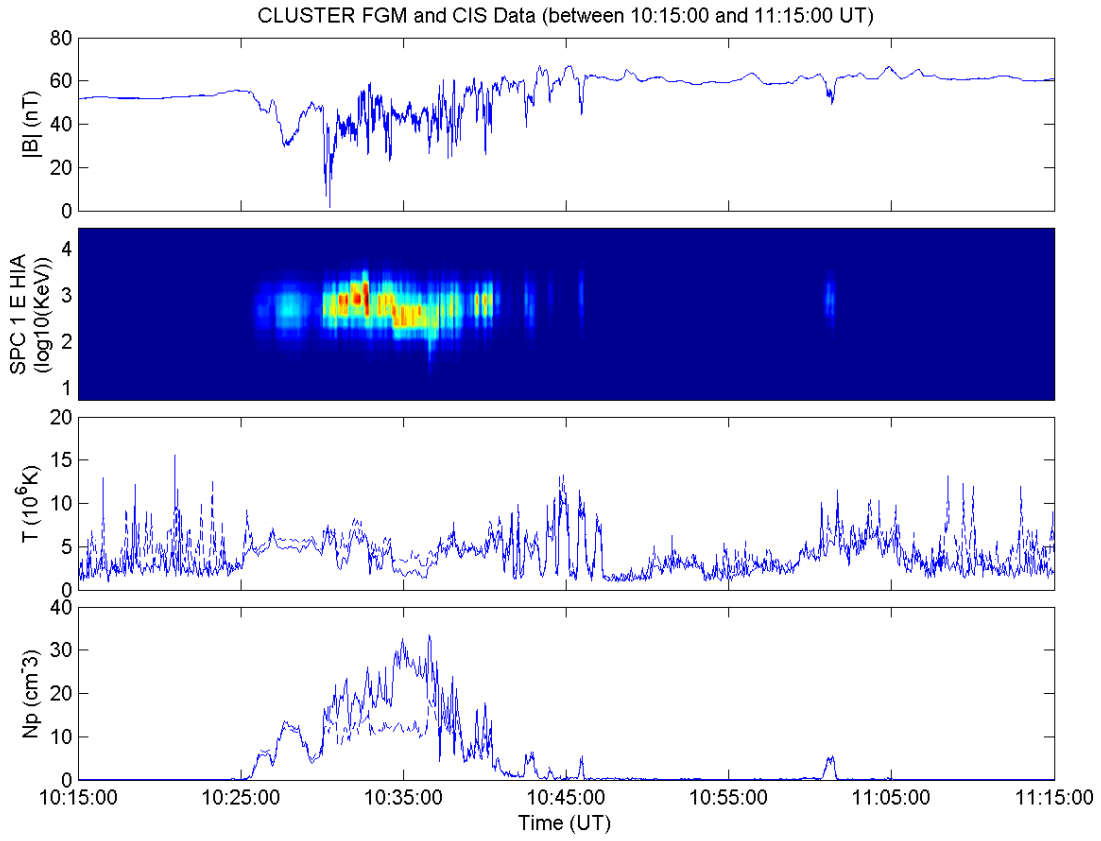

Figure 3.33: An overview of the primary period of interest showing a comparatively complete magnetopause transition for spacecraft 1 including CIS HIA spectrograms.

into the magnetosheath begins at 10:25 UT and the activity continues until 10:45 UT. Significant changes to magnetic field strength and orientation are clear and are temporally coincident with changes in associated plasma variables quantities.

Looking at these features as a whole it seems that; either the reconnection rate was fluctuating and the spacecraft sampled different sections of the progression or that the feature was quasi-static in time but different spatial locations were interacted with.

For spacecrafts 1, 2 and 4 the interaction with the layer does not seem to have been as prolonged as was the case for spacecraft 3. However there are several features we can pick out and analyse. The most striking of these, initially, is that of the bulk velocity enhancement that can be seen at approximately 10:58 UT in Figure 3.34(b). These seem to be echoed in all data sets (for which ion data is available) and will be explored further in the event following this one.

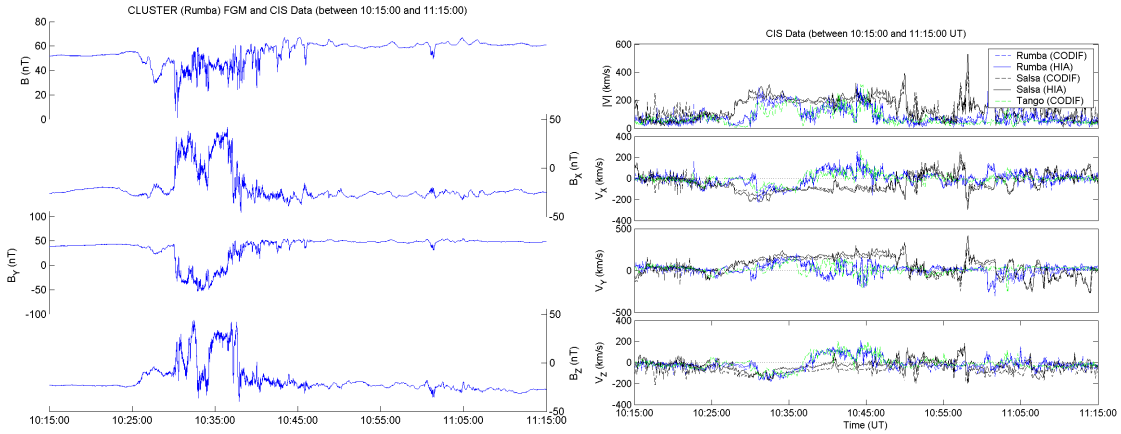

(a) Magnetic field data for Spacecraft 1 (Rumba) over the period of interest on the 3rd of December 2001. Obvious disturbances between 10:25 and 10:45 UT herald interactions with the magnetopause.

(b) Velocity data for all spacecraft, plotting HIA data from Spacecrafts 1 and 3 and CODIF data from spacecraft 4. All data is currently in the GSE coordinate system.

Figure 3.34: Plasma parameter quantities taken across the period of interest for Spacecraft 1 (a) and Spacecrafts 1,3 & 4 (b)

Spacecraft 3, during this period, undergoes 6 complete crossings, including those highlighted in the paper. Each of these crossings have been used to attempt to calculate both normal vectors and tested for the fluid signatures of reconnection. Figure 3.35 shows an observational overview of the data collected during this period.

In the first primary case the spacecraft entered a period of transition, as can be seen in Figure 3.35, at approximately 10:25:00 UT where it passed out of the magnetosphere and into the magnetosheath, leading to a rise in density and a decrease in total magnetic field magnitude. The boundary normal for the crossing was calculated to be GSE(x,y,z)=(0.8761±0.0018, 0.3048±0.0047, 0.3735±0.0076) or $(R, \theta, \phi) \approx (1, 19°, -22°)$ which is in broad agreement with earlier calculations and the model normal for that spatial location. The data, when transformed into this frame shows both magnetic field and bulk flow rotation, enhancements and other possible features of reconnection. A significant feature at approximately 10:25:30-10:26:20 UT describes a large ($\approx 50\%$) decrease in magnetic field magnitude with little evidence of rotation, a modest acceleration and rotation of the bulk flow velocity ($\Delta V \approx 600 km/s$, $\Delta V_\phi \approx 100°$) and peaks in both number density and temperature. Available EFW electric field data at this time was incomplete and so direct

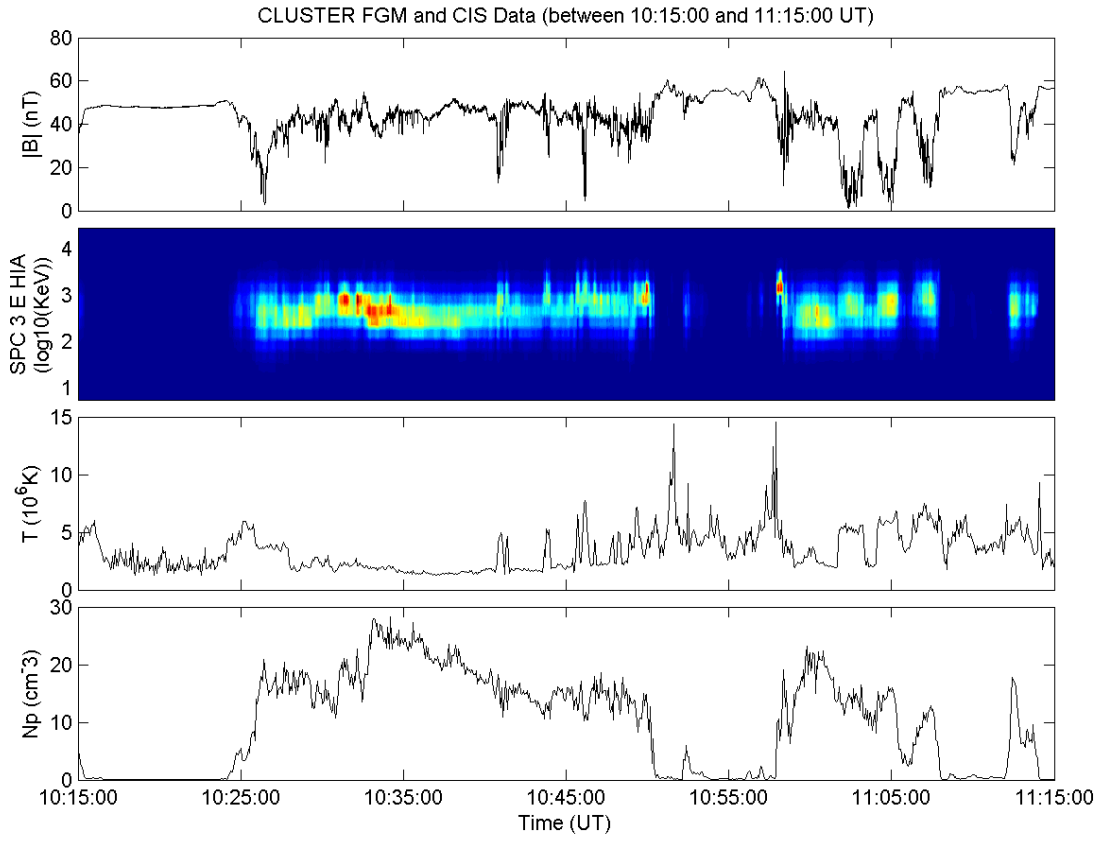

Figure 3.35: Event overview for SPC 3 over the interval of study, 10:15 to 11:15 UT, on 3rd December 2001. The plasma parameter and spectrogram data presented are those collected by the CIS-HIA instrument.

use in de Hoffmann-Teller analysis is impossible. Using the frozen-in-condition to derive the convective electric field dHT analysis was carried out over three specific features in the bulk velocity data; at 10:24:30, 10:25:30 and 10:27:30 UT. Corroborating answers from all three features would suggest the presence of a well defined convecting structure that all three were either a part of or connected to. The results of these analyses are in Table 3.19.

Time (UT)	V_{HT_L}	V_{HT_M}	V_{HT_N}	∇	C	D/D_0
10:24:30	-54.40	-2.51	-69.11	1.00	0.97	0.06
10:25:30	-8.58	-19.40	-69.56	1.02	0.82	0.28
10:27:30	-32.38	-37.43	-31.11	1.33	0.74	0.49

Table 3.19: de Hoffmann-Teller fram velocity (km/s) results from consequent samples of crossing at 10:25 UT on the 3rd of December 2001, each comprising approximately one minute of data.

From these results it is fairly obvious that as the layer is traversed the coherence

of the convective frame decreases. The magnetopause normal velocity is the same, to within experimental error, in the first two cases. The spacecraft velocity normal to the boundary during this time, in the boundary normal frame, is comparatively very similar to these values at -66km/s. This might suggest that the boundary is comoving with the spacecraft, although it is unlikely to be doing so steadily.

Taking the region over which there is a good dHT frame described, the tangential stress balance relation gives a negative result with a correlation coefficient of only 0.40. One reason for this may be the presence of a comparatively strong magnetic field component in the M-axis of -45nT, pointing in the duskward direction.

The second complete crossing occurred from 10:48:45 to 10:50:30 UT, during which time the spacecraft performed a completed inbound crossing, between approximately 10:49:50 and 10:50:30 UT, coincident with changes a marked decrease in density, increase in temperature and magnetic field direction.

The selected boundary normal vector for this crossing was calculated using the Tangential Discontinuity Method (§2.1.2) and was GSE(x,y,z)=(0.7523±0.0037, 0.2626±0.0067, -0.6042±0.0062). The magnetic field and ion data were transformed into the frame defined by these axes and the resultant data was subject to de Hoffmann - Teller analysis over the length of the obvious interaction with the magnetopause (10:49:41 - 10:50:30 UT). The results, for both CIS instruments, are collected in Table 3.20 below. The continued low value of V_{HT_N} corroborates earlier evidence that the magnetopause was moving outward at comparatively low speeds, this quasi-stationarity may assist with the application of the other analysis methods. The regression coefficients for this analysis were suggestive of there being a well defined static frame, both CIS instruments exhibited high correlation coefficients (0.99 & 0.96 for CODIF and HIA respectively) in addition to the degree of reduction in the convective electric field (99% & 93%) in comparison to its original value.

The crossing is less than smooth (Figure 3.36) and the changes in plasma parameters suggest magnetopause movement over the spacecraft. To this end the Walèn test results have proven more complicated during testing. Because of this the Walèn

CIS	V_{HT_L} (km/s)	V_{HT_M} (km/s)	V_{HT_N} (km/s)	∇	C	D/D_0
CODIF	-107.55	-249.61	18.96	1.00	0.99	0.01
HIA	-32.25	-349.91	6.00	1.01	0.96	0.07

Table 3.20: dHT results from both CIS instruments using data recorded by spacecraft 3 during the transition at ≈10:50 UT on the 3rd of December 2001.

test was only applied over the region where significant velocity perturbations were present, from 10:49:57 to 10:50:30 UT. The calculated correlation coefficient was -0.99 and a gradient of -0.30. This would therefore suggest that this acceleration took place in a quasi-static structure, but that it was unlikely to be Alfvénic in nature as $\nabla \ll 1$. Particle phase-space distributions also show a possible but imperfect D-shaped distribution in the data sampled between 10:49:54 and 10:50:06 UT. This time period encapsulates the initial period of acceleration.

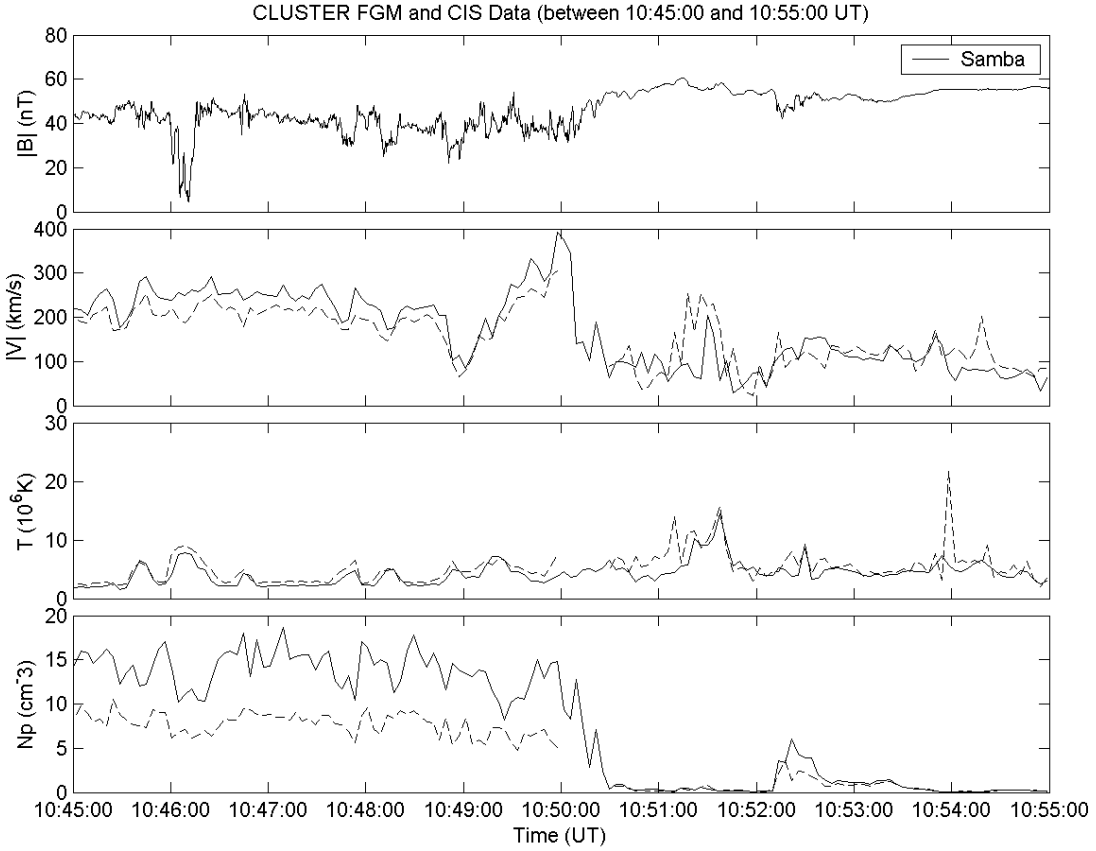

Figure 3.36: Plasma parameter overview for the crossing of spacecraft 3 at ≈ 10:50 UT on the 3rd of December 2001.

The model is dependent on the use of single plasma parameters to describe the behaviour of the reconnection layer. To examine the validity of assigning a single

state variable value to the distribution during this time the particle distribution functions were scrutinised as described in §2.4.

Figure 3.37 shows the CIS HIA distribution functions in their entirety for spacecraft 3. The 8 images represent each of the polar bin angles present in the archive data, the angle of inclination to the spacecraft equatorial plane is given in degrees in the top-right of each frame. The radial coordinate denotes the base 10 logarithm of the energy distribution and the angular data is unmodified.

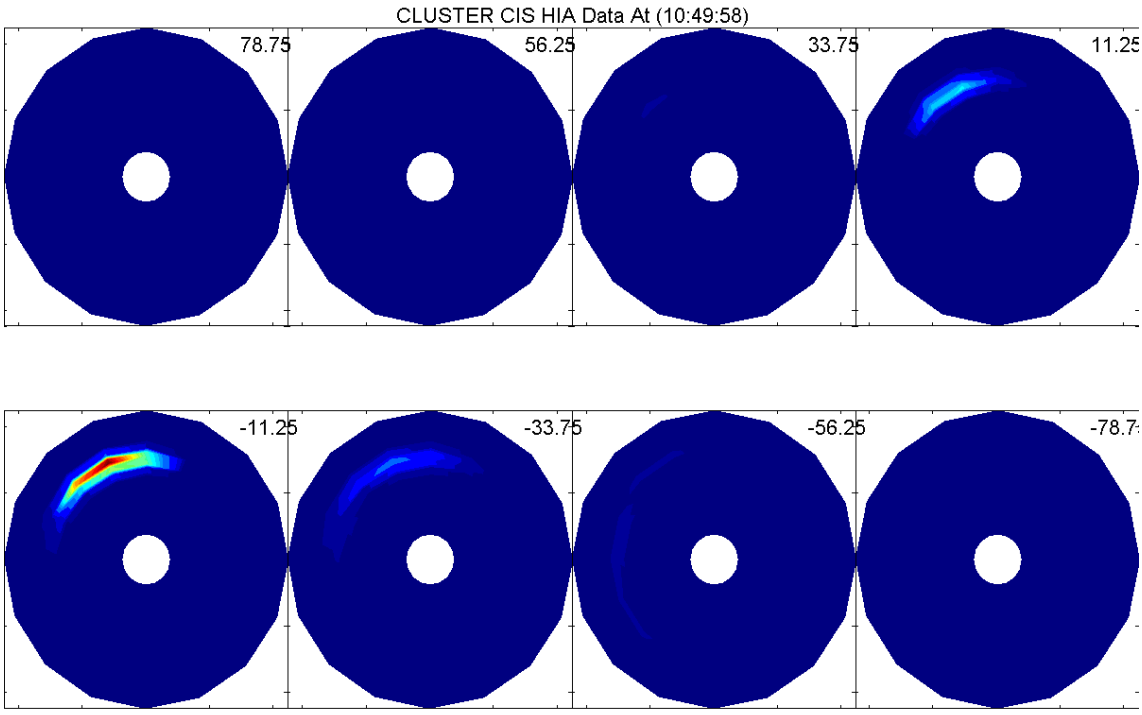

Figure 3.37: The angular population density with respect to the base 10 logarithm of the sampled energy spectrum, ascending with increasing radial distance from the centre from ≈6eV to 29KeV, is plotted for the 8 polar data bins. The angle to the central axis is shown in each (top right). The same energy scale is retained across all of the images.

The polar distributions in Figure 3.37 suggest that, at this early point in the crossing, the particles are generally energetically homogenous and seem to be clustered in such a way as to allow the use of single value state variables and further omni-polar, purely azimuthal investigation.

Figure 3.38, therefore, shows the progression of an omni-polar, azimuthal energy distribution across the period of interest. The centre of the sampling time is shown in the top-right of each frame and the data is of similar format to that in Figure

3.37. In the Figure (3.38) we can see a similar homogeneity in energy distributions to that seen in Figure 3.37 from the way that angular rings are formed with a well defined single peak centre.

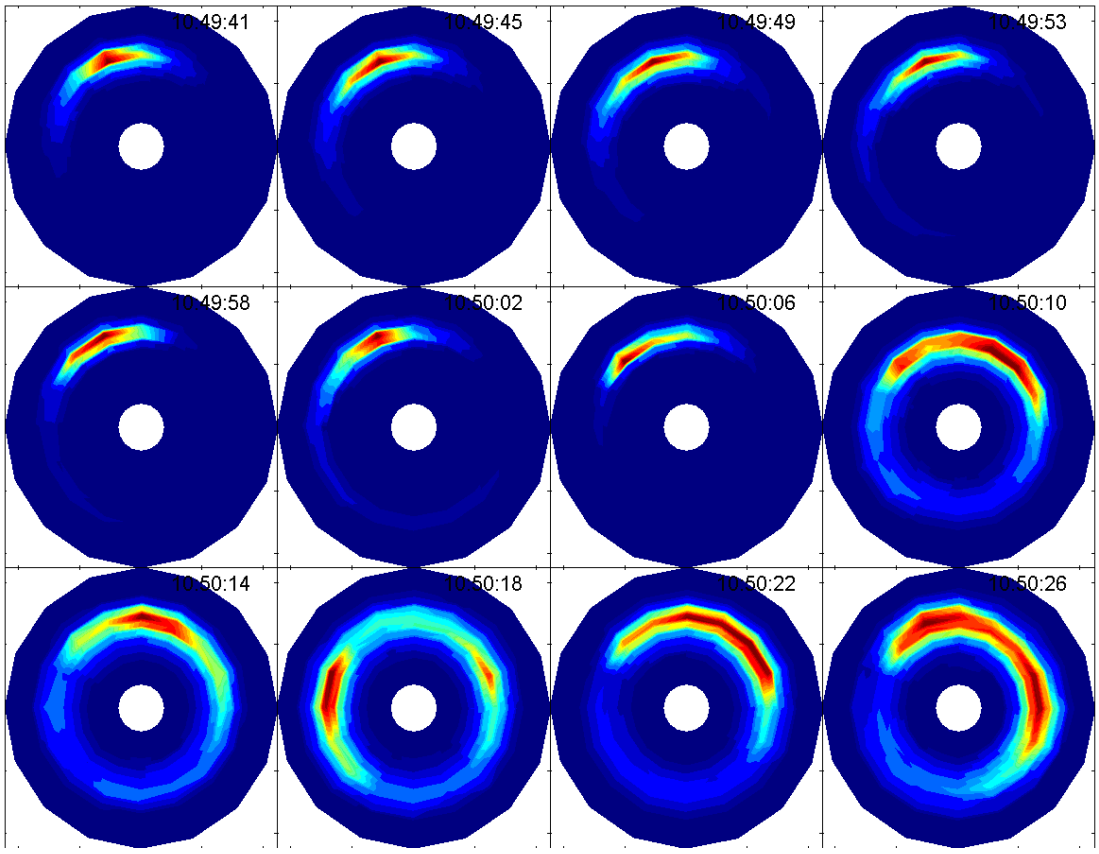

Figure 3.38: The omnipolar, azimuthal particle population distributions of for the flows intersecting Cluster spacecraft 3. A common scale (see Figure 3.38) is retained across the figures such that the minimum and maximum values used for colour scaling are consistant across all time values.

This similarity does not continue to the direction of that velocity. In the previous figure obvious clustering in both energy and direction of particle flux allowed a single value to be assigned to the distribution when used for simulation. The long sampling time for each distribution however may lead to angular smearing if the velocity vector undergoes significant modification.

The image at 10:50:18 UT, for example, suggests particles flowing in almost perfectly opposing directions which might be indicative of either a rapid rotation of bulk velocity flow or of counterstreaming particle flow. The latter behaviour is impossible to describe unambiguously with a single velocity vector. The loss of

information in the compression of the distribution to a single value is a limitation imposed by the single state variable approach and immediately limits its global accuracy.

Initial average variable sets, taken before and after the transition, were compiled from the quiet region before and after the crossing from 10:47:00 to 10:47:30 UT and 10:50:45 to 10:51:15 UT. The calculated values are presented in Table 3.21 below in addition to a measure of the statistical variance defined as, $\frac{\sigma_{Bi}}{|B|}$, the percentage statistical variance with respect to the magnitude of **B**. It makes little sense to consider variances in a single component as field rotation may lead to some components being very small and thus having comparatively large errors even if the variance in that component is comparable to those in other ones that evidence a larger value and thus a smaller percentage variance.

Variable	Pre Value	Variance (%)	Post Value	Variance (%)
B_L (nT)	40.4465	3.40	-11.1570	6.38
B_M (nT)	11.0262	8.01	-55.4552	2.65
V_L (Km/s)	-42.1596	4.23	79.3211	10.64
V_M (Km/s)	-246.6762	1.81	-25.9826	41.15
N_P ($/cm^3$)	15.5779	3.33	0.3147	11.58
T_P ($10^6 K$)	2.2286	1.46	39.8162	7.97

Table 3.21: Initial boundary condition values for the reconnection layer simulation of the transition at 10:50 UT on the 3rd of December 2001.

These values, when used as inputs to the model produce a type II model structure (ASCSA), featuring two slow shocks. The η constant values in the pre and post contact discontinuity regions are 0.99(73) and 0.74 respectively. Suggesting that the leading slow shock is on the cusp of making the transition to a slow expansion fan. The calculated value for $|\mathbf{b}|$ adds more evidence to this, the value calculated for this layer is 1181.9619, where the upper limit for Region II is 1073.48, suggesting it is, instead of the ARCSA type. The upper boundary for this Region III is 1632.20, which is clearly far larger than the calculated value for $|\mathbf{b}|$. All of these calculations were made using the effective mass factors derived using CIS-CODIF data. If the calculation is repeated without using these values there is a change in the η values to 1.08 and 0.80 respectively. We see a small increase in each case and indeed, the

first slow shock has now become a slow expansion fan. In this case the inclusion of heavy ion factors has had a significant impact on the modelled results. Staying, for the time being, with the initial determination using those heavy ion factors a direct comparison between the modelled behaviour and the observed data was carried out. The results of this comparison can be seen in Figure 3.39. What we can see from this figure is the comparatively good agreement between model and data. The magnetic field is the better described of the two, qualitatively, but significant morphological and quantitative coherence can also be seen in the number density and bulk velocity data. There is an anomalous increase in temperature during the second slow shock. This may be due to a number of factors, including but not limited to, the final and extremely low value of the number density. In the functions defining the change in temperature across the slow shock the new value is inversely proportional to the number density and is calculated using the ideal gas equation. This has the knock on effect that if the pressure does not change significantly but the number density drops to a low value the resultant jump in the plasma temperature is significant and likely not a reflection of the actual behaviour of the plasma. This is an issue that should be tackled in the future should this method be subject to continued development.

The analysis of this first pass solution through the genetic algorithms defined in §2.7.1 and §2.7.2 is presented in full in §4.1.2 and §4.2.2.

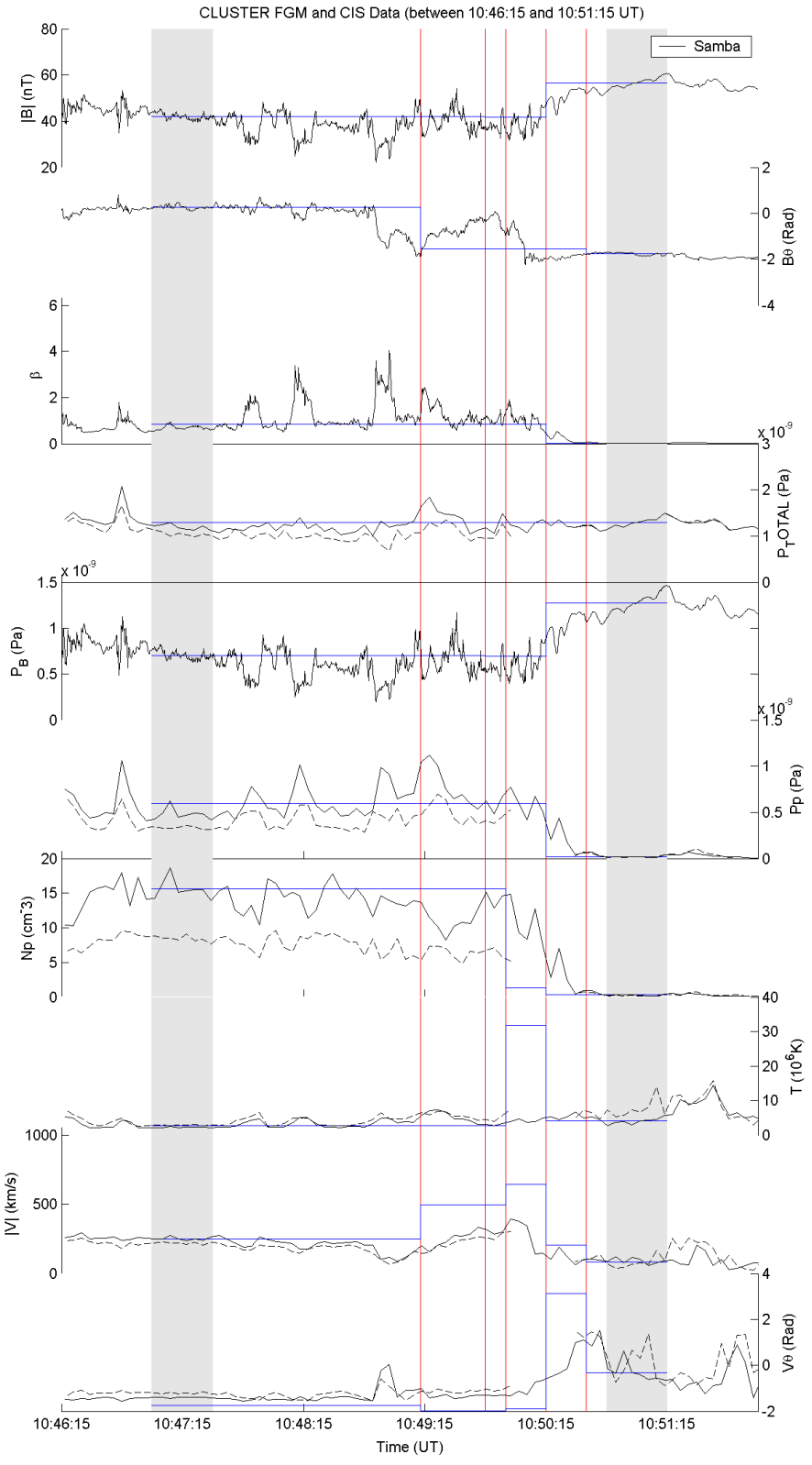

Figure 3.39: Comparative overlay of the reconnection layer model created by the simulation using the initial conditions specified for all magnetic and plasma variables on the 3rd December 2001 at ≈10:50 UT. Observed data from spacecraft 3 is presented in black, modelled in blue, the discontinuities are marked by red vertical lines and the ranges used for boundary condition sampling are shown in grey.

Event 2: 10:58UT

The second event described by Retinò et al. (2005) occurred at approximately 10:58:00 UT on the 3rd of December 2001.

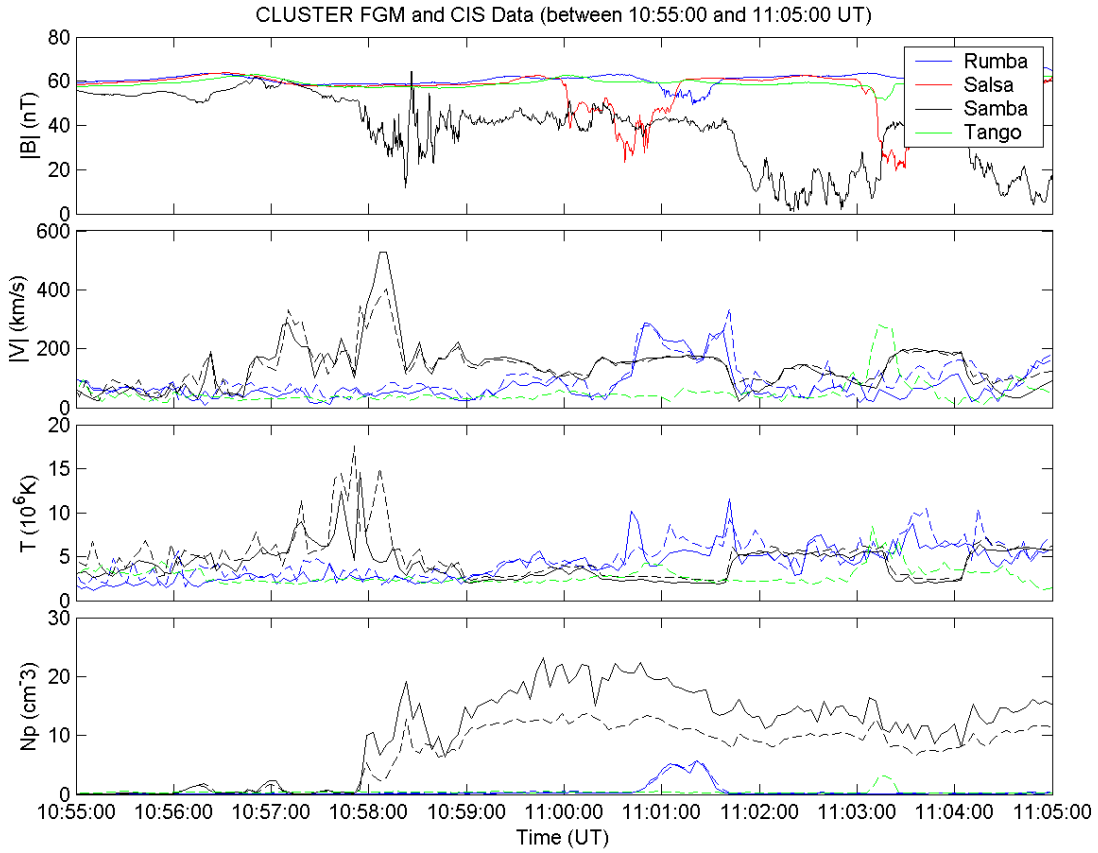

Figure 3.40: Plasma parameter overview of the transition at 10:58:00 UT on the 3rd of December 2001 for all 4 CLUSTER spacecraft.

An overview of collated plasma parameters during the event is presented in Figure 3.40, covering a 10 minute period describing the full extent of the event for all spacecraft. Although the crossing is primarily visible in spacecraft 3 data, attenuated signatures do exist in the data for the group I spacecraft. The crossing for spacecraft 1 is only partial and may be incomplete, illustrated by the final values reached and changes in magnetic field and ion data with respect to previous complete crossings. It is possible that the electron transition parameter described by Lockwood et al. (Lockwood and Hapgood, 1997) could be used to ascertain the degree of transition in this case should sufficient electron data be available.

In an attempt to generalise an analysis frame for this feature, a boundary nor-

mal frame determination was attempted for each spacecraft. For spacecraft 1 the transition feature lies between 11:00 and 11:02 UT. The resultant analysis gave a normal vector of $GSE(x, y, z) = (0.8818 \pm 0.0023, 0.4427 \pm 0.0134, -0.1625 \pm 0.0252)$ or in polar coordinates $(R, \theta, \phi) = (1, 27°, -9°)$. The method that provided the vector that gave the lowest trans-crossing gradient and variance in this case was the tangential discontinuity method. The values for each method are tabulated in Table 3.22.

Method	∇	$\langle B_N \rangle$	Variance (σ_{B_N})
Model Normal	0.01	15.52	4.64
Tangential Discontinuity	0.00	0.69	4.23
MVA	-0.01	-47.88	2.32
MVAB	0.00	-0.47	4.37

Table 3.22: A comparison of gradient, average normal magnetic field component magnitude and variance for all four boundary normal vector determination methods for spacecraft 1 over the feature at ≈11:00 UT on the 3rd of December 2001.

The theta value of the calculated normal vector, may seem anomalously low for an event whose spatial trajectory might be nearly tangential to the surface of the dusk-side magnetopause. Using the normal vector calculated using the tangential discontinuity method the data was transformed into the frame of these axes.

This transformed data was then subject to de Hoffmann-Teller analysis. The resultant frame dependent velocity vector was LMN(x,y,z)=(80.78, 382.41, 0.62). The linear fit parameters for this vector are suggestive of a well, but not perfectly, defined de Hoffmann-Teller frame with a gradient of 0.91, a correlation coefficient of 0.87 and a value for the reduction factor of $D/D0 = 0.18$. The latter value means that the convective electric field has been decreased to approximately 18% of its original value.

The low value of V_{HT_N} suggests that at the time of crossing the magnetopause boundary is almost stationary. The result of this is that crossings should then sample the spatio-temporal structure without any, comparative, concern about the nature of the boundary moving over the spacecraft.

Walèn testing within this range gave only a correlation coefficient of 0.73 and

a gradient of 0.28. In this case, at this early stage, the tangential stress balance relation is not conclusive in deciding whether this encountered flow is connected to the reconnection region. This may be due to several factors. One possibility may be the lack of completeness of the crossing. Another factor arises when the time series bulk velocity data is examined (Figure 3.41). It can be seen that there may actually be two phases of acceleration. One beginning in V_L from ≈11:00:13 to ≈11:00:37 UT evidencing simple acceleration and another, substantially larger, enhancement with a degree of rotation in V_M from ≈11:00:37 UT to ≈11:00:45 UT. This two stage acceleration, acting almost orthogonally to one another, might suggest two ion populations, two spatially commingling structures or possibly two acceleration mechanisms at work at this point in time.

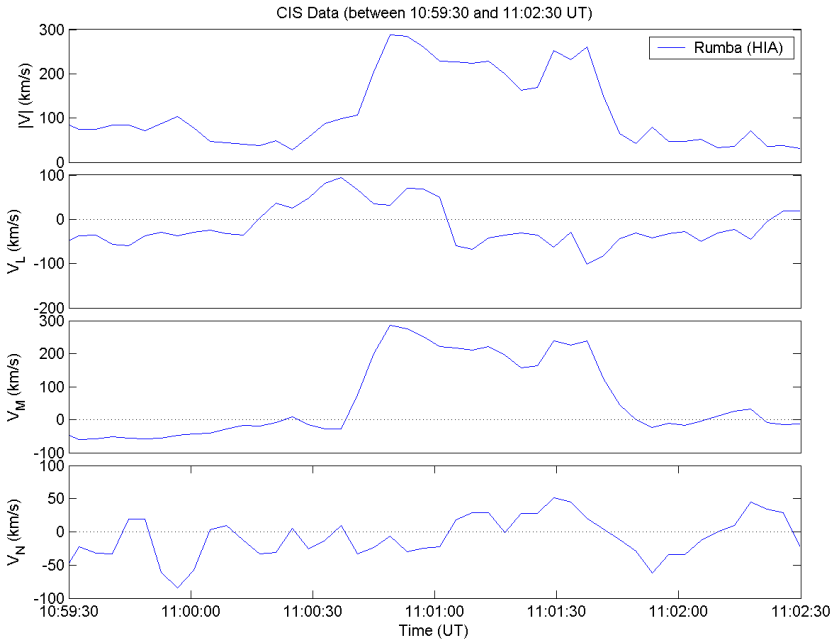

Figure 3.41: Magnitude and component breakdown of the bulk velocity data for spacecraft 1 while crossing the feature at $\approx 11:01UT$.

Evidence for this view appears in the phase-space distribution function of the ions as recorded by the HIA instrument. In the period from 11:00:11 to 11:00:31 UT there is no clear structuring of the population being accelerated. However, over the second period, 11:00:37 to 11:00:49 UT, there are clear signs, especially at the beginning, of a D-shaped ion distribution suggesting the presence of reconnection flows.

Spacecraft 2, lacking a working CIS instrument, can only be analysed, in this case, in terms of magnetic field alterations. From comparison of magnetic field data with spacecraft 1, spacecraft 2 seems to have had two intersections with the event observed by spacecraft 1, at 11:00:00 to 11:01:00 UT and 11:03:00 to 11:03:20 UT. The morphology of the two events is very similar even though the total magnitude is not, as is shown in Figure 3.42.

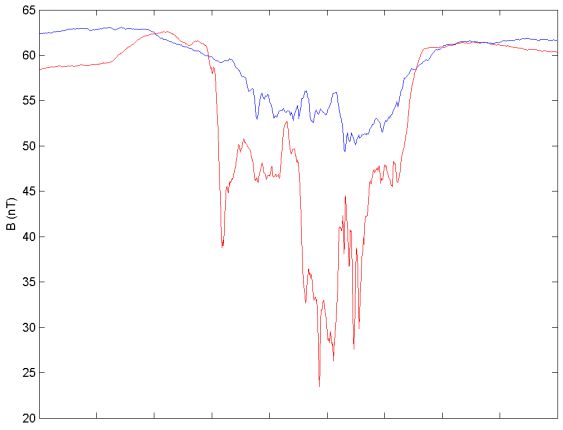

Figure 3.42: A morphological comparison of a magnetic field event encountered by spacecraft 1 (blue) and 2 (red). Data has been temporally re-sampled for comparison but not normalised.

Difficulties arise in analysis of spacecraft 2 data based on the lack of any ion data. Based entirely on magnetic field data, however, the first crossing evidences fast changes and lacks a stable point to allow interpretation using the tangential discontinuity method. Yet it does hows signatures that are clear and show strong similarities to those evidenced in earlier crossings by all 4 spacecraft.

Minimum variance analysis provides a value with significant uncertainty in terms of the gradient and statistical variance values of only 0.03 and 87.27 respectively. Not enough to base any kind of significant analyses upon.

Analysis of the second crossing of the event at 11:03:20 UT gives a boundary normal of GSE(x,y,z)=(0.8253±0.0328, 0.2214±0.0343, -0.5195±0.0610) or $(R, \theta, \phi) = 1, 15°, -31°)$ which, while showing some variance, remains similar to that arrived at in the earlier, pre-simulation, events.

Spacecraft 4 exhibits much the same variable behaviour as spacecraft 1, on an even further reduced scale. It is therefore possible to suggest that the interaction of

this spacecraft with the layer is minimal, with no significant degree of translation across the transition layer at this point in time.

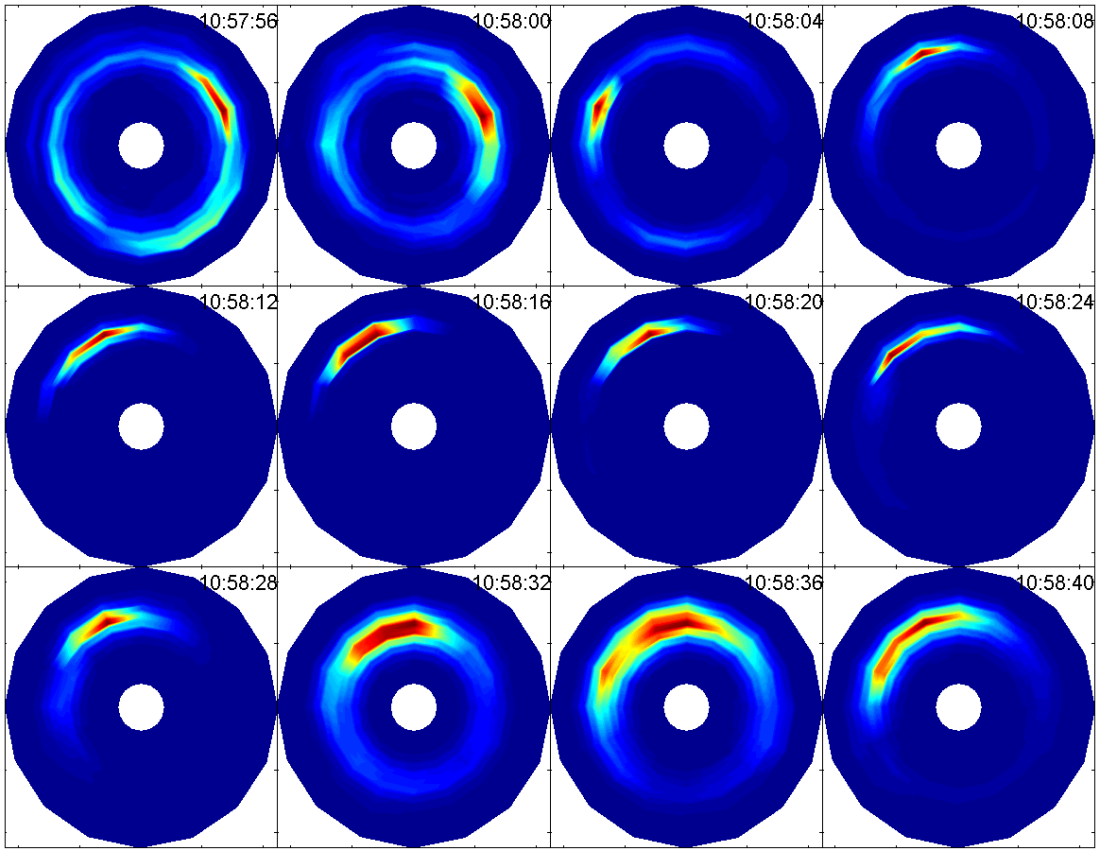

Figure 3.43: An omni-polar azimuthal plot of particle population distributions between 10:57:56 and 10:58:40 UT on the 3rd of December 2001. Radial distance from the centre of each spectrogram indicates logarithmically increasing energy. The full energy range of the CIS-HIA instrument, ≈6ev to 29KeV, is shown.

Figure 3.43 shows the progression of the particle flow characteristics across the transition at 10:58 in the previously described omni-polar azimuthal energy format (Figure 3.38). The distribution of particle flow seems also to support, within experimental tolerances, the use of the provided plasma moments and thus this type of approach to simulation, as the degree of coherence is generally high with well defined structures during intervals with the higher number density.

During this period spacecrafts 1, 2 and 4 undergo a slow transition between 10:35:00 and 10:45:00 UT. There isn't a well defined crossing structure, as temporal and spatial factors can possibly subsume the signatures of the reconnection process. As such only spacecraft 3 can be analysed for this crossing with any expectation of

accuracy as the transition takes place over a far shorter timespan.

When subject to boundary normal analysis methods the magnetopause normal vector was calculated, after selection based on the criteria described in §2.1.4, to be $GSE(x, y, z) = (0.7560 \pm 0.0061, 0.2739 \pm 0.0083, -0.5945 \pm 0.0116)$ in Cartesian coordinates or $(R, \theta, \phi) = (1, 20°, -36°)$ in polar ones with a mean magnetic field normal component of 0.28nT across the transition period.

Signatures in the bulk flow data suggest that the strong, clear velocity enhancement visible at approximately 10:58 UT appears purely as a feature tangential to the magnetopause boundary layer with the normal parallel velocity showing little variation or magnitude within the layer and a comparatively low magnitude sunward component before, and earthward component after the transition. This orientation would agree with inflow into a reconnection layer as sampled on an outbound (magnetosphere to magnetosheath) crossing.

The perpendicular velocity enhancement is of the order of 500% of temporally and spatially local values. The central section of this feature was selected as the sampling period for dHT analysis, namely from 10:58:00 to 10:58:15 UT. The results, seen in Figure 3.44(a), provide strong evidence for the presence of a well defined de Hoffmann-Teller frame for this feature as the linear fit correlation coefficient was ≈0.97 and the gradient was 1.00. The reduction factor of the convective electric field also adds evidence with a 97% decrease in total magnitude inside the frame (D/D0 = 0.03) defined by $\mathbf{V}_{HT}$(x,y,z) ≈ (-165, -278, 2) km/s. The spacecraft normal velocity at this time was $\mathbf{V}$(x,y,z) ≈ (-50, 208, -54) km/s.

Pointwise testing of the Walèn relation over the complete time period gives strong evidence of agreement with the conclusion of the dHT analysis in that there is a coherent convecting structure that is part of the velocity enhancement seen during this crossing. The results of this testing can be seen in Figure 3.45. An important feature to note is the transition from a negative gradient and correlation coefficient in the pre-layer region to positive values during and after the transition with a corresponding increase in the correlation coefficient.

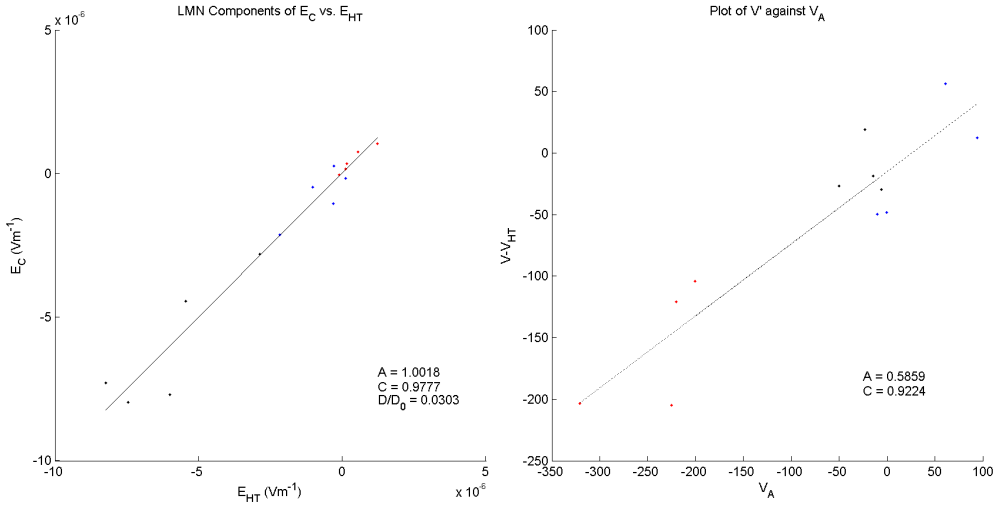

(a) The results of the dHT analysis carried out on the transition at 10:58 UT and the linear regression performed to quantify them.

(b) Displays the results of the application of the tangential stress balance relation (Walèn test) to the dHT frame defined in the previous figure.

Figure 3.44: de Hoffmann-Teller and Tangential Stress balance analysis results for Spacecraft 3 in a transition across the magnetopause at ≈10:58UT on the 3rd of December 2001.

Walèn testing over the complete time period provides slightly less conclusive values with the correlation coefficient now falling to 0.92 over the centre of the feature. The original paper specifies a possible reason for this, in that it is suggested that during this interval there may be a transition across the x-line. For this reason during the transition first one side and then the other would be sampled and would therefore may not conform to a single type of field alignment geometry, as required by the dHT and Walèn methods. The gradient of the linear regression is 0.59 and as such shows some degree of agreement with the predictions of acceleration by a slow shock.

The positive gradient and correlation coefficient suggest that the spacecraft is now crossing the layer in question northward of the reconnection region. This adds evedence to the possibility that there has been transit of the spacecraft past the diffusion region or x-point. The results for these tests are presented in Table 3.23.

In preparation for the simulation initial intervals have to be decided for the boundary value sets. In this case the requirement is a location on either side of the

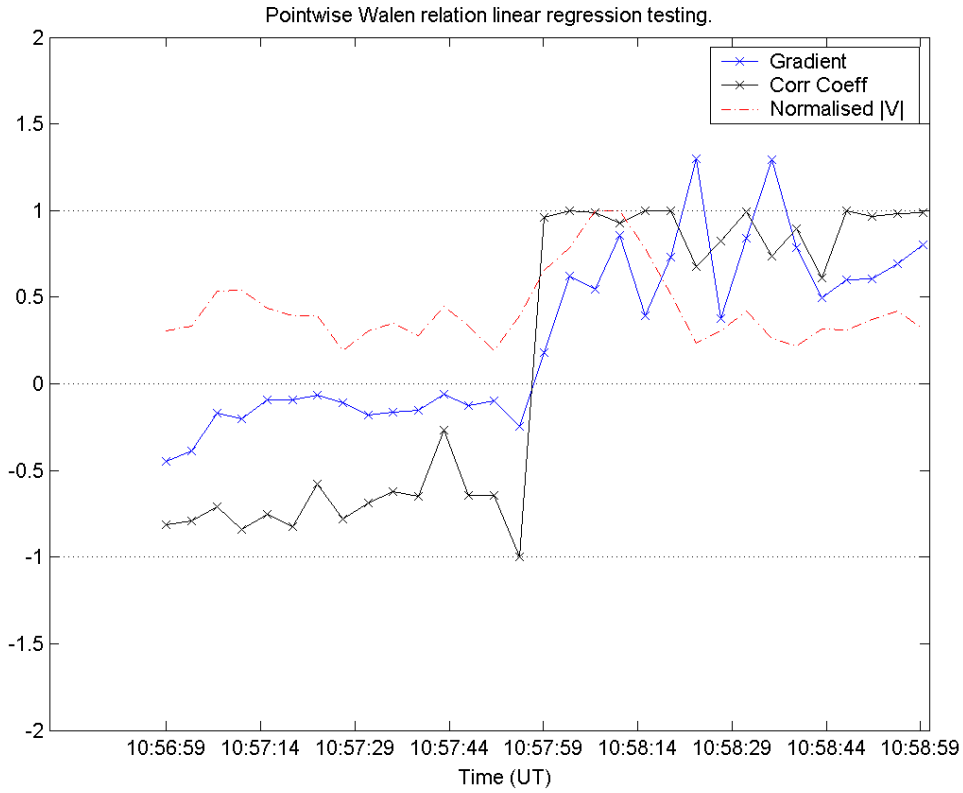

Figure 3.45: Results of a point-by-point comparison between observed bulk velocities and the predictions of the Walèn relation during the transition at ≈10:58 UT on the 3rd of December 2001 for spacecraft 3.

de Hoffmann Teller Analysis					
V_{HTL}	V_{HTM}	V_{HTN}	A	C	D/D0
-164.91	-278.45	1.75	1.00	0.98	0.03
Tangential Stress Balance (Walèn Relation) Analysis					
A		B		C	
0.59		-15.11		0.92	

Table 3.23: The results of tests for the fluid signatures of reconnection carried out on data from Spacecraft 3 during the crossing at ≈10:58 UT on the 3rd of December 2001. Data was drawn from between 10:58:00 and 10:58:15 UT in each case.

transition where conditions and behaviour tend towards constancy. A mean value of each variable can then be calculated and used as the basis of the simulation. In this case the selection of those intervals was hampered by the generally noisy condition of some of the variable components, most notably those associated with the ion measurements. The recorded number density during this time was very low so the moments derived from this data have a higher degree of uncertainty, and noise, associated with them. The initial value intervals chosen for this simulation ran from 10:54:00 to 10:55:00 UT before the transition and 11:00:30 to 11:01:00 UT after it. This selection is highlighted in the simulation results Figure 3.46.

The initial conditions derived from these intervals are summarised in Table 3.24.

Pre-Layer Components. Taken from 10:54:00 to 10:55:00			
Variable	Value	Absolute Statistical Error	Percentage Error
$B_L(nT)$	-17.6234	1.08	1.94
$B_M(nT)$	-52.7606	0.40	0.73
$V_L(km/s)$	23.9845	3.84	6.41
$V_M(km/s)$	48.8022	8.09	13.50
$N(/cm^3)$	0.16843	0.02	11.79
$T(10^6K)$	4.5496	0.03	6.18
Post-Layer Components. Taken from 11:00:30 to 11:01:00			
Variable	Value	Absolute Statistical Error	Percentage Error
$B_L(nT)$	18.7554	7.63	19.02
$B_M(nT)$	34.9216	5.87	14.65
$V_L(km/s)$	-74.9110	8.58	5.40
$V_M(km/s)$	-140.0832	2.61	1.54
$N(/cm^3)$	20.7705	0.38	1.85
$T(10^6K)$	2.2709	0.04	1.58

Table 3.24: Initial boundary values, derived from spacecraft 3 data, input into the reconnection layer model for the transition at 10:58 UT on the 3rd of December 2001.

The intervals selected were, needfully, a compromise between the magnetic field and ion observations as can be seen. In the pre-layer region the magnetic field measurements were comparatively noise free, yet due to the low number density the values recorded by the CIS-HIA instrument were subject to significant variation.

During the latter interval, the spacecraft had passed into the (magnetosheath) where the particle density was much higher and therefore ion observations are more reliable. The magnetic field, however, has decreased in total magnitude and shows a much higher variance, thus the percentage error is higher.

First pass simulation of this crossing gives a indeterminate solution with the parameters as described. It is therefore required that the model be constructed, first, by reversing the sets of input parameters (pre for post and vice versa) and then the resultant model flipped again. This is a problem with the initial determination of η imposed by the fact that the model, in its current state, has a direction bias with respect to the direction of magnetopause transitions.

The constructed model is defined by the following structural constants: The two η values for the slow shock/slow expansion fan pairs are 1.12 and 0.80 respectively. This suggests that the structural type should definitely be ARCSA, although as the latter value is so close to unity it may be tending towards a collapse of the second slow shock into a slow expansion fan. The $|\mathbf{b}|$ value is 1550.08 with the adjacent region ii and iii values being 1444.44 and 2265.94. This is in concurrence with the other values and confirms this structural type.

The structure itself, when compared with the recorded data shows a comparatively short, with respect to previous crossings, temporal span of approximately a minute. This short time should enhance the signal to noise ratio of the features themselves as spatio-temporal variations have less time to act. However, this also leads to a decreased time over which those features may be sampled by the spacecraft. This structure is reproduced in full in Figure 3.46.

Analysis was then carried out using the genetic algorithms described previously. It can be found in §4.1.2 and §4.2.2 for the RLDS and BVSR algorithms respectively.

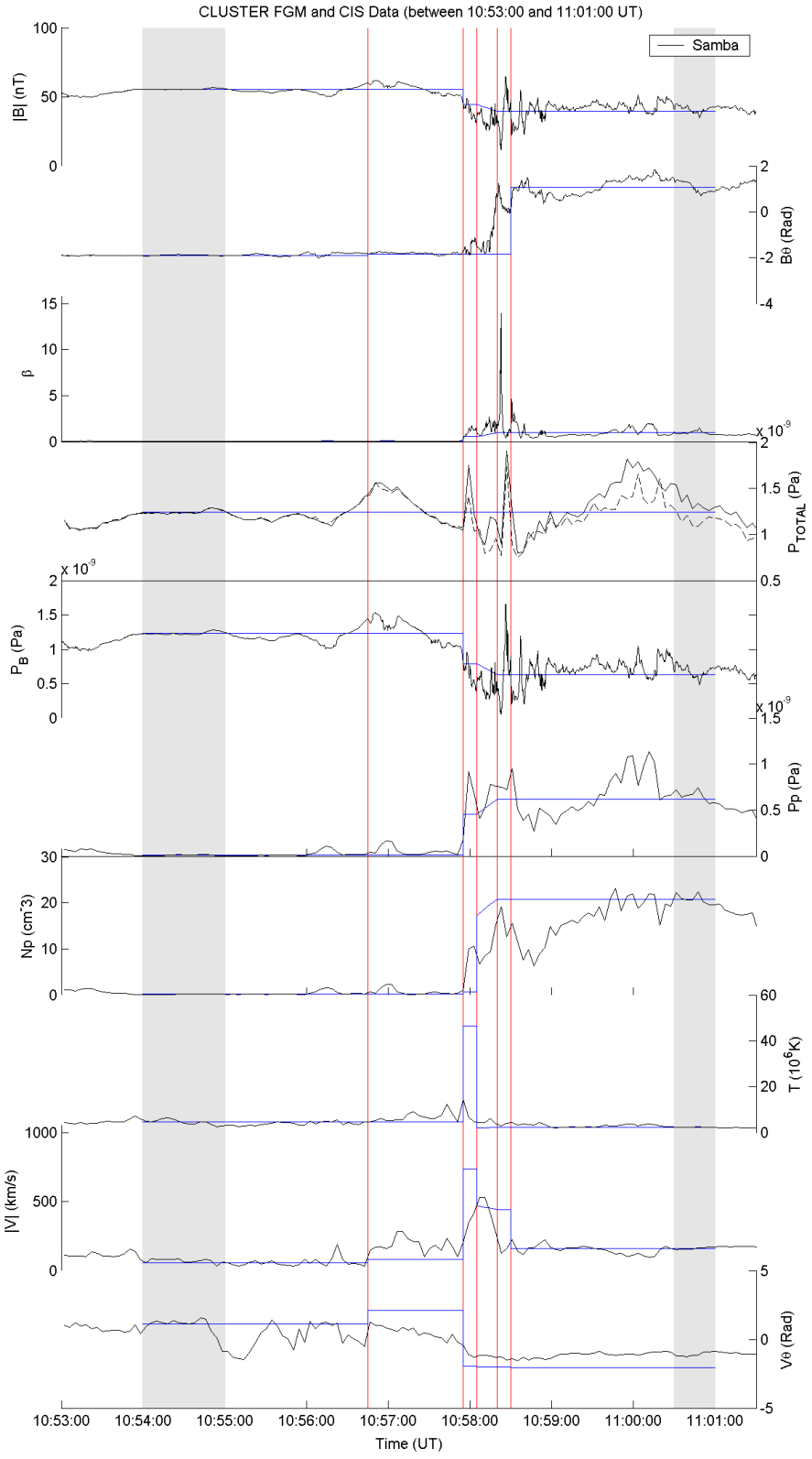

Figure 3.46: Comparative overlay of the reconnection layer model created by the simulation using the initial conditions previously specified for all magnetic and plasma variables. Observed data is presented in black, modelled in blue, the discontinuities are marked by red vertical lines and the ranges used for boundary condition sampling are shown in grey. The modelled event occurred at 10:58 UT on the 3td of December 2001.

Chapter 4

Analysis using Genetic Algorithms

In this section the analyses resulting from the application of the genetic algorithms defined in §2.7.1 and §2.7.2 will be described. In each event case the RLDS algorithm was the first to be applied to the data. BVSR determination does not, fundamentally, change the distribution of wave modes, only their effects. This independence suggests that the structure and timing of the wave modes in any specific analysis case can be established with a significant degree of coherence without concern for loss of BVSR accuracy. Although initially created as seperate entities, the two algorithms have since been conflated into a single analysis tool.

4.1 Analysis through RLDS

4.1.1 ASCSA Type: 1st April 2003

Event 1: 02:27UT

The simulation analysis for this event through RLDS highlighted differing trends in the single variable vs. multi variable approaches.

In the cases where single variable analysis was used, it often led to the compression of non-perturbing wave modes into single multi-mode structures. For example, magnetic field magnitude simulations regularly exhibt compression of the initial Alfvén-wave into an Alfvén/Slow Mode-wave pair as the former has no effect on

that variable in the model. Simulations using bulk plasma velocity do not seem to have been as susceptible to this. This difference is likely to be because Alfvénic acceleration is permitted by all of the wave-mode equations and therefore leads to changes in the flow velocity across the Alfvén wave. Figure 4.1 below shows several cases of this multi-modeing behaviour taking place. Overlapping peaks of wave modes that are consecutive within the model are a sign of this, as it suggests the following mode has effectively no temporal (and therefore spatial) extent. The wave component is either effectively not present or is as close to a mixed-mode structure as the model allows.

To mitigate this possibility it is possible to either choose a variable that has a perturbatory value at each discontinuity or perform multivariable analysis. A multivariable approach may use any combination of the variables provided as moments. To provide completeness, the available moments were gathered into two variable sets, the CODIF and HIA sets comprising: [B (FGM), V, N, T (CODIF)] and [B (FGM), V, N, T (HIA)].

Each set, having a different ion data basis, may produce different initial reconnection layer models. The structures that comprise these models may be compared and contrasted in terms of the boundary conditions and the sensitivity and range of each instrument. These comparisons can be used to clarify the predicted structure or highlight conditions at variance with the theoretical basis of the model.

To facilitate comparison between models and the analysis of an event as a whole, a way to describe and label each model produced was considered. The systems considered were: the single elements that comprised the model, the frequency of the occurrence of those elements (see Figure 4.1), and the timing structure as a whole and how often the complete structure (or one similar to it) was produced. For this, the method described for classifying structures (see §2.7.2) is applied. Each of these structures is unique and can be described in terms of its fitness and features as a separate possibility.

In this case, for a low "tolerance" value of 6 seconds, enough to encompass 2

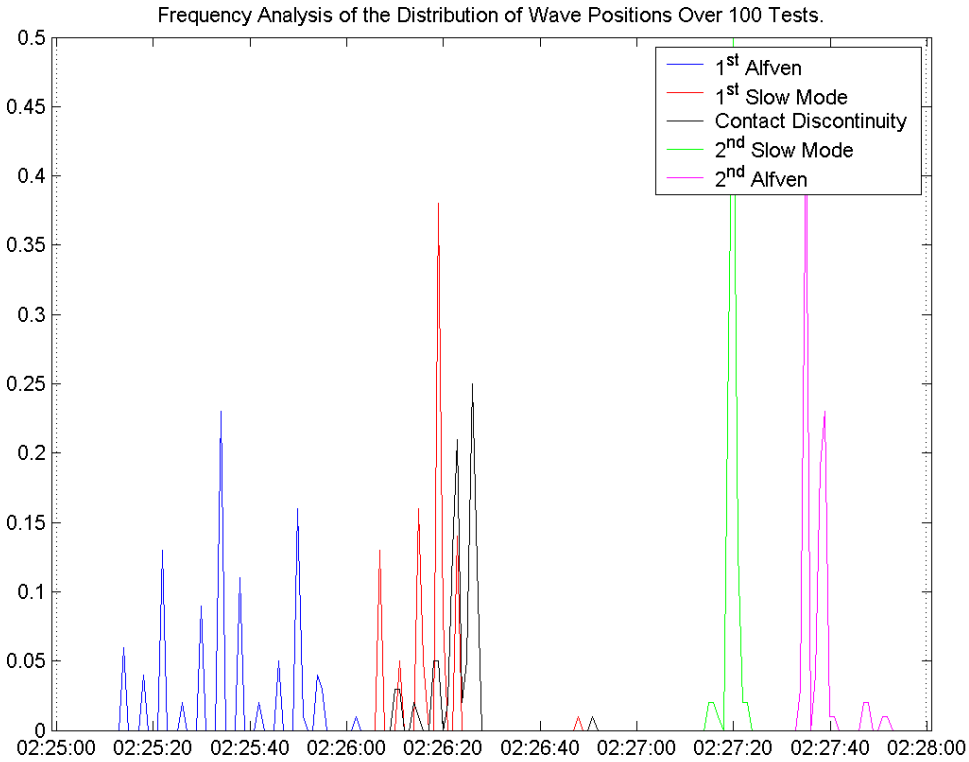

Figure 4.1: Histogram frequency analysis of the occurrence of a particular wave time in the solution arrived at using the RLDS method for the event at 02:27UT for spacecraft 3. The x-axis range was binned in units of 1 second.

neighbouring peaks but not 3, the number of unique structure groups found in 100 possible tests was 36. When the singleton groups are eliminated this falls to 20. Although it is possible to describe each of these, those that are most important are those occurring most frequently, and those with the best "fitness" value. As such, when subjected to frequency analysis these modes give rise to specific groups the results for the 5 most populous groups are reproduced in Table 4.1. Groups 13 and 23 have equal populations, so both are included for completeness.

The sum of the percentage occurrence (Total) column does not add up to 100. This is the case, by design, because the algorithm only looks for model structures that occurred more than once in the one hundred tests that were carried out. Fitness values were calculated for each of the grouped structures and the values are also present in Table 4.1. As all of these models are derived from the same observational data it is possible to compare them directly. Comparing models, possibly, between

	Percentage		Fitness		
Group Number	Grouped	Total	Magnetic	Plasma	Total
12	5.83	6	4.50	19.33	23.84
13	4.85	5	4.58	19.18	23.76
23	4.85	5	4.48	19.45	23.93
30	12.62	13	4.54	19.95	24.49
32	10.68	11	4.56	19.39	23.95
36	7.77	8	4.53	19.27	23.81

Table 4.1: The percentage occurrence of the structural groups calculated during the RLDS tests. The Grouped, value denotes the percentage occurrence in comparison to the total population that was grouped, i.e. non-single occurrence structures. The Total value is the percentage occurrence of that structure with respect to all tests carried out.

events and certainly between cases requires taking note of event length and local conditions.

It should be noticed that although group structures provide information about the nature of the multi-variate fitness landscape, and the performance of the algorithms that explore it, the best model that conforms to a particular transition layer may not be embodied in a group set, but by a single solution found during the construction of those group sets.

In this analysis case the RLDS solution that provides the greatest fitness is a single distinct, as opposed to a group, solution. The combined fitness value is 23.00 and component magnetic and plasma fitness values are 4.41 and 18.58. This solution occurs as a singular solution under both grouped and ungrouped approaches as it is not within the tolerance range specified for the group solution merging. The layer-by-layer variable breakdown is presented in Table 4.2. The non-boundary fitness is here defined as the summation of the fitness values for any variable(s) across the regions within the reconnection layer itself. This value does not include the fitness values used by the BVSR algorithm, those adjoining the layer as boundary conditions but not part of it. From the tavle we can see the non-boundary fitness is 3.75 for the magnetic field data and 7.16 for the plasma data, giving a total of 10.91. The difference between the combined fitness and non-boundary fitness values highlights the significant role played, in this system, of fitness optimization in the

regions bounding the reconnection layer.

Variable	A-S	S-C	C-$\tilde{S}$	$\tilde{S}$-$\tilde{A}$
B (FGM)	0.70	0.81	1.76	0.48
V (HIA)	0.80	0.03	0.02	0.18
N (HIA)	0.11	0.74	2.02	0.15
T (HIA)	0.32	0.20	0.23	2.34

Table 4.2: A breakdown of the fitness values for each variable using the best RLDS set for each discontinuity during the 02:27UT crossing.

Event 2: 02:35UT

After the initial pass simulation for this event had been completed the time series limits on the location of the reconnection layer were specified. The end of the pre-layer variable sampling region was used as the starting limit, and the start of the post-layer sampling region was used as the finishing limit. The simulation was run using the HIA variable set (B (FGM), V N T (HIA)) and 100 solutions were produced. At this time, solution settling times were not collected and so analysis over these values for this particular event is not possible.

The resultant solutions were then subject to histogram frequency analysis to highlight the most populous, if not the fittest, solutions. The time range was divided into 1 second bins and the solutions were placed into these bins. The results of this analysis are shown in Figure 4.2

Significant clustering is evident in the data for all discontinuities, most strongly in the 2nd Slow Mode and 2nd Alfvén wave cases. These latter cases are almost single valued, suggesting strong evidence for the positions being constant in any model using this framework being applied to this crossing. The other three discontinuities have more complex distributions although each has a specific frequency peak that is not coincident with either of the others. Taking into consideration the 4 second spacing of the peaks the pattern of those peaks may, in fact, be mappable to a Normal or Gaussian probability distribution.

Group analysis of the raw solutions may be a another form of distribution mapping, and it presents a mixed picture (Table 4.3). Due to the temporal convergence

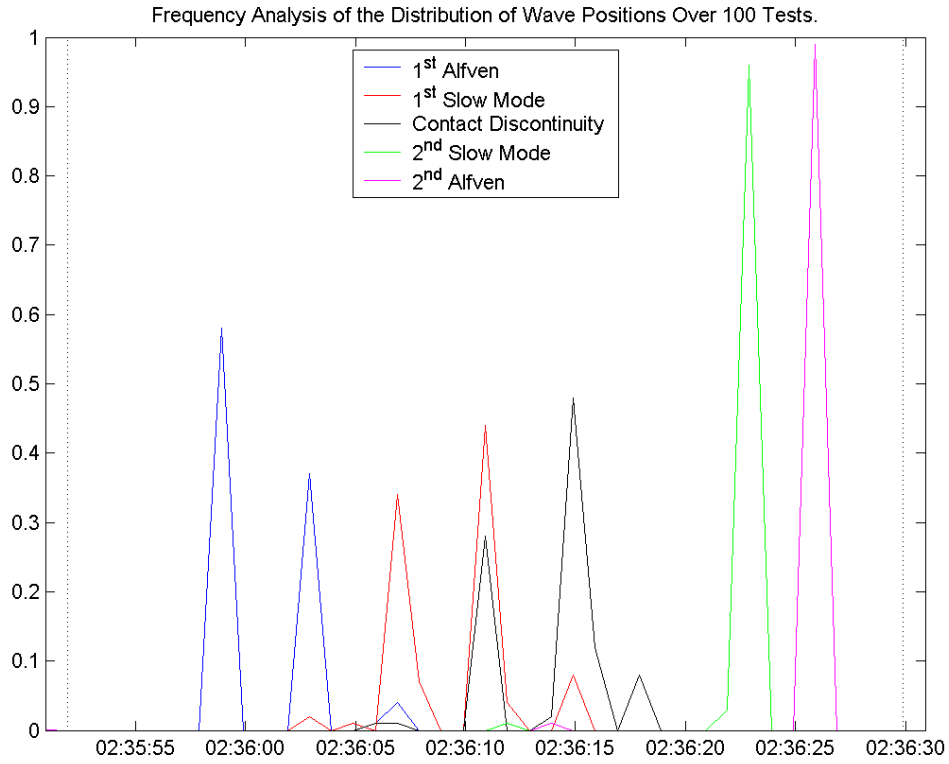

Figure 4.2: Histogram frequency analysis of the distribution of discontinuities arrived at through RLDS using spacecraft 3 data at 02:35UT.

of some of the groups, some members of one group are also considered part of another nearby group as members were within the tolerance range specified. This has been a recurring issue, during this study, with this type of analysis that remains unsolved at this time.

	Percentage		Fitness		
Group Number	Grouped	Total	Magnetic	Plasma	Total
1	30.63	49	5.06	240.47	245.52
2	25.63	41	5.57	314.17	319.73
3	3.75	6	4.08	250.10	254.17
4	33.75	54	5.48	216.12	221.59
5	5.00	8	4.08	280.87	284.96

Table 4.3: The percentage occurrence of the structural groups calculated during the RLDS tests. The Grouped, value denotes the percentage occurrence in comparison to the total population that was grouped, i.e. non-single occurrence structures. The Total value is the percentage occurrence of that structure with respect to all tests carried out.

The fittest non-singleton group is group 4, it is also the group with the highest

population. Single solution analysis, however, gave a result with a comparative fitness value of 217.92 and magnetic and plasma component fitness values of 5.01 and 212.91 respectively. Compared with the results from the group analysis it is clear that this single solution is more accurate than the Grouped structure for both magnetic field and plasma data. It is this single solution, therefore, that was used during the BVSR analysis in §4.2.1.

Variable	A-S	S-C	C-$\tilde{S}$	$\tilde{S}$-$\tilde{A}$
B (FGM)	0.21	2.29	1.56	0.68
V (HIA)	0.23	0.20	0.26	0.15
N (HIA)	0.17	0.14	0.17	0.35
T (HIA)	2.51	3.40	5.75	1.14

Table 4.4: A breakdown of the fitness values for each variable using the best RLDS set for each discontinuity during the 02:35UT crossing.

4.1.2 ARCSA Type: 3rd December 2001

Event 1: 10:50UT

Using the initial model structure derived in §3.3.3, in addition to defining the temporal layer boundaries as running from 10:47:30UT to 10:50:45UT, the RLDS algorithm was used to generate a pool of 100 possible solutions. These solutions, when generated, were subject to histographic analysis to identify trends within the data. The results of this analysis can be seen in Figure 4.3. The histogram shows that, structurally, the event is modelled to take place in two distinct halves. The first half of the event contains the first three modelled discontinuities (Alfvén, Slow Mode and Contact Discontinuity) and the second half contains the latter two (Slow Mode and Alfvén). Each of these three modes evidences at least one primary peak that is temporally distinct from those for adjoining modes. The solution population peaks extending away from the central maxima during the first half of the modelled event do, however, seem to be subject to considerable overlap. The central contact discontinuity and its following slow mode shock, although divided in time, both evidence a two peak behaviour suggesting two almost equally optimized positions, a possible

degeneracy in placement.

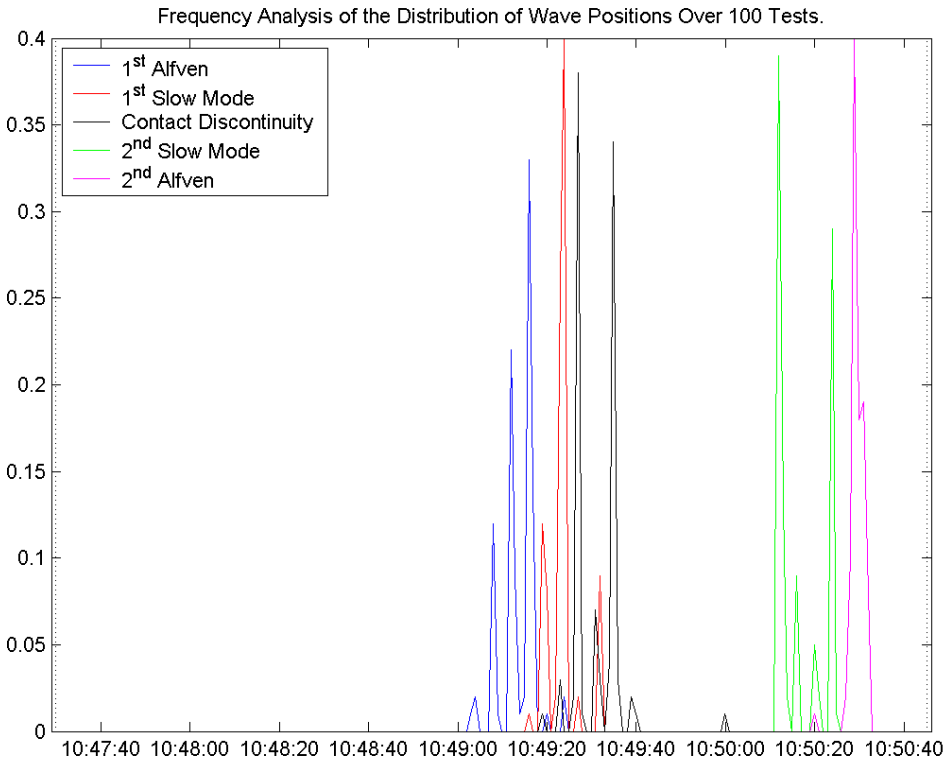

Figure 4.3: Histogram frequency analysis of the distribution of discontinuities arrived at through RLDS using spacecraft 3 data on the 3rd December 2001 at 10:50UT.

Group analysis of these solutions gave 17 separate groups, only 7 of which were not single membered. This high degree of clustering may suggest a stable solution close to the minimum value in the fitness landscape. The fitness of the group solutions with a high population was directly compared with the fittest single solution to find out if the groups found represented the best description of the event. The fitness statistics relating to the non-singleton groups are presented in Table 4.5. The most accurate solution there, by a significant margin, is that of Group 2 with component fitness values of 2.10 and 7.81 for the magnetic field and plasma components respectively and a total of 9.91.

The fittest single solution set was found to have very similar fitness values to those listed in Table 4.5. The magnetic field and plasma fitness values were 1.68 and 7.57 respectively, with a total of 9.26. This is an overall improvement in model

	Percentage		Fitness		
Group Number	Grouped	Total	Magnetic	Plasma	Total
1	21.51	20	2.22	8.06	10.28
2	22.58	21	2.10	7.81	9.91
3	2.15	2	1.97	8.33	10.29
4	10.75	10	2.31	8.49	10.80
5	13.98	13	1.81	8.24	10.05
6	11.83	11	1.76	8.85	10.61
10	6.45	6	1.68	9.00	10.72

Table 4.5: The percentage occurrence of the multi-member structural groups calculated during the RLDS tests. Presented with the total fitness factors associated with the Magnetic and Plasma variables used to test the model structure in addition to the overall total. All fitness values only include intra-layer values, not boundary conditions.

fitness of $\approx 3\%$. Considering each component seperately presents and more mixed picture because although the magnetic field and temperature fitness components show reductions (20% and 9% respectively) the bulk velocity and number density values show increases (of 16% and 11% respectively).

Two possible issues with this approach are highlighted by these results. Firstly, by considering only the changes in overall fitness during inter-generation seed selection, the optimization process becomes a system of trade-offs as it allows decreases in the fitness of one variable to be balanced by increases in others. Secondly, any single model described here is constructed in a single piece by evolutionary methods. It does not include the possibility of compiling hybrid sets using multiple solutions drawn from the entire solution pool. This hybridisation may lead to fitter solutions while requiring far fewer total solutions be produced.

The intra-layer fitness matrix, comprising the regions between each of the modelled discontinuities, for the fittest reconnection layer model is presented in Table 4.6. It was this set that was used as the basis for the BVSR analysis presented in §4.2.2.

Event 2: 10:58UT

Using the structure produced using the static analysis in 3.3.3, the resultant values and limits were used as the initial state for the RLDS genetic algorithm. The variable

Variable	A-S	S-C	C-$\tilde{S}$	$\tilde{S}$-$\tilde{A}$
B (FGM)	0.58	0.12	0.59	0.39
V (HIA)	0.52	0.31	0.36	0.40
N (HIA)	0.16	0.23	0.30	0.85
T (HIA)	1.07	0.82	1.65	1.60

Table 4.6: A breakdown of the fitness values for each variable using the best RLDS set for each discontinuity during the 10:50UT crossing observed by spacecraft 3.

set used was the HIA variable set (B (FGM), V N T (HIA)), and the system was used to generate a standard pool of 100 solutions. The number of generations it took for each solution to "settle" was recorded, in this case the mean number of generations required was 60, the distribution was comparatively wide, however with $\sigma \approx 20$. The temporal distribution of these solutions was compiled in histogram used 1 second wide bins, the result can be seen in Figure 4.4.

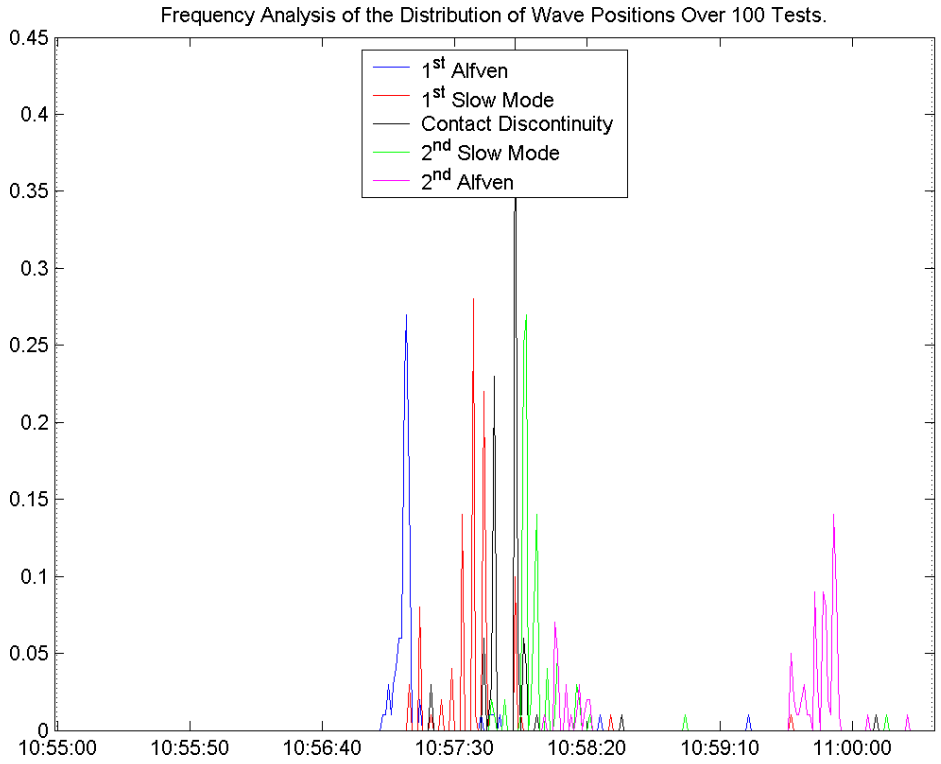

Figure 4.4: Histogram frequency analysis, using 1 second bins, of the temporal distribution of discontinuities arrived at through RLDS using spacecraft 3 data at 10:58UT on 3rd December 2001.

Applying the group reduction process to this solution pool with an inter-solution

tolerance of 6 seconds lead to 17 non-singleton groups being found. The 5 most populous groups accounted for ≈ 62% of the solutions, see Table 4.7. The high proportion of clustered solutions would suggest a comparatively well defined minimum. Whether this minimum is local or global can only be seen by comparing those groups to the fittest solutions found. In this case, this tight grouping was produced by the latter 4 groupings being identical copies of a single merged group. This is a failing of the grouping algorithm that was only addressed in the latter stages of the study.

	Percentage		Fitness		
Group Number	Grouped	Total	Magnetic	Plasma	Total
1	10.67	19	2.87	99.35	102.22
10,26,33,40	10.11	18	2.86	95.39	98.25

Table 4.7: The percentage occurrence of the structural groups calculated during the RLDS tests. The Grouped, value denotes the percentage occurrence in comparison to the total population that was grouped, i.e. non-single occurrence structures. The Total value is the percentage occurrence of that structure with respect to all tests carried out.

Comparing the total fitness of the best group solution (97.60) with the total fitness of the best single solution (95.96) we see again that although the group approach may be useful in classifying solutions arrived at, it does not produce the fittest solutions on its own. As such, it was the single solution structure values that were used in the BVSR analysis in §4.2.2.

4.2 Analysis Through BVSR Modification

4.2.1 ASCSA Type: 1st April 2003

Event 1: 02:27UT

As the basis for this BVSR analysis the initial sampling ranges from the first-pass simulation and the timing structure that was calculated using the RLDS algorithm in section §4.1.1 were used. The sampling ranges ran between 02:23:00UT - 02:25:00UT before the transition and 02:28:00UT - 02:31:00UT after it. The calculated discon-

tinuity structure that was used as the basis for the BVSR genetic algorithm is reproduced in Table 4.8.

Wave Mode	Time Position (UT)
1^{st} Alfvén Wave (A)	2:25:58.327
1^{st} Slow Shock (S)	2:26:22.773
Contact Discontinuity (C)	2:26:26.598
2^{nd} Slow Shock ($\tilde{S}$)	2:27:19.144
2^{nd} Alfvén Wave ($\tilde{A}$)	2:27:34.977

Table 4.8: The temporal position (UT) for each of the 5 modelled MHD discontinuities calculated using RLDS analysis for the event at $\approx$ 02:27UT using spacecraft 3 data.

Each completed BVSR process produced a single set of sample ranges for the boundary values used as the initial input conditions into the reconnection layer algorithm. The entire test generated a total of 100 possible solution sets. This number of sets was decided beforehand and is an arbitrary value. This value was selected in order to provide enough sets to suggest a representative sample of the total distribution. For a large set, such as this, it is then possible to classify the distribution in terms of its coherence with respect to the final, fittest, solution and introduce a measure of how many solutions must be generated before the fittest solution can be said to have been located. These statistics are dealt with in the collative overview in §6.1.6.

The distribution of solutions in this case is as a simple, well defined group. As such there is no need to consider alternate groupings or topological features. The non-boundary fitness values for the solutions produced ranged from 11.29 to 11.66. The structural factors that related to the model created using these intervals were 0.67 and 0.72 for η and $\tilde{\eta}$ respectively. These suggest a stable ASCSA type structure. The value for $|\mathbf{b}|$ contributes further evidence for this structure. For this model $|\mathbf{b}|$ was calculated to be 1404.47. This is close to but not over the ARCSA threshold that was calculated to be at 1444.15. The fitness matrix resultant from the comparison of this solution to the observed data can be seen in Table 4.9, the comparison itself is presented in full in Figure 4.5.

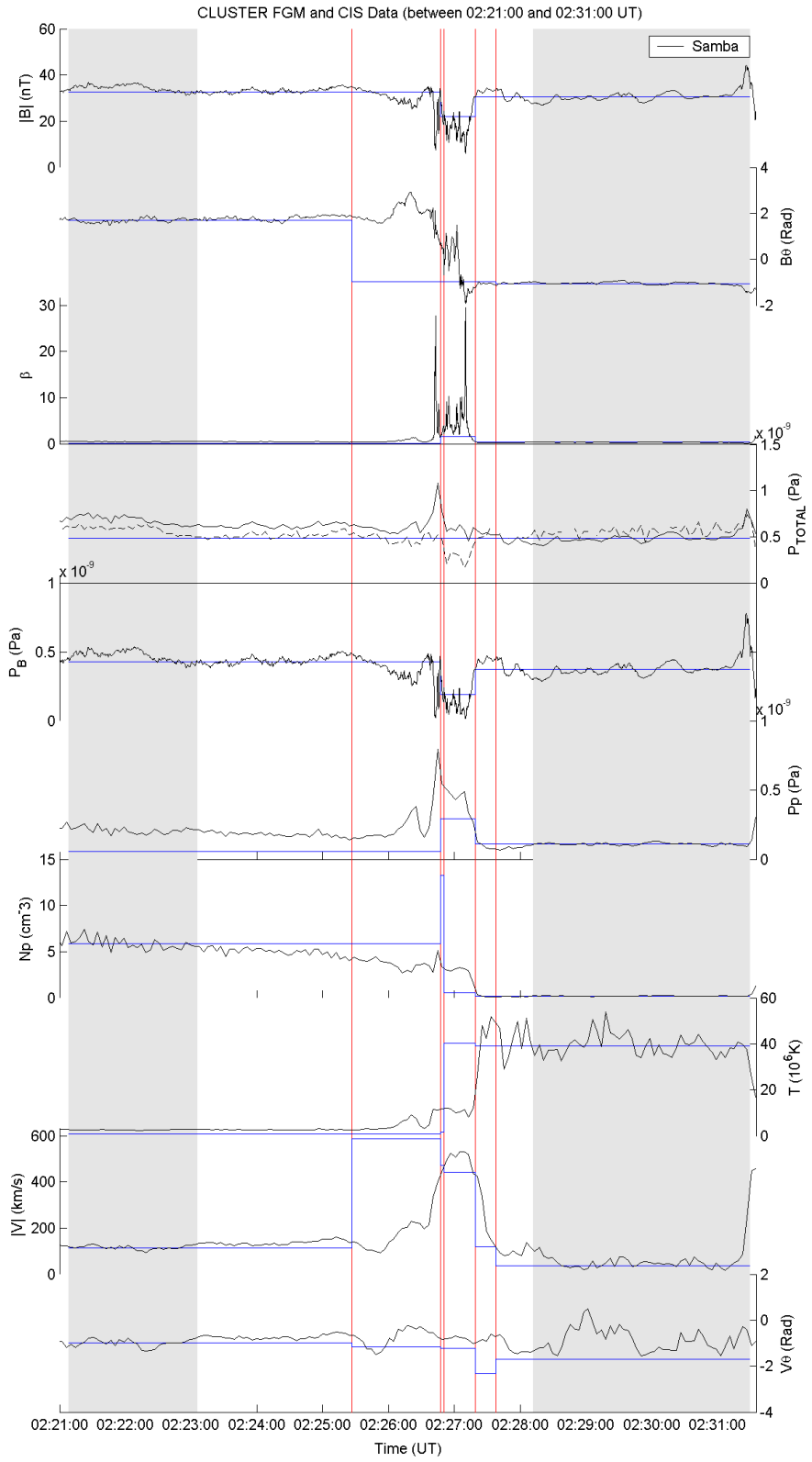

Figure 4.5: Comparative overlay of the reconnection layer model created by the simulation using the initial conditions previously specified for all magnetic and plasma variables. Data recorded by spacecraft 3 is presented in black, modelled in blue, the discontinuities are marked by red vertical lines and the ranges used for boundary condition sampling are shown in grey.

Variable	A-S	S-C	C-$\tilde{S}$	$\tilde{S}$-$\tilde{A}$
B (FGM)	0.75	0.77	2.11	0.39
V (HIA)	0.74	0.02	0.03	0.10
N (HIA)	0.17	0.90	2.37	0.16
T (HIA)	0.24	0.11	0.15	2.29

Table 4.9: The fitness values for the tested variables in the regions between each of the modelled discontinuities using the best RLDS and BVSR set for each one during the 02:27UT crossing observed by spacecraft 3.

Event 2: 02:35UT

Using the structure derived from the RLDS analysis the initial state for the BVSR algorithm was constructed. The initial sample range limits were those specified in the original, first pass analysis, and the discontinuity layer structure was as follows.

Wave Mode	Time Position (UT)
1^{st} Alfvén Wave (A)	2:35:58.864
1^{st} Slow Shock (S)	2:36:11.04
Contact Discontinuity (C)	2:36:14.98
2^{nd} Slow Shock ($\tilde{S}$)	2:36:22.97
2^{nd} Alfvén Wave ($\tilde{A}$)	2:36:26.133

Table 4.10: Discontinuity positions in time (UT) after RLDS analysis for the event at $\approx$ 02:35UT using spacecraft 3 data.

Using this information, 100 possible solutions were generated by the BVSR algorithm. These solutions, when analysed, display a two-tier nature. In 95% of the solutions produced the fitness value was clustered comparatively tightly between 160 and 170. However in 5% of the cases a second such grouping was clear in the 70-80 range. This smaller group shows a significant improvement in numerical fitness over the larger. The feature that all of those members of this second, fitter, group display is that they all have the pre-layer period limits set earlier than their less fit counterparts. The maximum ranges for the two groups are in Table 4.11. The post-layer sampling takes place over similar ranges that overlap to a significant degree. The pre-layer sampling however takes place in ranges that are significantly different and do not overlap at all. These periods have been plotted as shaded areas in Figure 4.6. These two groups of solutions have been designated with the numerals I and II for the earlier and later sets respectively for ease of referral.

Population	Pre-Layer Limits	Post-Layer Limits	Mean Fitness
5% (Group I)	02:34:08-02:34:26	02:36:31-02:37:05	72.94±0.16
95% (Group II)	02:34:55-02:35:15	02:36:30-02:37:33	162.74±0.23

Table 4.11: Contrasting pre and post transition layer sampling ranges for the two fitness groups evident in the BVSR solution analysis for spacecraft 3 data at 02:35UT. All time values are in Universal Time (UT).

The two highlighted periods contain fundamental differences in the observed variables. Both groups seem to have been regressed in time into an earlier portion of the transition layer. Examining the data for the entire interaction, beginning at 02:31:30 the spacecraft seems to have made successively deeper incursions into the transition layer before being returned to its previous environment. As such, the transition at 02:35 seems the most complete and has the lengthiest post-transition period. The group I boundary range is in a region that is similar to that after the transition layer, the group II one is situated approximately 30 seconds before the input sampling range where the variables are slowly changing, after an initial jump, to the stable originally identified pre-layer conditions.

Variable	Group	A-S	S-C	C-$\tilde{S}$	$\tilde{S}$-$\tilde{A}$	Total
B (FGM)	I	0.34	0.39	6.15	0.69	7.58
	II	2.83	1.90	3.04	0.74	8.50
V (HIA)	I	0.31	0.18	0.24	0.29	1.00
	II	0.31	0.20	0.35	0.32	1.19
N (HIA)	I	2.00	0.69	0.44	0.36	3.49
	II	1.13	0.29	0.24	0.39	2.00
T (HIA)	I	0.33	0.27	0.50	1.00	2.10
	II	3.26	2.18	3.23	1.03	9.69

Table 4.12: A comparison multi-variable fitness value breakdown using the best RLDS set for the best Group I solution from the BVSR algorithm during the 02:35UT crossing.

In examining the wave-interval fitness breakdown information in Table 4.12 many of the values are, for the most part comparable. Strong differences in value seem to have been present in the magnetic field where greater accuracy in the third wave-interval (in Group II) was traded for a greater improvement in the first two (in Group I). The primary causal factor for this change seems to have been the Temperature. The reduction of inaccuracy across the first three intervals leads to a model-wide

decrease in the total fitness of over 78%. There does not seem to have been a significant decrease during the 4th interval. A reason for this may be that due to the way the assumption of the conservation of total pressure is applied across the layer, the value that is dependent on the boundary conditions to the highest degree is the second Alfvén wave. The behaviour of the model during the 4th interval is provided by the equations describing this discontinuity.

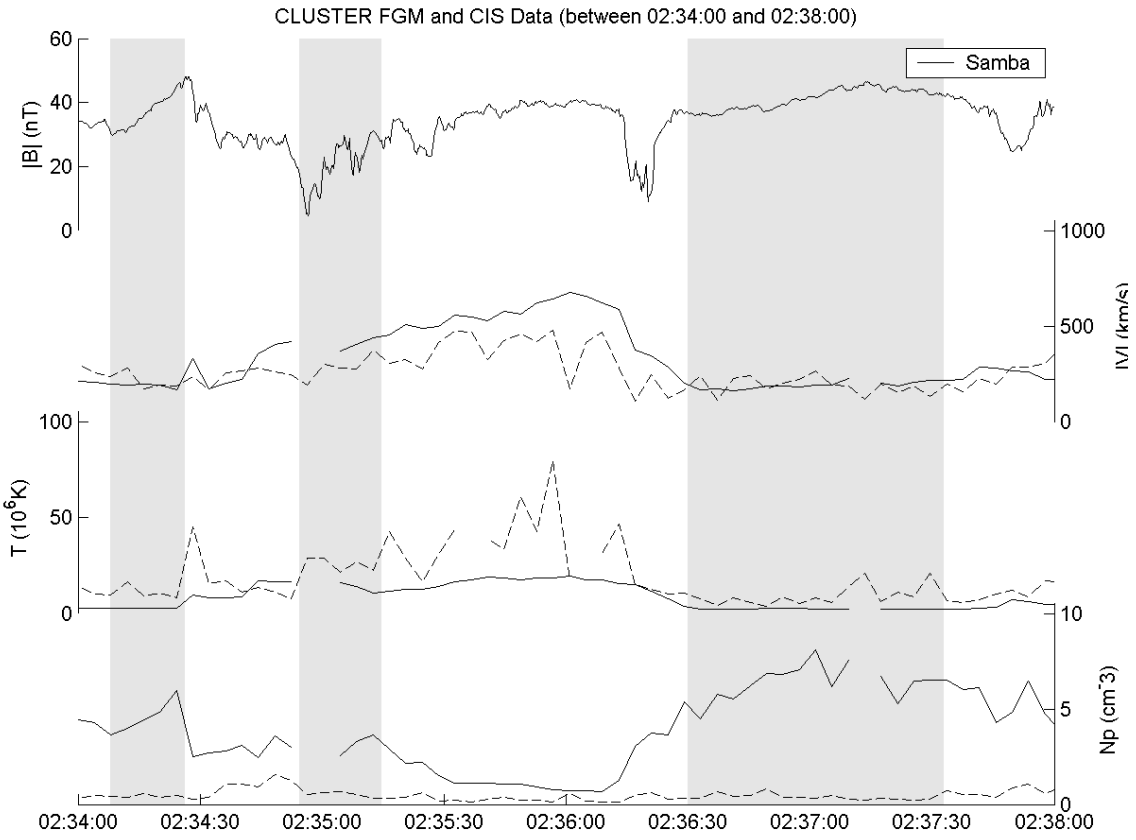

Figure 4.6: State variable overview for the transition at 02:35UT highlighting the higher fitness (left) and lower fitness (middle) groups of pre-layer solutions in addition to the compiled range for both groups of solutions in the post-layer (right) region.

Each of these two groups were tested for any correlation between the length of the sampling intervals used and the fitness of the model as a whole. In the group I case there is a strong correlation between the size of the post-layer sampling range and the fitness of the result, C=0.98, with a positive gradient ($\nabla = 0.59$) suggesting that shorter intervals give more accurate representations of the underlying variable behaviour.

The number of generations for each of the 100 solutions to reach the located minimum was recorded. When corrected for the 10 generation settling check time the results are such that the mean settling time, in generations, is 23±10. The distribution of settling times can be seen in Figure 4.7. In this diagram the primary feature is the strong peak around the mean. There is, however, a high-value tail above this feature that contains enough samples (≈ 26%) to alter the statistics significantly.

The evolutionary path for each of the solutions was not, at this time, recorded so it is difficult to say with certainty what the precise causes of this tail might be. A possible reason might be that since the initial state of the system is entirely random and the fitness landscape may not be, in all places, a simple funnel, that there may be locations that display local minima or regions of low fitness gradient. These areas would then be navigable, in the mathematical sense, but add an overhead to the number of generations taken to find the global minimum. This may be resolved with the introduction of methods that allow the selection procedures to be more aware of the features of the local fitness landscape.

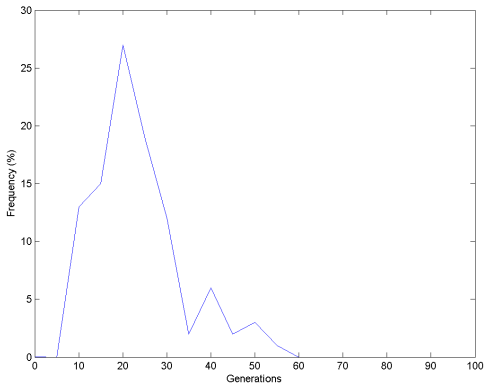

Figure 4.7: Frequency histogram of the settling time of solutions produced through the BVSR algorithm.

4.2.2 ARCSA Type: 3rd December 2001

Event 1: 10:50UT

The structure resulting from applying the RLDS algorithm (Table 4.8) was then used as the basis for the BVSR algorithm. The standard pool of 100 sampling range solutions was produced. The total, boundary inclusive, fitness values of these solutions were the considered in terms of any relation between interval length and overall fitness. Minor correlations were observed, the strongest being between post-layer interval size and total fitness. This positive correlation ($\nabla \approx 0.51$), while suggesting that shorter intervals tended to produce fitter solutions, was not considered strong as the correlation coefficient was only 0.72.

Wave Mode	Time Position (UT)
1^{st} Alfvén Wave (A)	10:49:11.43
1^{st} Slow Shock (S)	10:49:23.45
Contact Discontinuity (C)	10:49:27.33
2^{nd} Slow Shock ($\tilde{S}$)	10:50:24.01
2^{nd} Alfvén Wave ($\tilde{A}$)	10:50:31.28

Table 4.13: The temporal position (UT) for each of the 5 modelled MHD discontinuities calculated using RLDS analysis for the event at $\approx$ 10:50UT using spacecraft 3 data.

The fitness vs. interval plots for this solution pool did not, as has been seen in other cases, display a two-tier structure. All fitness values were clustered in a comparatively small range between 19.86 and 22.67, boundary values inclusive. As such, deciding the sampling range set to use was based on using a simple comparison of intra-layer, boundary value exclusive, fitness. From that comparison a single solution was found with a total fitness value of 8.68. This is a significant improvement over the 9.26 from the RLDS alone. The pre-layer interval spanned 10:46:16.1 to 10:46:47.3 UT, and the post-layer interval was from 10:51:41.1 to 10:52:10.7 UT. The non-boundary fitness matrix for this transition using both RLDS and BVSR solutions is given in Table 4.14.

The η values for this set were 0.95 and 0.78 for the first and second slow mode waves respectively. The value of $|\mathbf{b}|$ was 1442.64, with region II and region III $|\mathbf{b}|$

Variable	A-S	S-C	C-$\tilde{S}$	$\tilde{S}$-$\tilde{A}$
B (FGM)	0.80	0.12	0.60	0.14
V (HIA)	0.57	0.32	0.38	0.13
N (HIA)	0.11	0.24	0.31	0.22
T (HIA)	0.67	0.57	1.21	2.31

Table 4.14: A breakdown of the fitness values for each variable using the best RLDS and BVSR set for each discontinuity during the 10:50 UT crossing observed by spacecraft 3.

limits of 1353.53 and 1857.74 respectively this is actually classified in terms of the ARCSA structure type even though the η values suggest, albeit not in a robust fashion in the case of the first value, the presence of two slow shocks rather than one slow expansion fan and one slow shock. As the spacecraft was passing in from the magnetosheath into the magnetopause this suggests that it is the magnetospheric slow mode component that is in question. In this case, if simulation is tried assuming only a hydrogen plasma then the system resolves itself into the expected ARCSA structure with η values of 1.05 and 0.86. What is unclear at this time, due to the nature of the compositional data, is whether it is the heavy ion mass factors used in the simulation that are inaccurate, or the equations used to define the structure region boundaries. The compiled comparison between the model and observed data is presented in Figure 4.8.

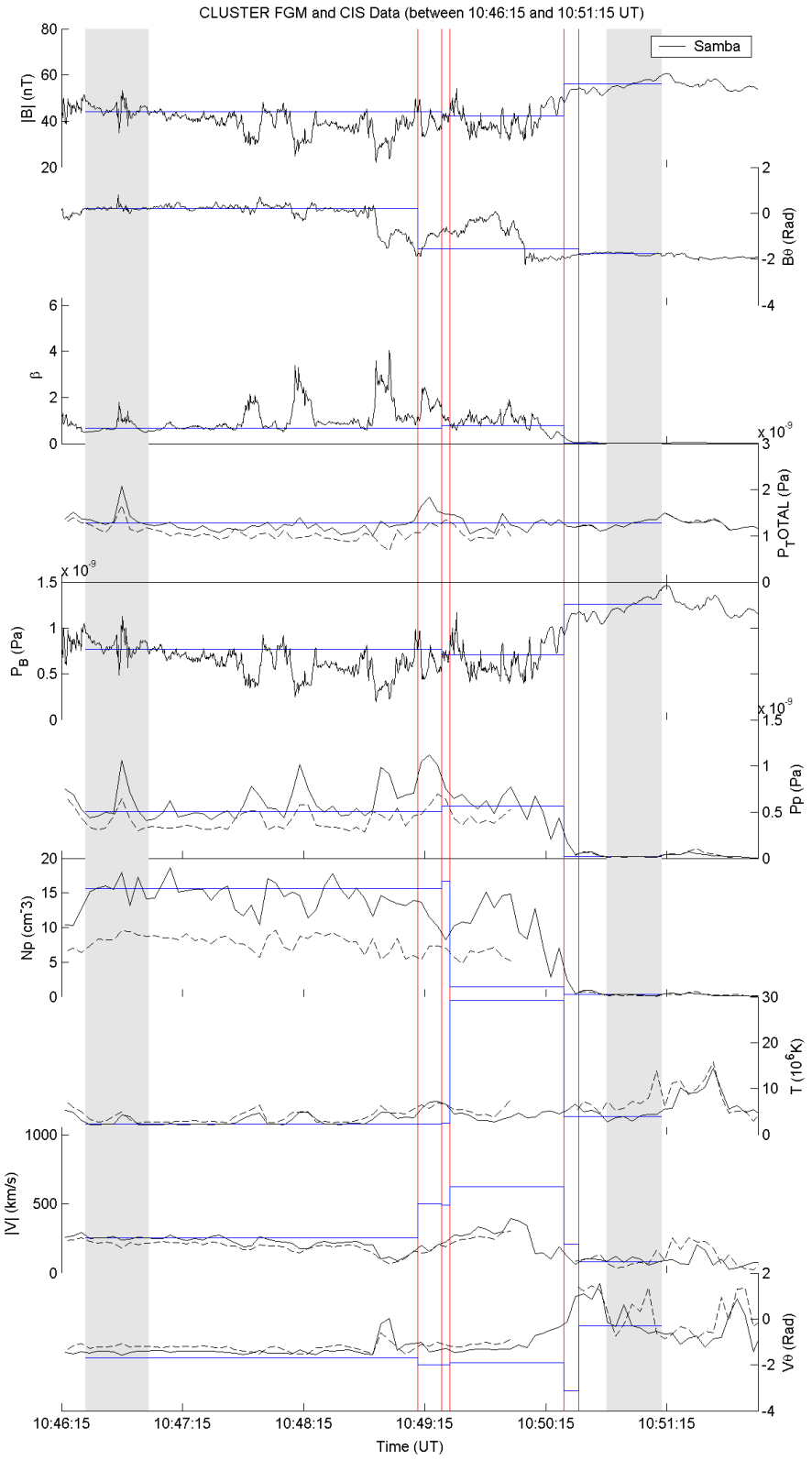

Figure 4.8: Comparative overlay of the reconnection layer model created by the simulation using the initial conditions previously specified for all magnetic and plasma variables. Observed data is presented in black, modelled in blue, the discontinuities are marked by red vertical lines and the ranges used for boundary condition sampling are shown in grey.

Event 2: 10:58UT

Using the structure derived in §4.1.2 using the RLDS method (Table 4.15) the BVSR algorithm was applied. The initial boundary sampling range was as specified in the first pass analysis in §3.3.3 and the evolutionary method was used to produce a standard pool of 100 solutions.

Wave Mode	Time Position (UT)
1^{st} Alfvén Wave (A)	10:57:02.64
1^{st} Slow Shock (S)	10:57:36.77
Contact Discontinuity (C)	19:57:52.78
2^{nd} Slow Shock ($\tilde{S}$)	10:57:56.74
2^{nd} Alfvén Wave ($\tilde{A}$)	10:59:49.13

Table 4.15: Discontinuity positions in time (UT) after RLDS analysis for the event at ≈10:58UT on 3rd December 2001 using spacecraft 3 data.

The solutions produced displayed a similar two-tier distribution as that seen in §4.2.1. In this case the proportion in the larger, less accurate group, was 98%. There were only 2 solutions in the smaller, fitter group and those solutions were clearly distinct from one another. All solutions retain similar post-transition sampling intervals. The pre-transition intervals are where the primary divergence takes place. One of the two fitter solutions may be considered an intermediate, or bridging, solution set as it retains similarity with the main group on 3 of the 4 sampling range values. The pre-layer sampling range start point differs significantly with the main group, however, and led to a improvement in fitness of $\approx$ 26%. The minimum solution has a significant change in both pre-layer sampling limits and leads to a fitness value over 30% less than the best solution in the main group. Using the Groups I & II nomenclature from the earlier cases, the intra-layer fitness comparison was carried out using the fittest solution from the largest group (Group I), the intermediate solution and absolute fittest solution found (Group II).

Using this data it is possible to see that accuracy in terms of the magnetic field data has been traded for larger improvements associated with the bulk velocity and temperature variables. The total fitness has improved. Bulk velocity and Temperature are two of the variables that are less well described by this particular model.

Variable	Group	A-S	S-C	C-$\tilde{S}$	$\tilde{S}$-$\tilde{A}$	Total
B (FGM)	I	0.17	0.72	0.41	0.78	2.08
	Inter	0.61	3.40	3.37	0.79	8.16
	II	0.25	2.60	2.43	0.81	6.09
V (HIA)	I	0.12	1.13	0.65	0.45	2.33
	Inter	0.13	0.41	0.19	0.39	1.12
	II	0.21	0.54	0.28	0.42	1.44
N (HIA)	I	0.15	0.33	0.04	0.33	0.85
	Inter	2.93	5.21	1.62	0.29	10.05
	II	1.32	3.66	1.09	0.27	6.34
T (HIA)	I	1.81	16.83	7.40	1.51	27.55
	Inter	2.08	3.87	1.62	1.47	9.04
	II	2.91	5.37	2.29	2.11	12.68

Table 4.16: A comparison multi-variable fitness value breakdown using the best RLDS set for the best Group I solution from the BVSR algorithm during the 02:35UT crossing.

This may be a candidate event either for the exclusion of particular variable sets based on their inaccuracy, or for considering the limitations of this model in this type of case. Including all variables necessarily leads to the system prioritizing numerical optimization at the cost of morphological coherence.

Examining the solutions for correlations between interval size and fitness, the same positive correlation is confirmed. Larger intervals produce higher the final fitness values. The highest correlation coefficient calculated, in this case, is for the relation between the pre-layer interval size and the fitness with a value of $\approx$0.65. This is not a strong correlation. It does, however, lend evidence towards the presence of this being a general behaviour seen in all analysed cases.

A comparison of the calculated structure with the observed data is given in Figure 4.9.

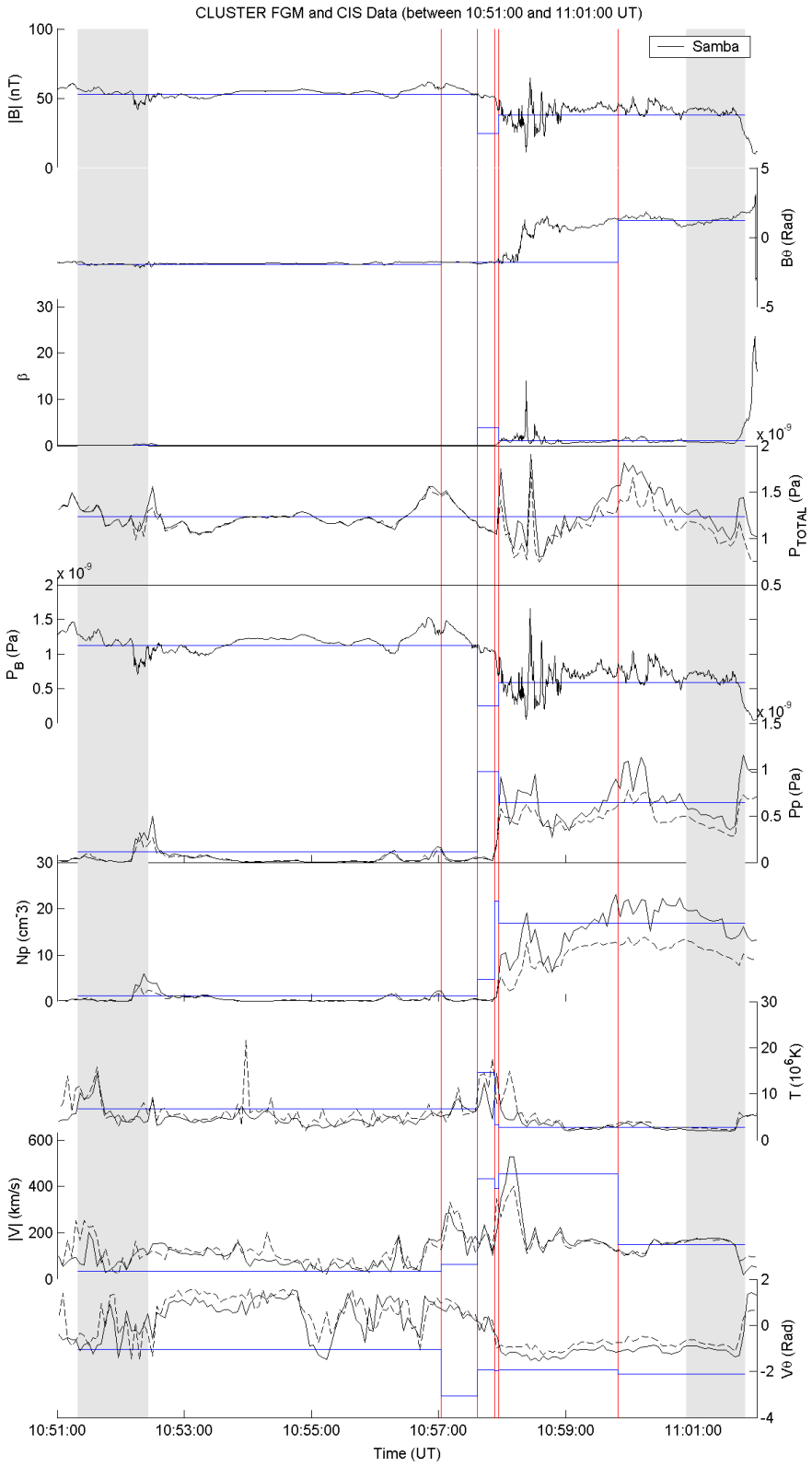

Figure 4.9: A comparative overlay of the reconnection layer model created by the simulation using the initial conditions previously specified for all magnetic and plasma variables. Observed data is presented in black, modelled in blue, the discontinuities are marked by red vertical lines and the ranges used for boundary condition sampling are shown in grey.

Chapter 5

Summary of Case Studies

In this chapter will be presented a summary of the results of each of the analyses on a quantitative basis using the fitness calculations inherent to the Genetic Algorithm approach. The initial fitness value is based on the first-pass simulation structure generated for each case that was described in §3. This structure is then fitted, by eye, to the morphology of the crossing data as it has been observed by the CLUSTER satellite used in that analysis. RLDS fields will then present fitness values after the same structure has been mathematically matched to the crossing data in a fashion that removed the arbitrary nature of by-eye fitting. BVSR/Final values are generated using the resultant RLDS structure and the modified sampling range indexes produced by this method. The three stage method was selected as it is then possible to evaluate, by looking at the trend in the fitness values generated at each stage, both whether the initial model was accurate in addition to whether the two algorithmic methods contributed to an improvement in that accuracy.

5.1 Summary by Structural Type

Date/Time (UT)	Spacecraft	Initial By-Eye	RLDS	BVSR/Final
Type I: ACA				
No crossing that I analysed as part of this project was identified as belonging to this structural type.				
Type II: ASCSA				
03/07/01 05:37:50	3	17.43	15.74	7.90
03/12/01 10:50:00	3	11.60	9.26	8.98
01/04/03 02:27:00	3	11.51	10.91	11.29
01/04/03 02:36:00	3	26.55	19.20	14.17
Type III: ARCSA				
03/12/01 10:58:00	3	68.07	34.34	27.50
20/02/02 13:59:00	1	20.63	10.02	9.77
20/02/02 13:59:00	3	27.09	15.68	10.11
20/02/02 13:59:00	4	11.97	6.47	5.83
Type IV: ARCRA				
03/07/01 05:37:50	1	13.86	11.58	11.10

Table 5.1: Compiled results for all events analyses in each of the pre-defined structural types.

5.2 Summary by Spacecraft

Date/Time (UT)	Type	Initial By-Eye	RLDS	BVSR/Final
Spacecraft 1: Rumba				
03/07/01 05:37:50	IV	13.86	11.58	11.10
20/02/02 13:59:00	III	20.68	10.02	9.77
Spacecraft 3: Samba				
03/07/01 05:37:50	II	17.43	15.74	7.90
03/12/01 10:50:00	II	11.60	9.26	8.98
03/12/01 10:58:00	III	68.07	34.34	27.50
20/02/02 13:59:00	III	27.09	15.68	10.11
01/04/03 02:27:00	II	11.51	10.91	11.29
01/04/03 02:36:00	II	26.55	19.20	14.17
Spacecraft 4: Tango				
20/02/02 13:59:00	III	11.97	6.47	5.83

Table 5.2: Compiled results for all events analyses for each of the spacecraft, listed in numerical order.

Chapter 6

Discussion

6.1 Overview of Methods

6.1.1 Boundary Normal Methods

The methods used to derive a normal vector for the purposes of constructing the boundary normal coordinate system were, a model normal, the Tangential Discontinuity Method and Minimum Variance Analysis.

The model normal method was used primarily as a guide, and primarily used the Shue 1997 (Shue et al., 1997) and Sibeck 1991 (Sibeck et al., 1991) models of the magnetopause. These models have the benefit that they are comparatively easy to both construct and apply. For many of the situations encountered, these models were effective and efficient. However, these models do not, directly, reflect the magnetic field structure of the dayside magnetopause which they represent using spherical sections. Instead they are used to create smooth surface models at the extent of the magnetopause boundary. This means that they are not as applicable to regions where there is significant topological complexity, for example, the cusp (§3.2). This type of case requires the use of models that describe the magnetic field itself rather than the surface of the magnetopause (Tsyganeko, 1996).

The Tangential Discontinuity (TD) method (Paschmann and Daly, 1998) has, due to its initial construction assumptions (anti-parallel field orientations on either

side of the field discontinuity), limited applications to situations where the field shear is comparatively low. The quality of a coordinate system defined using this method is difficult to check internally as it does not support a quality factor value in the same way as the Minimum Variance Analysis methods do. It is, however, a good initial guide and often produces normal vectors that are of comparable accuracy to those produced by MVA. The strength of this method is that, when applied to cases where there is comparatively little variance in the pre and post layer regions from which the initial magnetic field vectors are compiled, it is effectively interval invariant.

Minimum Variance Analysis is a complimentary method to the TD method as it is most effective when the magnetic field orientations are not anti-parallel, i.e. when the magnetic rotation is less that 180 degrees. In fact as long as the eigenvectors produced are sufficiently separated ($Q >> 1$) then the accurate applicability is high. It is important to remember that without using the $B_N = 0$ constraint there will be a normal component to the trans-boundary magnetic field, a guide field. It is possible to specify a non-guide field geometry ($B_N = 0$) by using the equations specified in (Paschmann and Daly, 1998) and (Paschmann and Daly, 2008) or the methods described therein suggested by Siscoe. et al. in 1968. In this case the Siscoe method results often tended towards an intermediate vector between that provided by the TD method and unconstrained MVA.

6.1.2 Reconnection Signatures: Fluid

The methods applied to classifying the fluid signatures of reconnection were the de Hoffmann-Teller analysis (§2.2) and the Tangential Stress Balance, or Walèn Relation, test (§2.5).

In context, the methods applied were in their simplest form. They did not include effects relating to the possible acceleration of the de Hoffmann Teller convective frame, as described by Khrabrov and Sonnerup in (Paschmann and Daly, 1998), or pressure anisotropies in the Walèn test, although heavy ion composition factors

were accounted for. These methods were used as a confirmator of the presence of reconnection in an event already subject to this analysis rather than as an attempt to prove the existence of reconnection during a new and not previously studied period. In both cases adequate confirmation was gained through their use and as such their employment can be considered successful.

6.1.3 Reconnection Signatures: Particle

Particle signatures of reconnection were confirmed by the examination of phase-space velocity distributions in light of data described both the magnetopause normal and possible de Hoffmann-Teller frames, from both the CIS-CODIF and CIS-HIA instruments, for structures conforming, as in §2.4, to transitive ion populations and distribution selected Cowley-D Distributions.

In general good agreement was found between the appearance of these structures and with the results of other tests, such as the tangential stress balance (Walèn relation) test, designed to highlight the signatures of reconnective processes.

6.1.4 Petschek-Type Reconnection Layer Model

The Petschek model, although remaining somewhat controversial, has been applied with some success in the past to in situ observational data (Rijnbeek et al., 1989; Rijnbeek, 1992). In the cases studied here, a structurally similar model has shown, even in its unoptimized state, significant morphological coherence with the data.

As the model is only two-dimensional and uses infinitesimally thick discontinuities it does not include factors such as the finer structure of the MHD waves, wave mixing and particle species effects due to different masses. This leads to an inherent inaccuracy that future developments of the model are hoped to lessen.

6.1.5 Reconnection Layer Discontinuity Spacing (RLDS)

In applying RLDS to these cases, it has been found that all solutions the method produces are valid and fit the data. This latter part is important because in fitting

the data in a mathematical and non-arbitrary fashion, the structure produced may have some physical meaning beyond just being a useful way to distribute the discontinuities in this model. The spacing of the discontinuities in the time series of the satellite data, combined with the motion of the spacecraft and the motion of the magnetopause boundary, calculated through de Hoffmann Teller analysis (§2.2) or other method such as the Constant Thickness, Constant Velocity or Discontinuity Analyser methods (Paschmann and Daly, 2008), can be used to give values for the spatial extent of the reconnection layer. However, these values must always be considered in the light of the nature of the model and methods used to produce them.

One of the primary limitations of this method, in its current incarnation, is that the engine itself is not aware of the surrounding topology in fitness space. For example, a peak in a variable may arrest the evolution of the position of a discontinuity, even if, once on the other side, the mathematical fitness value would be far lower. This localisation of solutions is made more unlikely, by the random nature of the distribution of discontinuities in the initial state. It does not, however, completely prevent the system from finding local minima. The method that allows the highest expectation of producing the global minimum, is to carry out multiple evolutionary simulations for each event. The global minimum, should then be discovered as the solution to one of these tests. The system is, if a structure is not specified, in a random initial state and therefore the due to the nature of its evolution, the global minimum solution may not be the first one that is defined, or even the 100th. This limitation could overcome during future development by applying optimization methods such as Differential Evolution or Particle Swarm Optimization.

What can be seen from a histogram analysis of the maximum numerical separation between discontinuity layer structures using magnetic field and ion data is that it shows peaks of discontinuity positions at approximately 4 second separation. This effect is a result of the discrete nature of the measurement time series, and is comparable to the numerical resistivity observed in grid based MHD simulations.

The algorithm to calculate the fitness of a wave-timing structure does so using the values provided at discrete data points, rather than a continuum. This results in different variance values appearing either just before or just after an ion time sampling point, not between them. Future methods to attenuate this effect might rely either: on data with higher sampling rates, or through improvements to the way the Fitness is calculated.

The Grouping method of analysing RLDS algorithm solutions was introduced to highlight solution regions through analysis of the temporally dispersed raw solutions. Merging solution sets into meaningful groups and resolving possible multi-group members proved to be complex. In each of the presented cases, multi-group solution sets were encountered, which precluded the collection of clear results. The high populations observed within the groupings constructed suggest, however, that with more effective analysis they may be useful in classifying event solution structures in the future.

The future generational efficiency of solutions created using the RLDS algorithm could be improved by allowing the hybridisation of solution sets, as described in brief in §4.1.2. If the generated solution sets are examined for the most effective single solution for each discontinuity, then the compilation of these values may lead to a single, fitter, solution. This extension to the method may also provide a way of maximising the efficacy of the process while decreasing the required number of algorithm iterations. To be computationally feasible in the case of a large solution set pool, a reduction method, such as solution grouping, may need to be applied before the hybridisation stage, due to the large number of discontinuity position possibilities to be evaluated.

6.1.6 Boundary Value Sampling Range (BVSR)

Boundary value sampling was carried out in two phases. The early section of the testing was carried out without using any constraint on the type of solution produced. The system would then evolve towards the best, numerical, comparison of

model and observation. What was found, was that the system tended to evolve from the, originally input, longer sampling range towards a shorter one. A comparison of the total original sampling range (both pre crossing and post) to that which produced the most similar model/observation pairing was considered, an example of this is one case on 1st April 2004 where the original sampling range spanned some 36.2 seconds. The eventual result was an interval of only 6.0 seconds, a reduction of over 80%.

The reduction in these values was significant and widespread. All events analysed for this trend showed some sign of it. As multiple solutions were produced for each event it was possible to look, statistically, at the fitness of the solutions produced with respect to the properties of the intervals that gave rise to those solutions. Initial scatter plots of each interval set were produced. To the raw sets, derived sets covering the Minimum and Maximum Intervals, Mean Interval and Summed Intervals were added. All of the sets were also subject to linear least squares fitting, correlation coefficient and correlation significance tests. In many of these a null result was found. However, across the board a weak correlation was highlighted between total sampling interval and the fitness of the model. An inverse proportionality. Generally, the longer the interval sampled over the less well the model constructed using those values fit the data.

If this was present in only a single case, or even a structural class of cases, it might be a function of the local conditions or the specific equations used to model that layer. The correlation was present, however, in many of the tests carried out. Two possible explanations for this behaviour might be:

1. There is something inherent to the model or genetic algorithms that favours small sampling ranges.

2. That the model is attempting to evolve towards a minimum in the fitness landscape that is not represented in the data and so finds the closest point to that minimum.

If an internal bias towards shorter sampling ranges is inherent to the BVSR method, in its current form, then it occurs as an emergent property. Analysis of the system for evidence of this emergent behaviour could be carried out using a modified data set for a reconnection layer transition. The data for the transition would be constrained, such that the plasma parameters in the pre and post-layer sampling regions would be constant. If the algorithm is not biased towards short range selection then the initial solution should not evolve as, due to the interval invariance of fitness statistics, all sampling ranges will be mathematically identical and so all "genes" will have equal fitness. Any evolution of this system would be evidence of a length based criterion, the identification and removal of which would be of primary importance in any future use of the BVSR method.

This analytical reconnection layer model was constructed using ideal MHD, as a theoretical basis, and assumptions used to simplify the geometry. The limitations placed upon the model by these choices preclude it, even if theoretically perfect input parameters were used, from any expectation of complete accuracy in its description of an event. Computationally, these limitations result in the constraint, that the calculated fitness value for any modelled structure produced by the genetic algorithms cannot be zero.

The core function of the genetic algorithms is to modify the parameters relating to the model to minimise mathematical divergence of the model from the observational data. The input parameter set that leads to the best fitness value is not guaranteed to be scientifically meaningful, since a single point observation is just as valid, numerically, as a more representative set supplied by the region adjoining the layer. Because of this, a limit on the smallest size of a valid sampling range had to be applied during this study, to remove the possibility of unphysical results that nonetheless fit the mathematical criteria.

Future use, especially autonomous use, of the BVSR method should be carried out alongside an empirical study of the crossing data. This empirical study would focus on identifying physically significant values for the minimum and maximum

limits on the BVSR range modification.

Those details are tied closely to the model and not the BVSR method itself. In evaluating the efficacy of the method we need only evaluate whether there is any improvement in the model to observation comparison. If there is, the degree to which there is an improvement needs to be quantified, and possible flaws need to be identified, described and solutions need to be suggested.

The numerical fitness system described for general use in the genetic algorithms, in §2.7.1 and §2.7.2, has been used as the basis for comparatively quantifying the effect of the BVSR method. This choice was made, at the time, because the calculated values are effectively unitless and dependent only on the divergence of the model from the CLUSTER instrument data. Later re-examination of the original methods used in calculating the fitness values has concluded that an approach based on the direct combination of the variance for each variable is likely to provide more representative and intercomparable results.

The summary in §5 for the four events presented in full in §3, shows non-boundary fitness value reductions of 3%, 20%, -4% and 26% respectively from the RLDS values. From these results it can been seen that, generally, the BVSR method does improve the model to observation coherence. The single negative value, an increase, is due to the manner in which the fitness value has been calculated. These values, within the algorithm, are calculated taking into account both intra-layer (decided by the model) and boundary range (calculated observed data only) accuracy. The boundary range component was added to ensure that the model did not evolve towards a state that, while giving the most accurate solution internally, ignored the position in the time series that solution occurs, i.e. it keeps it bounded in the layer itself. This component to the fitness value is examined during the iterative selection process but is not, however, examined when looking at the final fitness of the layer. It is therefore possible for a solution to the be fittest solution while including the boundary fitness values but actually lead to an increase in the fitness value (a loss of accuracy) once these have been removed. This case is, in fact, unique as each of the other cases

there is a significant reduction that seems to confirm that this method is applicable to this data, and may have wider applications to this system using other models or even other systems whose inputs are comprised of boundary condition value sets.

To examine the ability of the system to tend towards the global minimum value we can look at how the distribution of solutions changed with increasing total solution number. As any specific solution can occur in any position in the timeline, the sequence of solutions has no meaning in and of itself. As such, a bootstrapping approach was taken and resampling a certain number of solutions from the produced pool it was possible to describe the resultant behaviour in terms of the statistical qualities associated with a fitted gaussian probability distribution for a given sample size.

Sample Size	Distribution Mean	Mean Solution	
		$\delta\mu$ (s)	σ (s)
10	42306.5571	-0.1917±0.0258	7.7215±0.0182
20	42306.1107	-0.1771±0.0167	5.1161±0.0094
30	42306.4856	-0.1659±0.0115	3.9037±0.0085
40	42306.4431	-0.1648±0.0103	3.1400±0.0071
50	42306.3156	-0.1598±0.0075	2.5635±0.0056
60	42306.3741	-0.1607±0.0062	2.0926±0.0045
70	42306.4174	-0.1586±0.0056	1.6781±0.0035
80	42306.3973	-0.1391±0.0038	1.2826±0.0027
90	42306.4117	-0.1084±0.0025	0.8531±0.0018
100	42306.5600	Sample Total so Not Applicable	

Table 6.1: A reproduction of an example set of solution comparisons by sampled solution set size for a boundary limit for the set created for the event at ≈02:27UT on the 1st April 2003.

The data in Table 6.1, although from a single case, is representative of the behaviour for all such analyses. It is easy to see that even with a low sample size (number of simulated solutions) the mean value for the fitted distribution very quickly tends towards the final mean value. In this case the initial $\delta\mu \approx 0.2$ which is approximately the same as the sampling time for only 4 magnetic field vectors at full time resolution, or in fact only one at the resolution used in these tests. An almost insignificant amount. Lower numbers of samples were tested and the results were

the same. This suggests that any simulation run that contains even a low number of members will provide an accurate picture of the nature of the final distribution quickly. This does not suggest that the mean for this distribution will be the global minimum. In the above case, the minimum solution found occurs at index value 42310, some 0.69 seconds away from the mean value. As such, it is important to note that an efficient use of this method is not to optimize the distribution but to produce the fittest single set of values.

This behaviour is underscored by the two-tier nature of some of the solution pools arrived at using this approach. The presence of these lends evidence to the hypothesis that while the model is incomplete (only 2-D, ideal MHD based and time independent) the fittest solution for the model may not actually exist in the input data. Thus, without limits these evolutionary algorithms will find the best match irrespective of where they find it. That said, in these cases it is primarily the pre-transition layer that shows the most variance and the highest tendency towards group division. I would suggest that the reason for this is that, in this model, the application of the conservation condition for total pressure means that subtle changes in the pre-layer range has a far larger effect than those in the post-layer region because the pre-layer plasma data is used to calculate the initial pressure on both sides of the layer, and thus the behaviour of much of the internal mechanics.

6.2 Overview of Results

The comparison of results can be split into its qualitative (morphological) and quantitative components.

Morphological matches between models and data are, by their nature, arbitrary to a degree. It is, however, useful to consider this information, especially in light of the natural simplicity inherent to the model used. Changes in a quantity or quantities across a modelled discontinuity that are of the right sense and approximately the right magnitude would suggest, even in the presence of only weak quantitative confirmation, that the feature modelled is physically similar to the one present. This

is an important distinction to make.

Qualitatively, through examination of the models produced with respect to the data they attempt to describe, it can be seen that, in general, the morphology of, and changes in, the observed magnetic field data are represented to a greater degree in the derived model structures than those observed in the plasma parameter data. Reasons for this may include, but not be limited to:

1. The assumption of total pressure balance across the layer that is used to calculate the temperature on the pre-layer side.

2. The increasing inaccuracy of the moment determination from the particle distributions when the number density was low.

Quantitativly it is important to examine the post-discontinuity fitness for each of the four active layers for each type, and then overall. The layer types encountered were the types II, III and IV being comprised of ASCSA (Table 6.2), ARCSA (Table 6.3) and ARCRA (Table 6.4) wave types respectively.

	Alfvén	Slow Mode	Slow Mode	Alfvén
Magnetic Field (B)	5.42	3.71	25.75	4.17
Bulk Velocity (V)	4.55	1.46	1.77	2.33
Number Density (N)	6.75	5.53	9.50	1.94
Temperature (T)	3.98	3.04	5.96	14.15

Table 6.2: Average percentage contribution to final fitness value for the ASCSA structure type.

	Alfvén	Slow Mode	Slow Mode	Alfvén
Magnetic Field (B)	0.68	1.50	8.36	26.03
Bulk Velocity (V)	0.66	1.80	0.91	3.88
Number Density (N)	0.76	2.16	0.20	3.87
Temperature (T)	6.97	28.08	12.13	66.22

Table 6.3: Average percentage contribution to final fitness value for the ARCSA structure type.

Examination of these values leads us to the early conclusion that the magnetic field data is, in fact, one of the least accurate quantities. In spite of the fact that qualitatively it seems to show the highest degree of morphological coherence. This

	Alfvén	Slow Mode	Slow Mode	Alfvén
Magnetic Field (B)	7.36	5.75	6.95	1.09
Bulk Velocity (V)	0.52	1.27	6.12	1.66
Number Density (N)	0.71	0.76	0.01	0.26
Temperature (T)	26.66	9.56	0.09	31.23

Table 6.4: Average percentage contribution to final fitness value for the ARCRA structure type.

is, I believe, due to the difference in temporal resolution. The temporal resolution for the plasma data is of the order of 4 seconds, whereas it is 0.2 seconds for the magnetic field data selected for use in this study. Assuming a normal pattern of variation in the variable we would therefore expect a far higher variance per unit time in the higher time resolution sample. A simple test of this was carried out; a 60 second period of "random" data was produced at the two different time resolutions using sampling from the normal distribution, as real physical observables might be. In the 60 second period 15 Ion Data samples would be collected and 300 Magnetic Field Data samples would be collected. The fitness of these sets, as previously defined, was calculated for each using the $y = 0$ line a as a "model" section, which is reasonable. The results were that the magnetic fitness value was higher by a factor of $\approx 20 \pm 0.07$. This is exactly the factor difference between the number of samples for each of the two types. As such, for the basis of inter-variable comparisons, magnetic field fitness values should be regarded as being approximately 20 times lower than they are. One effect that follows on from this is that the fitness values used by the algorithms in their current configuration as the basis for evolutionary selection are extremely sensitive to inaccuracy in the modelled behaviour of the magnetic field. This is not, inherently, a fault it just needs to be taken into consideration when designing the function conditions for the tests. Recalculating the raw values using a baseline of exactly 20 as a scaling factor it can be seen, in Table 6.5, that the magnetic field is, as we would now expect, the most accurately modelled of all of the observed variables, followed in order by the bulk velocity, number density and the temperature.

While this information tells us about the organisation of data within a model,

Variable	Average Contribution to Fitness
Magnetic Field (B)	3.1041
Bulk Velocity (V HIA)	16.067
Number Density (N HIA)	37.705
Temperature (T HIA)	43.124

Table 6.5: Comparative contributions to overall fitness values averages across all tests exhibiting the ASCSA structural type using a scaling factor of 0.05 on all magnetic field results.

it sheds little light on how effective that model is both in comparison to the data and to other models. Tables 6.2, 6.3, 6.4 relate information about inter-model and inter-structure comparisons and give absolute values for the efficacy of the models produced for each structural type.

Looking to characterize the different final fitness values of the events tested direct comparisons were made between the fitness of each event and different variables that may have had an effect. Examples of these variables are: the value of $|b|$ (the structural constant), the magnetopause normal velocity as measured in the deHoffmann-Teller frame (V_N) and the angular quantities calculated during boundary normal analysis that describe the orientation of the spacecraft with respect to the magnetopause. There are too few events to form the basis of an accurate statistical study, however, there are enough to suggest whether these are plausible. Of these V_N and the angular quantities are already in useful units with respect to an intercomparable frame of reference. The effect of $|b|$ is dependent on the local conditions as the transition points between structure types are calculated in each case, not set. A unitless ratio was constructed to meet this goal. Since the most populous structure types were the ASCSA and ARCSA types (Regions II and III) the transition point between the two was used and all $|b|$ values were then plotted as a ratio of their $|b|$ to the Region II/III limit. None of the above showed significant evidence of correlated behaviour, the correlation coefficient for a linear regression carried out on the $|b|$ data was only 0.5532. There may indeed be trends in fitness values but they are not clear from this data.

6.3 Conclusions

The results I have collected during this study suggest that this Petschek-type model of the reconnection layer can be applied, successfully within the bounds of the assumptions used in its creation, to modelling such layers and can be used to derive both structural and behavioural information about them.

The pre-simulation methods I have used are tried and tested approaches and have, in general, provided consistent and satisfactorily accurate results, within methodological and experimental bounds.

The simulation methods I have used, although in their simplest form, in this case, seem to provide meaningful information in a manner that is easily applied, comparatively fast in development, internally consistent and as a robust alternative to arbitrary selection.

Chapter 7

Conclusions

7.1 Overview of Study

9 events were analysed in detail, and each event was analysed in two stages. The first analysis stage was the pre-simulation analysis and comprised examination in terms of the event position, orientation and evidence of reconnection signatures in fluid and particle quantities. For the most part, this has been carried out with success, if in varying degrees, in the past, and was continued in this case using proven methods. The second, simulative, stage looked at model structure types, physical variable behaviour, inter-model fitness and absolute model fitness. This application to this data set in this fashion has not been attempted before.

Contextual features relating to this approach that were identified included:

1. The inherent simplicity of a single fluid, two-dimensional ideal magnetohydrodynamic model, and its incapacity to model finer structural features.

2. The nature of the evolutionary search methods and guaranteeing the location of the global minimum with a high degree of accuracy in a minimum of evolutionary iterations.

7.2 Final results

In considering the results as a whole it is important to remember that each of these sets of results exists, primarily, in comparison with each other. Since there is no defined measure mathematically and non-arbitrarily, in this study, for what constitutes a "good" fit, or in fact a "bad" one we are constrained to making statements about "better" or "worse". Comparison between models is possible, however, using the fitness values derived from their agreement with observational data. It is important to remember, while doing this, that these values are not solely dependent on the model itself but are also a reflection of local conditions and noise in the data.

The goal, of course, is to portray each structure through a perfect fit to a model. This is neither likely nor, strictly speaking, physically possible. Since all observations are inherently subject to both instrumental and environmental effects there will always be some degree of variance even from a model that exhibits complete theoretical understanding of a mechanism. In such a case we must therefore either content ourselves with the comparatives and with the drive to improve the model and its parameters or define an arbitrary threshold of "good enough fit". Thus these results do provide an effective basis for an initial structural and behavioural analysis of reconnection layer crossings.

7.3 Suggested Extensions to the Study

The extensions to this study come in two sections; The extensions to the model, and the extensions to the methods used to apply the model.

Due to the modularity of the functions used in the work, these two can, and should, be addressed independently.

Extensions to the model are primarily centered around a fundamental change of model. The model used as the basis for the current simulations is the updated form of the original Heyn et al. model (Heyn et al., 1988b) incorporating the extensions to the steady-state solution until the advent of the time-dependent model

in 1992 (Semenov et al., 1992a). The strength of this model is the simplicity with which it can be applied to cases and the fact that, although simplified, the structure it generates is applicable. Later models produced in this vein expand on this by extending the model to include three spatial dimensions (Biernat et al., 1998), the aforementioned time-dependency (Semenov et al., 1992b), multi-species fluids and relativistic effects (Tolstykh et al., 2007). These changes address some of the concerns about model applicability listed in 6.1.4.

Extensions to the methods are comprised around changes to the fitness system and changes to the search method and parameters.

The fitness system is required to be internally consistent, malleable (in terms of variable selection) and verbose (in that it needs to provide both values for each internal structure and variable and wave groupings for each section of that structure as well as totals for export and comparative collation).

Changes to the search method and parameters includes optimizing the searching methods in the fitness landscape to increase the accuracy of the final solution and to decrease the number of generations it takes to locate this solution. Previously mentioned methods include Differential Evolution or Particle Swarm Optimization. Another possible change to the search methods is to include the possibility of process automation.

7.3.1 Automation: Simulation and Search

In this study, the initial crossing positions were identified and used as starting points for the simulations. Development of these methods would then suggest the need for either; an initial selection algorithm for identifying candidate crossing positions before applying these methods to them, or the capacity to be integrated into the system that allows for the algorithms to be applied to an interval in the time series data and find any existing crossing positions in that series. This latter possibility might include an interface with a database such as the Cluster Active Archive (CAA) Predicted Scientific Events (PSE) or Identified Scientific Events (ISE) lists.

The ability of the algorithms to then Search through data sets may prove valuable in that in each simulation several pieces of information could immediately be returned:

1. Absolute Fitness : Can be used both as a confirmator of a candidate for a reconnection event and, after analysis, a comparable measure of the efficacy of the model when applied to that event.

2. Structure Factors : The η and $|\mathbf{b}|$ structure factors define the presence and nature of the types of MHD wave modes used to create the model. In this case they could be used to select candidate events for the study of these wave types and their conditions.

3. Model Structure : The comparative strengths of wave modes in comparison to initial conditions could be used in a statistical manner to explore the limiting behaviour.

4. Discontinuity Positions : This information can be interpreted using spacecraft location data to describe thickness of discontinuities, their spacing and the spatial extent of the entire transition region.

This information, in tandem with positional and space-weather data, could provide a basis for statistical studies of physical mechanisms and the locations in the magnetosphere where they occur. Initial theoretical questions to be answered in this case would be to define thresholds of recognition in terms of structure constants, types and most importantly fitness levels for candidate events. As such, the values reported in this study could form in initial criteria set to be expanded through further testing, mostly of other structural types in other locations.

The automation process would therefore be a major goal, after updating the model and search methods, for this work should it be given the opportunity to continue. I conclude that it may have much to offer in the way of satellite data analysis and catagorisation. In summary:

- This Petscheck-type reconnection layer model seems to, within tolerances imposed by theory, provide a good behavioural and structural framework that could form the basis of an event analysis.

- A model, such as the one used here, may be applied through the use of external (BVSR) and internal (RLDS) structural algorithms in an internally self-consistent way to quickly locate and classify specific features.

- Possibilities for this information include a deeper analysis of a single event, a statistical study of a set of related events/behaviours through to the searching within a sizeable data set for events fitting certain model criteria.

Bibliography

T. L. Aggson, P. J. Gambardella, and N. C. Maynard. Electric field measurements at the magnetopause 1. observation of large convective velocities at rotational magnetopause discontinuities. *Journal of Geophysical Research*, 88(A12):10000–10010, 1983.

A. Balogh, C. M. Carr, M. H. Acuña, M. W. Dunlop, T. J. Beek, P. Brown, K.-H. Fornacon, E. Georgescu, K.-H. Glassmeier, J. Harris, G. Musmann, T. Oddy, and K. Schwingenschuh. The cluster magnetic field investigation: overview of in-flight performance and initial results. *Annales Geophysicae*, 19:1207–1217, 2001.

T. M. Bauer, G. Paschmann, N. Sckopke, R. A. Treumann, W. Baumjohann, and T. D. Phan. Fluid and particle signatures of dayside reconnection. *Annales Geophysicae*, 19:1045–1063, 2001.

W. Baumjohann and R. A. Treumann. *Basic Space Plasma Physics*. Imperial College Press, 1996.

L. Biermann. Kometenschweife und solare korpuskularstrahlung. *Zeitschrift fr Astrophysik*, 29:274, 1951.

H. K. Biernat, M. F. Heyn, R. P. Rijnbeek, V. S. Semenov, and C. J. Farrugia. The structure of reconnection layers: Application to the earth's magnetopause. *Journal of Geophysical Research*, 94(A1):287–298, 1989.

H. K. Biernat, V. S. Semenov, and R. P. Rijnbeek. Time-dependent three-

dimensional petschek-type reconnection: A case study for magnetopause conditions. *Journal of Geophysical Research*, 103(A3):4693–4706, 1998.

Jr. Coleman, P. J., C. P. Sonett, D. L. Judge, and E. J. Smith. Some preliminary results of the pioneer v magnetometer experiment. *Journal of Geophysical Research*, 65(6):1856–1857, 1960.

S. W. H. Cowley. The causes of convection in the earth's magnetosphere: A review of developments during the ims. *Reviews of Geophysics and Space Physics*, 20(3): 531–556, 1982.

I. Dandouras, A. Barthe, E. Penou, H. Rème, S. McCaffrey, C. Vallat, L. M. Kistler, and the CIS Team. Archival of the cluster ion spectrometry (cis) data in the cluster active archive (caa). In *Cluster and Double Star Symposium 5th Anniversary of Cluster in Space,*, Noordwijk, The Netherlands, 2005. ESA.

F. de Hoffmann and E. Teller. Magneto-hydrodynamic shocks. *Physical Review*, 80 (4):692–703, 1950.

J. W. Dungey. Interplanetary magnetic field and the auroral zones. *Physical Review Letters*, 6(2):47, 1961.

J. P. Eastwood. The science of space weather. *Philosophical Transactions of the Royal Society A*, 366:4489–4500, 2008.

M. Eriksson, M. Øieroset, D. N. Baker, C. Mouikis, A. Vaivads, M. W. Dunlop, H. Rème, R. E. Ergun, and A. Balogh. Waln and slow-mode shock analysis in the near-earth magnetotail in connection with a substorm onset on 27 august 2001. *Journal of Geophysical Research*, 109:1–15, 2004.

M. H. Farris and C. T. Russell. Determining the standoff distance of the bow shock: Mach number dependance and use of models. *Journal of Geophysical Research*, 99(A9):17681–17689, 1994.

J. M. Gloag, C. Carr, B. Forte, and E. A. Lucek. The status of cluster fgm data submissions to the caa. In *Cluster and Double Star Symposium 5th Anniversary of Cluster in Space,*, Noordwijk, The Netherlands, 2005. ESA.

M. F. Heyn, R. P. Rijnbeek, H. K. Biernat, V. S. Semenov, C. J. Farrugia, D. J. Southwood, G. Paschmann, N. Sckopke, and C. T. Russell. Energy flow inside a reconnection layer containing slow shocks. *Advances in Space Research*, 8(9-10): (9)239–(9)244, 1988a.

Martin F. Heyn, Helfried K. Biernat, Richard P. Rijnbeek, and Vladimir S. Semenov. The structure of reconnection layers. *The Journal of Plasma Physics*, 40(2):235–252, 1988b.

H. Hugoniot. Propagation des mouvements dans les corps et spcialement dans les gaz parfaits. *Journal de 1Ecole Polytechnique*, 57, 58:3, 1, 1887, 1889.

H. Kawano and T. Higuchi. A generalization of the minimum variance analysis method. *Annales Geophysicae*, 14(10):1019–1024, 1997. 10.1007/s00585-996-1019-1.

M. G. Kivelson and C. T. Russell. *Introduction to space physics.* Cambridge University Press, Cambridge ; New York, 1995. 94019084 edited by Margaret G. Kivelson, Christopher T. Russell. Space physics ill. ; 27 cm. Includes bibliographical references (p. 545-562) and index.

Irving Langmuir. The interaction of electron and positive ion space charges in cathode sheaths. *Physical Review*, 33(6):954, 1929. Copyright (C) 2008 The American Physical Society.

M. Lockwood and M. A. Hapgood. How the magnetopause transition parameter works. *Geophysical Research Letters*, 24(4):373–376, 1997.

O. Lodge. Sun spots, magnetic storms, comets tails, atmospheric electricity, and aurorae. *Electrician*, 46:249–250, 1900.

J. Merka, A. Szabo, T.W. Narock, J.D. Richardson, and J.H. King. Three decades of bow shock observations by imp 8 and model predictions. *Planetary and Space Science*, 53:79–84, 2005.

F. S. Mozer, S. D. Bale, and T. D. Phan. Evidence of diffusion regions at a subsolar magnetopause crossing. *Physical Review Letters*, 89(1):015002–1 – 015002–4, 2002.

K. Nykyri, A. Otto, B. Lavraud, C. Mouikis, L. M. Kistler, A. Balogh, and H. Rème. Cluster observations of reconnection due to the kelvin-helmholtz instability at the dawnside magnetospheric flank. *Annales Geophysicae*, 24:2619–2643, 2006.

M. Øieroset, T. D. Phan, R. P. Lin, and B. U. O. Sonnerup. Walen and variance analyses of high-speed flows observed by wind in the midtail plasma sheet: Evidence for reconnection. *Journal of Geophysical Research*, 105(A11):25247–25263, 2000.

E. Parker. Extension of the solar corona into interplanetary space. *Journal of Geophysical Research*, 64, 1959.

G. Paschmann and Patrick W. Daly. *Analysis Methods for Multi-Spacecraft Data*, volume 1 of *ISSI Scientific Report Series*. International Space Science Institute, 1998.

G. Paschmann and Patrick W. Daly. *Multi-Spacecraft Analysis Methods Revisted*. ISSI Scientific Report Series. ESA Communications, 2008.

G. Paschmann, B. U. O. Sonnerup, I. Papamastorakis, N. Sckopke, G. Haerendel, S. J. Bame, J. R. Asbridge, J. T. Gosling, C. T. Russell, and R. C. Elphic. Plasma acceleration at the earth's magnetopause: evidence for reconnection. *Nature*, 282 (5736):243–246, 1979. 10.1038/282243a0.

T. D. Phan, M. W. Dunlop, G. Paschmann, B. Klecker, J. M. Bosqued, H. Rème, A. Balogh, C. Twitty, F. S. Mozer, C. W. Carlson, C. Mouikis, and L. M. Kistler. Cluster observations of continuous reconnection at the magnetopause under steady

interplanetary magnetic field conditions. *Annales Geophysicae*, 22(7):2355–2367, 2004.

W. J. M. Rankine. On the thermodynamic theory of waves of finite longitudinal disturbances. *Philosophical Transactions of the Royal Society of London*, 160:277, 1870.

A. Retinò, M. B. Bavassano Cattaneo, M. F. Marcucci, A. Vaivads, M. André, Y. Khotyaintsev, T. D. Phan, G. Pallocchia, H. Rème, E. Möbius, B. Klecker, C. W. Carlson, M. McCarthy, A. Korth, R. Lundin, and A. Balogh. Cluster multi-spacecraft observations at the high-latitude duskside magnetopause: implications for continuous and component magnetic reconnection. *Annales Geophysicae*, 23 (2):461–473, 2005.

R. P. Rijnbeek. Magnetic field reconnection at the dayside magnetopause. In *26th ESLAB Symposium - Study of the Solar-Terrestrial System*, volume SP-346, pages 151–160, Killarney, Ireland, 1992. ESA.

R. P. Rijnbeek and V. S. Semenov. Features of a petschek-type reconnection model. *Trends in Geophysical Research*, 2:247–268, 1993.

R. P. Rijnbeek, H. K. Biernat, M. F. Heyn, V. S. Semenov, C. J. Farrugia, D. J. Southwood, G. Paschmann, N. Sckopke, and C. T. Russell. The structure of the reconnection layer observed by isee 1 on 8 september 1978. *Annales Geophysicae*, 7(3):297–310, 1989.

C. T. Russell. The structure of the magnetopause. *Planetary and Space Science*, 51 (12):731–744, 2003.

V. S. Semenov, I. V. Kubyshkin, V. V. Lebedeva, R. P. Rijnbeek, M. F. Heyn, H. K. Biernat, and C. J. Farrugia. A comparison and review of steady-state and time-varying reconnection. *Planetary and Space Science*, 40(1):63–87, 1992a.

V. S. Semenov, I. V. Kubyshkin, V. V. Lebedeva, M. V. Sidneva, H. K. Biernat, M. F. Heyn, B. P. Besser, and R. P. Rijnbeek. Time-dependent localized reconnection

of skewed magnetic fields. *Journal of Geophysical Research*, 97(A4):4251–4263, 1992b.

J.-H. Shue, J. K. Chao, H. C. Fu, C. T. Russell, P. Song, K. K. Khurana, and H. J. Singer. A new functional form to studv the solar wind control of the magnetopause size and shape. *Journal of Geophysical Research*, 102(A5):9497–9511, 1997.

D.G. Sibeck, R. E. Lopez, and E. C. Roelof. Solar wind control of the magnetopause shape, location, and motion. *Journal of Geophysical Research*, 96(A4):5489–5495, 1991.

B. U. O. Sonnerup and L. J. Cahill. Magnetopause structure and attitude from explorer 12 observations. *Journal of Geophysical Research*, 72(1):171–183, 1967.

B. U. O. Sonnerup, I. Papamastorakis, G. Paschmann, and H. Luhr. Magnetopause properties from ampte/irm observations of the convection electric field: Method development. *Journal of Geophysical Research*, 92(A11):12137–12159, 1987.

T. Terasawa, H. Kawano, I. Shinohara, T. Mukai, Y. Saito, M. Hoshino, A. Nishida, S. Machida, T. Nagai, T. Yamanoto, and S. Kokubun. On the determination of a moving mhd structure: Minimization of the residue of integrated faraday‘s equation. *Journal of Geomagnetism and Geoelectricity*, 48(5-6):603–614, 1996.

Yu V. Tolstykh, V. S. Semenov, H. K. Biernat, M. F. Heyn, and T. Penz. Relativistic unsteady petschek-type model of magnetic reconnection. *Advances in Space Research*, 40:1538–1542, 2007.

N. A. Tsyganeko. Effects of the solar wind conditions on the global magnetospheric configuration as deduced from data-based field models. In *Third International Conference on Substorms (ICS-3)*, volume SP-389, pages 181–185, Versailles, France, 1996. ESA.

A. Vaivads, Y. Khotyaintsev, M. André, A. Retinò, and S. C. Buchert. Structure of the magnetic diffusion region from four-spacecraft observations. *Physical Review Letters*, 93(10):105001–1–4, 2004.

D. W. Walthour, B. U. O. Sonnerup, and C. T. Russell. Observation of a slow-mode shock in the dayside magnetopause reconnection layer. *Advances in Space Research*, 15(8/9):501–506, 1995.

Y. Zheng, G. Le, J. A. Slavin, M. L. Goldstein, C. Cattell, A. Balogh, E. A. Lucek, H. Rème, J. P. Eastwood, M. Wilber, G. Parks, A. Retinò, and A. Fazakerley. Cluster observation of continuous reconnection at dayside magnetopause in the vicinity of cusp. *Annales Geophysicae*, 23(6):2199–2215, 2005.

Appendix A

Simulation Equations

A.1 Initial Setup

The factors that are input directly as boundary values to the model are presented in Table A.1

N_0	Number density
R_{M0}	Mass Factor ($H^+ = 1.0$)
V_{L0}	Bulk Velocity L component
V_{M0}	Bulk Velocity M component
B_{L0}	Magnetic Field L component
B_{M0}	Magnetic Field M component

Table A.1: Values input into the RL simulation

Upstream values are as above, downstream values are denoted with a tilde. ($\tilde{N_0}$)

A.2 Wave Layer Calculations

A.2.1 First Alfvén Wave

The static equations for this layer, in the absence of including "soft" Alfvén waves (discrete intra-wave rotation), are:

$$\rho_0 = \rho_1 \tag{A.1}$$

$$N_1 = N_0 \tag{A.2}$$

$$P_1 = P_0 \tag{A.3}$$

$$B_{M1} = \left[\frac{\vec{b}_M}{V_{A0}\vec{\hat{b}}}\right] \tag{A.4}$$

$$B_{L1} = \left[\frac{\vec{b}_L}{V_{A0}\vec{\hat{b}}}\right] \tag{A.5}$$

$$B_{\perp 1} = \sqrt{B_{M1}^2 + B_{L1}^2} \tag{A.6}$$

$$\alpha_{B_{\perp 1}} = tan^{-1}\left(\frac{B_{L1}}{B_{M1}}\right) \tag{A.7}$$

$$V_{M1} = V_{M0} - S_{\pm}\left[V_{AM0} - V_{A0}\left(\frac{\vec{b}_M}{V_{A0}\vec{\hat{b}}}\right)\right] \tag{A.8}$$

$$V_{L1} = V_{L0} - S_{\pm}\left[V_{AL0} - V_{A0}\left(\frac{\vec{b}_L}{V_{A0}\vec{\hat{b}}}\right)\right] \tag{A.9}$$

$$V_{\perp 1} = \sqrt{V_{M1}^2 + V_{L1}^2} \tag{A.10}$$

$$\alpha_{V_{\perp 1}} = tan^{-1}\left(\frac{V_{L1}}{V_{M1}}\right) \tag{A.11}$$

$$\beta_1 = \frac{P_1 F_2}{B_{\perp 1}^2} \tag{A.12}$$

$$T_1 = \frac{P_1}{N_1 R} \tag{A.13}$$

These equations form the basis for the Alfvén layer behaviour and stand completely unchanged as long as the option for discrete rotation of the magnetic field direction across the Alfvén wave is not used. If it is, then these equations are used to define the final values for the layer, the field direction parameters (and the quantities that depend on them) are then subject to an additional set of functions.

(A.14)

A.2.2 First Slow Mode Wave

$\eta < 1$ **: Slow Shock**

$$\alpha_S = 1 + \left(\frac{1 - \eta^2}{\gamma\beta + (\gamma - 1)(1 - \eta)} \right) \tag{A.15}$$

$$\rho_2 = \rho_1 \alpha_S \tag{A.16}$$

$$N_2 = \frac{\rho_2}{R_{M0}} \tag{A.17}$$

$$P_2 = P_1 \left[1 + \frac{1 - \eta^2}{\beta} \right] \tag{A.18}$$

$$B_{M2} = \eta B_{\perp 0} \left(\frac{\vec{b}_M}{V_{A0}\hat{\vec{b}}} \right) \tag{A.19}$$

$$B_{L2} = \eta B_{\perp 0} \left(\frac{\vec{b}_L}{V_{A0}\hat{\vec{b}}} \right) \tag{A.20}$$

$$B_{\perp 2} = \sqrt{B_{M2}^2 + B_{L2}^2} \tag{A.21}$$

$$\alpha_{B_{\perp 2}} = tan^{-1} \left(\frac{B_{L2}}{B_{M2}} \right) \tag{A.22}$$

$$V_{M2} = V_{M0} - S_{\pm} \left[V_{AM0} - V_{A0} \left(\frac{\vec{b}_M}{V_{A0}\hat{\vec{b}}} \right) G_S(\eta) \right] \tag{A.23}$$

$$V_{L2} = V_{L0} - S_{\pm} \left[V_{AL0} - V_{A0} \left(\frac{\vec{b}_L}{V_{A0}\hat{\vec{b}}} \right) G_S(\eta) \right] \tag{A.24}$$

$$V_{\perp 2} = \sqrt{V_{M2}^2 + V_{L2}^2} \tag{A.25}$$

$$\alpha_{V_{\perp 2}} = tan^{-1} \left(\frac{V_{L2}}{V_{M2}} \right) \tag{A.26}$$

$$\beta_2 = \frac{P_2 F_2}{B_{\perp 2}^2} \tag{A.27}$$

$$T_2 = \frac{P_2}{N_2 R} \tag{A.28}$$

$\eta > 1$ **: Slow Expansion Fan**

For n points per layer.

$$D_{INC} = \frac{\eta - 1}{n} \tag{A.29}$$

$$D_\eta = 1 \tag{A.30}$$

$$D_\eta = D_\eta + D_{INC} \tag{A.31}$$

The equations that are looped.

$$P_2 = P_1 \left[1 + \frac{1 - D_\eta^2}{\beta}\right] \tag{A.32}$$

$$\rho_2 = \rho_1 \left(\frac{P_2}{P_1}\right)^{\frac{1}{\gamma}} \tag{A.33}$$

$$N_2 = \frac{\rho_2}{R_{M0}} \tag{A.34}$$

$$B_{M2} = D_\eta B_{\perp 0} \left(\frac{\vec{b}_M}{V_{A0}\vec{\hat{b}}}\right) \tag{A.35}$$

$$B_{L2} = D_\eta B_{\perp 0} \left(\frac{\vec{b}_L}{V_{A0}\vec{\hat{b}}}\right) \tag{A.36}$$

$$B_{\perp 2} = \sqrt{B_{M2}^2 + B_{L2}^2} \tag{A.37}$$

$$\alpha_{B_{\perp 2}} = tan^{-1}\left(\frac{B_{L2}}{B_{M2}}\right) \tag{A.38}$$

$$V_{M2} = V_{M0} - S_\pm \left[V_{AM0} - V_{A0}\left(\frac{\vec{b}_M}{V_{A0}\vec{\hat{b}}}\right) G_R(D_\eta)\right] \tag{A.39}$$

$$V_{L2} = V_{L0} - S_\pm \left[V_{AL0} - V_{A0}\left(\frac{\vec{b}_L}{V_{A0}\vec{\hat{b}}}\right) G_R(D_\eta)\right] \tag{A.40}$$

$$V_{\perp 2} = \sqrt{V_{M2}^2 + V_{L2}^2} \tag{A.41}$$

$$\alpha_{V_{\perp 2}} = tan^{-1}\left(\frac{V_{L2}}{V_{M2}}\right) \tag{A.42}$$

$$\beta_2 = \frac{P_2 F_2}{B_{\perp 2}^2} \tag{A.43}$$

$$T_2 = \frac{P_2}{N_2 R} \tag{A.44}$$

Appendix B

Further case studies data.

B.1 20th February 2002

B.1.1 14:00 UT

Spacecraft	N_X	N_Y	N_Z	Method
1	0.5455 ± 0.0119	0.1953 ± 0.0143	0.8150 ± 0.0102	MVAB
3	0.5264 ± 0.0133	0.1831 ± 0.0155	0.8303 ± 0.0108	MVAB
4	0.2712 ± 0.0154	-0.2536 ± 0.0140	0.9285 ± 0.0018	TD

Table B.1: Results of Boundary Normal determination for the crossing at ≈14:00UT on the 20th February 2002 for spacecrafts 1, 3 & 4, including information about orientation and method used.

Spacecraft	Instrument	V_{HTL}	V_{HTM}	V_{HTN}	A	C	D/D0
1	CODIF	196.69	-11.46	12.71	0.99	0.96	0.07
	HIA	233.87	-21.84	4.98	1.00	0.97	0.05
3	CODIF	227.42	-54.73	-35.78	1.01	0.98	0.04
	HIA	292.12	-48.01	27.58	1.00	0.98	0.04
4	CODIF	116.19	130.14	99.15	1.00	0.97	0.06

Table B.2: Results of dHT analyses over the boundary transitions at 14:00UT for spacecrafts 1, 3 & 4. All velocities are given in km/s

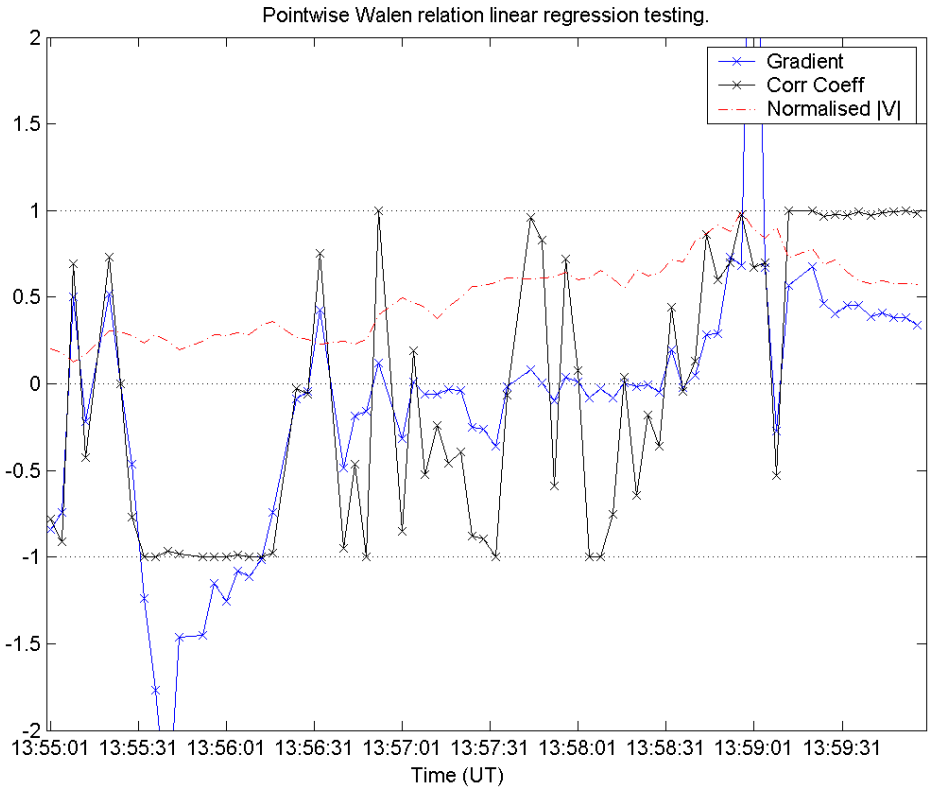

Figure B.1: Results of a pointwise comparison between the Walén relation and observational data collected by the spacecraft 4 CIS-CODIF instrument on the 20th of February 2002 at $\approx$ 14:00UT.

Variable	A-S	S-C	C-$\tilde{S}$	$\tilde{S}$-$\tilde{A}$	Total
Spacecraft 1					
B (FGM)	2.34	2.55	1.17	0.21	6.27
V (CODIF)	0.08	0.05	0.04	0.02	0.19
N (CODIF)	0.05	0.06	1.44	0.41	1.95
T (CODIF)	2.22	2.50	6.21	1.34	12.27
η	1.51	$\tilde{\eta}$	0.69	Fitness Total	20.68
Spacecraft 3					
B (FGM)	1.10	1.91	0.15	0.65	3.82
V (CODIF)	0.55	0.06	0.05	0.10	0.76
N (CODIF)	0.61	0.61	7.98	4.57	13.77
T (CODIF)	5.65	2.01	0.14	0.94	8.74
η	1.57	$\tilde{\eta}$	0.72	Fitness Total	27.09
Spacecraft 4					
B (FGM)	0.93	2.34	0.39	0.21	3.86
V (CODIF)	0.14	0.04	0.03	0.02	0.23
N (CODIF)	0.02	0.04	0.53	0.03	0.62
T (CODIF)	1.66	1.91	1.32	2.36	7.25
η	1.69	$\tilde{\eta}$	0.79	Fitness Total	11.97

Table B.3: A breakdown of the fitness values for initial discontinuity structure and boundary value sampling ranges for the crossing of spacecrafts 1, 3 & 4 on the 20th of February 2002 at $\approx$ 14:00UT. The CIS-CODIF data was used as the CIS-HIA data was incomplete during this interval.

Variable	A-S	S-C	C-$\tilde{S}$	$\tilde{S}$-$\tilde{A}$	Total
Spacecraft 1					
B (FGM)	0.09	1.48	0.65	0.45	2.66
V (CODIF)	0	0.43	0.09	0.02	0.54
N (CODIF)	0	0.03	1.34	0.72	2.10
T (CODIF)	0	2.04	2.38	0.30	4.72
η	1.51	$\tilde{\eta}$	0.69	Fitness Total	10.02
Spacecraft 3					
B (FGM)	1.22	0.85	0.45	0.37	2.89
V (CODIF)	0.34	0.16	0.14	0.03	0.67
N (CODIF)	0.30	0.24	3.61	2.53	6.67
T (CODIF)	2.54	2.65	0.08	0.18	5.45
η	1.57	$\tilde{\eta}$	0.72	Fitness Total	15.68
Spacecraft 4					
B (FGM)	0.37	0.31	0.65	0.09	1.42
V (CODIF)	0.11	0.24	0.09	0.02	0.46
N (CODIF)	0.01	0.05	0.38	0.07	0.50
T (CODIF)	1.33	1.68	0.54	0.55	4.09
η	1.69	$\tilde{\eta}$	0.7911	Fitness Total	6.47

Table B.4: A breakdown of the fitness values for the discontinuity structure calculated by the RLDS algorithm using the initial and boundary value sampling ranges for the crossing of spacecrafts 1, 3 & 4 on the 20th of February 2002 at $\approx$ 14:00UT.

Variable	A-S	S-C	C-$\tilde{S}$	$\tilde{S}$-$\tilde{A}$	Total
Spacecraft 1					
B (FGM)	0.27	2.17	0.88	0.44	3.76
V (CODIF)	0	0.17	0.03	0.03	0.24
N (CODIF)	0	0.03	1.05	0.75	1.82
T (CODIF)	0	1.76	1.89	0.31	3.95
η	1.98	$\tilde{\eta}$	0.93	Fitness Total	9.77
Spacecraft 3					
B (FGM)	1.29	0.50	0.51	0.37	2.66
V (CODIF)	0.11	0.07	0.04	0.12	0.33
N (CODIF)	0.36	0.25	1.29	1.21	3.10
T (CODIF)	1.73	1.69	0.24	0.34	4.01
η	1.80	$\tilde{\eta}$	0.89	Fitness Total	10.11
Spacecraft 4					
B (FGM)	0.37	0.41	0.45	0.09	1.32
V (CODIF)	0.04	0.09	0.05	0.05	0.23
N (CODIF)	0.02	0.05	0.33	0.06	0.46
T (CODIF)	1.25	1.54	0.49	0.55	3.83
η	1.82	$\tilde{\eta}$	0.86	Fitness Total	9.77

Table B.5: A breakdown of the final fitness values for the discontinuity structure calculated by the RLDS and BVSR algorithms for the crossing of spacecrafts 1, 3 & 4 on the 20th of February 2002 at $\approx$ 14:00UT.

Appendix C

Core Programs

C.1 rlatest.m : Reconnection Layer Simulation

See attached CD-ROM.